



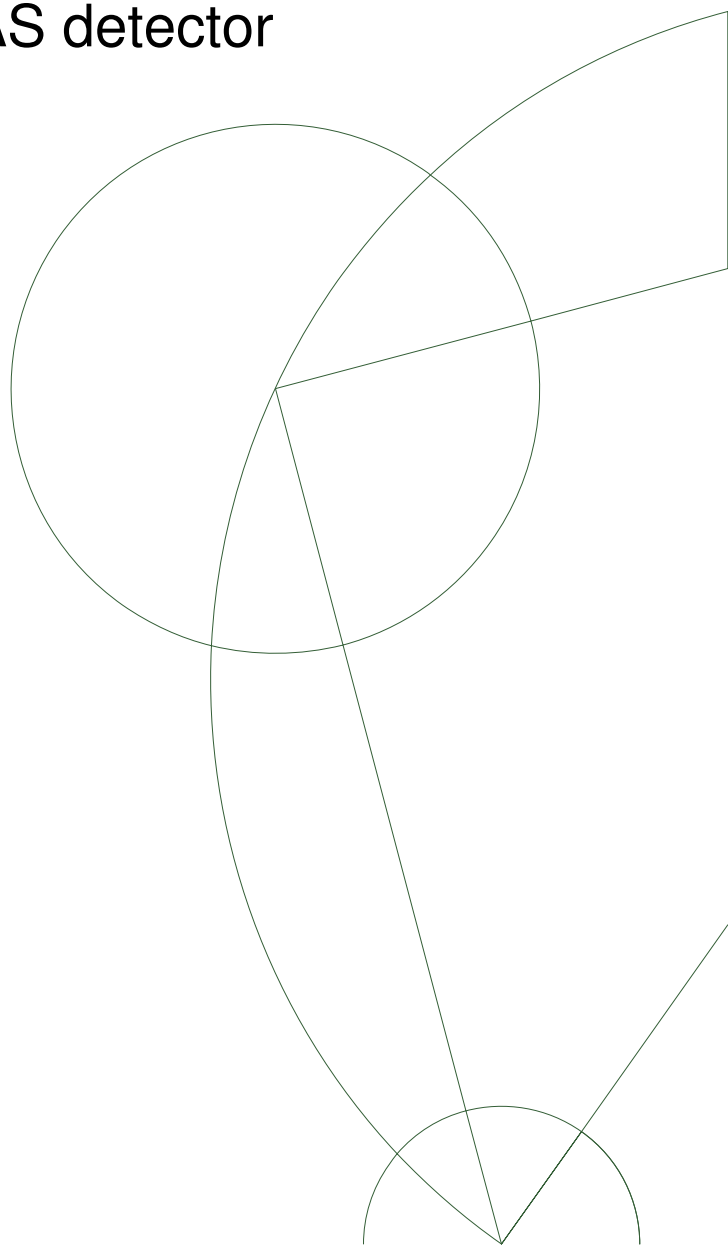
Master thesis

Jesper Roy Christiansen

Strange particle production in the underlying event
in pp-collisions at a center-of-mass energy
of $\sqrt{s} = 7 \text{ TeV}$ with the ATLAS detector

Supervisor
Peter Hansen

Niels Bohr Institute
1. September, 2011



Acknowledgement

I would like to thank all the people with whom I have had the pleasure to share the same office: Bjørn, Christian, Christoffer, Gorm, Henriette, Lars, Martin and Terkel. You have made the experience of making a master thesis much more enjoyable than it otherwise would have been.

I am also grateful to all the people in the High Energy Physics group for all the entertaining and (at times) insightful discussions. Without these, this thesis would not have been possible. Also, all the people within the discovery center should be noted for all the interesting discussions, especially with their different perspectives on particle physics.

Finally, I would like to thank my supervisor, Peter Hansen, for first of all introducing me to the wonderful world of soft QCD. And also for his guidance and ability to provide enlightning explanations, whenever I faced a problem.

Contents

1	Introduction	1
2	The Standard Model	3
2.1	The particle zoo	3
2.2	The mathematical foundation for the standard model	5
2.3	Quantum Chromo Dynamics - QCD	6
2.4	Strange particles	8
2.4.1	The strange quark	8
2.4.2	The K^0 meson	9
2.4.3	The Λ baryon	11
3	A proton-proton collision	12
3.1	Parton distribution functions	14
3.2	The hard interaction	15
3.3	Soft QCD processes	16
3.4	Final state radiation and initial state radiation	17
3.5	Hadronization	19
3.6	The underlying event	20
4	Event generators	22
4.0.1	Tuning of event generators	23
5	Studying the underlying event	25
5.1	Previous studies of the underlying event	26
6	The Large Hadron Collider	29
6.1	The four major experiments at LHC	30
7	The ATLAS Detector	32
7.1	Measuring charged particles	33
7.2	The Inner Detector	35
7.2.1	Silicon pixel detector	36
7.2.2	Silicon strip detector (SCT)	36
7.2.3	Transition Radiation Tracker (TRT)	36
7.2.4	Material budget	37
7.2.5	Track reconstruction	37
7.2.6	Tracking resolution	39
7.2.7	Vertex Reconstruction	40
7.3	Simulation of the ATLAS detector	41

7.4	Data driven controls of the simulation of the inner detector . . .	41
8	The analysis	43
8.1	Overview of the analysis	43
8.2	Data selection	45
8.3	Event selection	46
8.3.1	Minimum bias event selection	46
8.3.2	Non diffractive event selection	47
8.3.3	Phase-space cuts on the event generators	48
8.4	Track selection	48
8.4.1	Phase-space cuts on the event generators	51
8.5	From tracks to jets	51
8.6	Measuring the number of K_S^0 and Λ particles	53
8.6.1	Selection of secondary vertices	54
8.6.2	Transverse flight distance	56
8.6.3	Secondary vertex probability	58
8.6.4	CosThetaPointing	59
8.6.5	Fitting the mass histogram	61
8.6.6	Phase-space cuts on the event generators	64
8.7	Efficiencies and corrections procedures	66
8.7.1	Event wide corrections	66
8.7.2	Track corrections	68
8.7.3	Correction for K_S^0 and Λ efficiencies	69
8.7.4	Final correction	71
8.8	Differences between the analyses for the different final distributions	72
8.8.1	K_S^0 (Λ) multiplicity density as a function of $p_T^{\text{leading jet}}$	73
8.8.2	The average p_T distribution and the sum p_T distribution	74
8.8.3	Track based distributions	75
9	Systematic uncertainties	76
9.1	Systematic uncertainties from variation of cuts	76
9.2	Systematic uncertainties from adding extra material	77
9.3	Systematic uncertainties from model dependency	78
9.4	Systematic uncertainties from the fitting method	78
9.5	Systematic uncertainties from the bin-to-bin migration cor- rection	78
9.6	Systematic uncertainties from final correction for Λ	79
9.7	Summary of the systematic uncertainties	80

10 Lifetime distribution	82
11 Results	84
11.1 Angular multiplicity density	84
11.2 Multiplicity density vs. $p_T^{\text{leading jet}}$	88
11.3 Average transverse momentum vs. $p_T^{\text{leading jet}}$	89
11.4 Sum p_T vs. $p_T^{\text{leading jet}}$	89
11.5 Comparison to track based results	92
12 Conclusion	100
13 Appendix A - Summary of cuts	101
14 Appendix B - Glossary	102
15 Resume - English	112
16 Resume - dansk	114

1 Introduction

In some of the first studies of the data from the LHC, an excess of particles containing strange quarks was observed [1] (over the predictions from models tuned using LEP and Tevatron data). Observing an excess always inspires to ask the question as to what the physical origin is and in this specific case, whether it is an overall excess (all production mechanisms predicted too few strange particles in the simulations) or if it is possible to single out a few production mechanisms with a higher strange production than expected. One of the candidates to explain the excess is the underlying event. Since the production of strange hadrons was tuned according to LEP data and no underlying event is present in e^+e^- collisions, it would be a possible way to explain the excess without breaking the consistency between the event generators and the LEP data.

Studies of the underlying event fall under the category of non-perturbative QCD, thus a rigorous calculation of the underlying event within the standard model is not possible. Instead one has to rely on different phenomenological models, which need tuning from the observed data. Thus, further studies of the underlying event could lead to a better understanding (and thereby a better model) of non-perturbative QCD.

Since the underlying event is present in any proton-proton collision, the understanding of the underlying event will influence the outcome of any physics analysis. And an improvement in our understanding of the underlying event would lead to better possibilities in searches for new physics. For instance the search for the Higgs boson in the $H \rightarrow \gamma\gamma$ channel, the orientation of the two photons relies on the primary vertex [2]. And since the two photons do not leave any tracks in the detector, the primary vertex is reconstructed from the tracks coming from the underlying event.

In this thesis I will present the standard distributions describing the underlying event using K_S^0 and Λ^1 particles. The distributions are corrected for detector effects, permitting a comparison between the data and different event generators. The number of K_S^0 and Λ particles is found by fitting the invariant mass distributions, under the assumption of a $\pi^+\pi^-$ decay and $p^+\pi^-$ decay for the K_S^0 and Λ , respectively. The correction due to the efficiency of the detector is found by the use of a full detector simulation.

¹The $\bar{\Lambda}$ is not considered due to the wrong simulation of the anti-proton interaction with material in GEANT [3].

In the end a correction is applied to handle bin-to-bin migration as well as any difference in the estimate from the fit and the actual expected number.

The systematic uncertainties are estimated by a combination of data-driven studies and MC studies. The MC studies are used to estimate the effect of additional material in the inner detector. It is also used to calculate the systematic uncertainty from the final correction (i.e. bin-to-bin migration and the fitting procedure). The data-driven studies are used to vary the different cuts and compare the efficiencies estimated from MC and data. In addition a final control of the method is accomplished by comparing the measured lifetime with the expected.

The thesis provides first a brief introduction to the standard model. The emphasize is on QCD and especially the properties of strange quarks and the K_S^0 and Λ hadrons. Afterwards an explanation of the physic processes behind a proton-proton collision is explained, which includes the introduction to the underlying event. In section 4, the different event generators used in this thesis is introduced. The experimental setup is described in section 6 and 7, with the first section describing the LHC and the second the ATLAS detector. The emphasize in the description of the ATLAS detector is the reconstruction of tracks and vertices, and hence also the needed detector components.

The analysis method is described afterwards (section 8), where a brief overview is provided before going into details with the selection and correction procedures. In section 9 a study of the systematic uncertainties is presented followed by a data-driven test of the analysis method (section 10). Finally the results are presented in section 11, the section is split into two major parts: The first part is the presentation of the measured distributions and second part is a comparison between track-based studies and the previous presented results. In the end, a conclusion of the results is provided.

I have tried to explain the jargon of high energy physics when the special terms are first introduced. But I have also included a glossary of the most used terms within high energy physics in appendix B, thus if you at any point stumble upon a specific abbreviation, it might be possible to find it here.

2 The Standard Model

The standard model is the description of the fundamental particles and the interactions among them. The development of the standard model started a century ago with the discovery of the electron, but the idea of fundamental particles goes all the way back to Democritus in ancient Greece. During the last century many discoveries, the latest being the discovery of the tau neutrino [4], and theoretical developments have lead to the current standard model, which describes three out of the four known forces. The three forces included are the electromagnetic force, the weak force and the strong force; only gravity is missing.

One of the major motivations behind the standard model is the combination of different theories into one common theory, the ultimate goal being one single theory describing everything. The idea of combining theories goes back in history, a prime example being the combination of electrical and magnetic forces into Maxwell's equations. Within the development of the standard model examples of combinations of previous separated theories also exist, namely the combination of the electromagnetic force with the weak force. This combination was a big step towards the current understanding of the standard model. Because of these examples theorists have for long tried to combine the standard model with general relativity into a theory of everything, but so far no attempts have succeeded.

2.1 The particle zoo

The standard model contains two types of particles: Fermions and bosons, the fermions being the matter particles and the bosons being the force carrier particles. Fermions are half-integer spin particles and follow Fermi statistics². The fermions are often divided into quarks and leptons and each group is further split into three generations (see figure 2.1). Almost all the ordinary matter in the universe is made of constituents from the first generation, the proton and neutron being different compositions of u and d quarks and the electron is in itself an elementary particle of the first generation. It was first in 1936 with the discovery of the muon that particles from the second generation were discovered³. The last generation

²This includes the Pauli exclusion principle which states that two identical particles cannot be in the exact same physical state (for example the electrons in an atom must have different quantum numbers).

³At first this discovery was in fact misinterpreted as the pion predicted by Yukawa in 1935

was observed in 1975 by the discovery of the tau lepton and shortly hereafter (1977) also the bottom quark was discovered. The last discovered particle in the standard model was the tau neutrino, it was observed in 2000 at Fermilab.

The bosons have (by definition) integer spin and all the observed elementary bosons have spin one. The photon is the massless boson carrying the electromagnetic force. The weak force is mediated through the charged W^\pm bosons and the neutral Z boson. Both the W^\pm and Z bosons are massive, thus the range of the weak force is very short ($\approx 2 \cdot 10^{-3}$ fm). The Z and W bosons were discovered at the UA1 and UA2 experiments in 1983 and their discovery was one of the main evidences for the standard model. The gluon is the carrier of the strong force; evidence of its existence was observed in 1979 at DESY. The graviton is the proposed elementary particle for gravity, it has not yet been discovered⁴ and the inclusion of the graviton turns the theory into a non-renormalizable theory.

		Three Generations of Matter (Fermions)			
		I	II	III	
mass →		2.4 MeV	1.27 GeV	171.2 GeV	0
charge →		$\frac{2}{3}$	$\frac{2}{3}$	$\frac{2}{3}$	0
spin →		$\frac{1}{2}$	$\frac{1}{2}$	$\frac{1}{2}$	1
name →		u up	c charm	t top	γ photon
	Quarks				
		4.8 MeV	104 MeV	4.2 GeV	0
		$-\frac{1}{3}$	$-\frac{1}{3}$	$-\frac{1}{3}$	0
		$\frac{1}{2}$	$\frac{1}{2}$	$\frac{1}{2}$	1
		d down	s strange	b bottom	g gluon
	Leptons				
		< 2.2 eV	< 0.17 MeV	< 15.5 MeV	91.2 GeV
		0	0	0	0
		$\frac{1}{2}$	$\frac{1}{2}$	$\frac{1}{2}$	1
		ν_e electron neutrino	ν_μ muon neutrino	ν_τ tau neutrino	Z weak force
		0.511 MeV	105.7 MeV	1.777 GeV	80.4 GeV
		-1	-1	-1	± 1
		$\frac{1}{2}$	$\frac{1}{2}$	$\frac{1}{2}$	1
		e electron	μ muon	τ tau	W^\pm weak force

Figure 2.1: The particles of the standard model.

The last piece of the standard model is the Higgs boson. It was introduced in the standard model as a mechanism to provide all the particles with mass without breaking local gauge invariance (invariant under a gauge transformation⁵). The Higgs boson also is the only prediction of the standard model not yet discovered, and the discovery of the Higgs boson (or the exclusion of its existence) is one of the main physics goals of the

⁴And the detection of a single graviton is not happening within the next years, due to the very low cross section [5]

⁵A gauge transformation is a transformation of the field. As an example consider the following transformation: $\Psi(x) \rightarrow e^{i\alpha(x)}\Psi(x)$. If the transformation is allowed to vary from point to point (exemplified here by α depending upon x) the transformation is called a local gauge transformation.

LHC. If the Higgs is discovered it will be the first elementary particle with spin zero to be observed. Being a scalar boson (spin zero particle), the Higgs boson mass is quadratically influenced by the ultraviolet cutoff scale⁶. The ultraviolet cutoff scale is often set to the Planck scale and the huge difference between the expected Higgs mass (~ 1 TeV) and the Planck scale ($\sim 10^{16}$ TeV) is known as the hierarchy problem of the standard model⁷.

2.2 The mathematical foundation for the standard model

Quantum Field Theory (QFT) is the mathematical framework on which the standard model is built. QFT was developed as a framework to combine two of the biggest discoveries in the start of the 20th century, namely quantum theory and special relativity. In a QFT the particles are represented as fields and the properties of the particles and their interactions are described by the Lagrangian. In a classical physics system the equation of motion is found by the principle of least action, which is to find the point at which the variation of the action⁸ vanishes. In a quantum theory, the path of least action is no longer the only allowed path, instead all possible paths have to be summed over, and this sum is called the Feynman path integral. In general the classical path will dominate, but quantum corrections arise due to the new paths.

In particle physics, one wants to calculate the transition amplitude, i.e. the probability to go from a state of particles with a given momentum, mass, etc. to a new state of particles (an example being $e^+e^- \rightarrow \mu^+\mu^-$). Unfortunately these calculations can in general not be done exactly, instead the transition amplitudes are calculated as perturbations around the classical solution. This works very well for QED (Quantum ElectroDynamics - the theory for the electromagnetic force), since the coupling constant, $\alpha_{EM} \sim \frac{1}{137}$, is much smaller than unity. An example of the perturbation can be seen in figure 2.2, the transitions are represented as Feynman diagrams, which can be directly related to the calculation of the amplitude. The coupling constant for the strong force is much larger than for the electromagnetic

⁶The ultraviolet cutoff scale is a parameter introduced in the renormalization procedure to make an otherwise infinite integral finite. A physical interpretation is that it provides the scale, at which the model breaks down.

⁷The hierarchy problem can be solved within the standard model by the use of fine tuning, however it is still one of the motivation for several beyond standard model theories (for example theories involving supersymmetry or extra dimensions)

⁸The action is defined as the time integral of the Lagrangian

force, and at times even larger than unity⁹. In this case, it is not possible to perform perturbation calculation and therefore this region is named as non-perturbative QCD (Quantum Chromo Dynamics - the theory describing the strong force). The amount of diagrams, and thus the amount of calculations, increases dramatically when going to higher orders. Thus, in general for the processes relevant at the LHC, only next-to-leading order (NLO) calculation has been made.

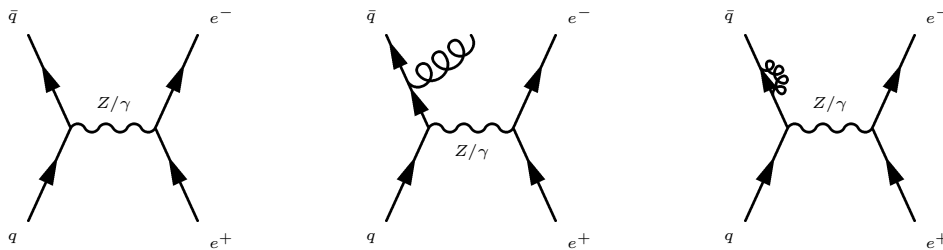


Figure 2.2: Examples of Z/γ production at respectively LO (left), NLO (middle) and NNLO (right).

Symmetries are a cornerstone in the understanding of the standard model and also provide inspiration for models beyond the standard model (e.g. supersymmetry). In the case of particle physics, symmetries refer to transformation of the fields that leave the Lagrangian unchanged. According to Noether theorem, such symmetries are equivalent with conserved quantities (for example translation invariance leads to momentum conservation). One of the most important symmetries within the standard model is known as gauge invariance, thus under any local gauge transformation the Lagrangian has to remain unchanged. The different parts of the standard model are often characterized by which gauge group they belong to. The standard model is thus often written as a $U(1) \times SU(2) \times SU(3)$ theory, the $U(1) \times SU(2)$ being the electroweak theory and $SU(3)$ similar the gauge group for the strong interaction. The choice of gauge group determines the dynamical properties of the theory, and it can be shown that only by requiring the electron field to obey local gauge invariance, it is possible to derive the full QED Lagrangian [6].

2.3 Quantum Chromo Dynamics - QCD

The current understanding of the strong force started with the prediction of the quark by Murray Gell-Mann and George Zweig in 1964. A lot of

⁹Even though it is called a coupling “constant”, it actually varies with the energy scale.

different hadrons were discovered around 1960 and the quark model provided a framework to understand all these: Namely as bound states of quarks. But the existence of quarks was seriously doubted, since no experiments were able to find free quarks. The existence of quarks first became widely accepted after experimental results from SLAC (Stanford Linear Accelerator Center) showing that protons had pointlike charged constituents and secondly a theoretical model (QCD), describing why no free quarks were observed, was developed.

QCD introduces a new quantum number called color charge, which can take three different values - red, green and blue. In QCD the interactions between colored objects are described by the exchange of a gluon, just as the photon describes the interacting between charged objects in QED. Both the photon and the gluon are spin-one massless gauge bosons, thus one could expect the same behavior for QCD as QED. But opposite photons, gluons have color charge themselves and therefore gluon-gluon interactions are possible. This difference leads to two very different theories, which can be seen in the following two phenomena of QCD: Asymptotic freedom and confinement.

Asymptotic freedom is a property of QCD that causes the particles to become “free” at higher energies (or smaller distances), the free refers to coupling constant going to zero for the energy going to infinity. The asymptotic freedom is calculated by help of the so-called renormalization group equation and it can be shown that the coupling constant decreases logarithmic with the energy.

Another consequence of the energy dependency of the coupling constant can be derived by looking at what happens if one tries to separate two quarks: As the distance between the two quarks increases the coupling constant will increase simultaneously and thus the energy required to separate them further will also increase. At some point the energy required becomes so large that it is more profitable to create a new quark anti-quark pair, which combines into two new bound states. This effect is known as confinement and an illustration of the concept can also be seen in figure 2.3.

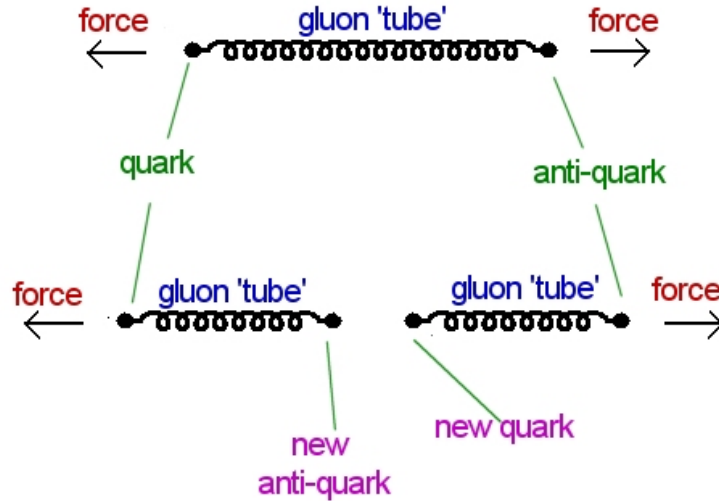


Figure 2.3: An illustration of quark confinement, when trying to separate two quarks a new quark-antiquark pair is created and thus no free quarks can be observed.

2.4 Strange particles

In this thesis I will study the production of K^0 and Λ hadrons¹⁰, which both contain a strange quark. Therefore I will provide a more in depth account of the strange quark, followed up by a description of the K^0 meson and Λ baryon.

2.4.1 The strange quark

The strange quark is, up to all test conducted so far, an elementary particle. It is the third lightest quark and its existence was predicted along with the u and d quarks to explain the many observed hadrons. These three quarks were the only quarks predicted by the first quark models and no additional quarks were needed to explain the so far observed hadrons. It was first later that additional quarks were proposed and discovered [7, 8, 9].

Before the prediction of the strange quark, particles containing the strange quark had already been observed. The first observed strange particle was the kaon, observed in 1947 in cosmic rays. To explain the long lifetime of these newly found particles ($\tau \sim 10^{-11}$ s (weak force) compared with

¹⁰A hadron is a particle composed of quarks and held together by the strong force. The category is often split into three: Baryons (qqq), anti-baryons ($\bar{q}\bar{q}\bar{q}$) and mesons ($q\bar{q}$).

the typical timescale of the strong force $\tau \sim 10^{-23}$ s) a quantum number called strangeness was introduced. Strangeness was designed to be conserved during strong interactions but allowed to break in weak interactions, this has later led to the introduction of quark mixing in weak decays. With the introduction of strangeness, it was possible to order the observed hadrons into what is known as the eightfold way (see figure 2.4, which was one of the building blocks for the quark model).

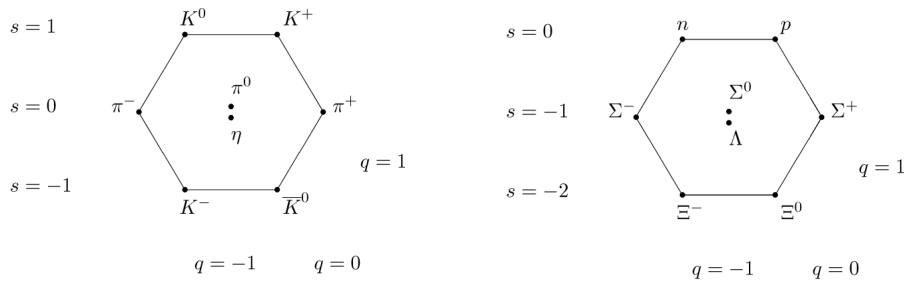


Figure 2.4: The figure shows the meson octet (left) and the baryon octet (right). The horizontal lines have the same strangeness and the diagonals share the same charge.

Since the quarks are confined, the mass of the individual quark is very hard to measure. This leads to a very high uncertainty on the measurement of the mass compared to the mass measurement of final hadron states. The mass of the strange quark is $M_S = 100^{+30}_{-20}$ MeV [10]. The strange quark decays through a charged current reaction and a Feynman diagram of the decay can be seen in figure 2.5.

2.4.2 The K^0 meson

The K^0 meson consists of an anti strange quark and a down quark ($\bar{s}d$) and has the anti particle, \bar{K}^0 , which consists of a strange quark and an anti down

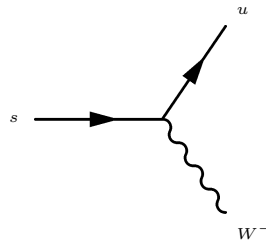


Figure 2.5: A Feynman diagram showing how a strange quark decays.

quark ($s\bar{d}$). The only difference between the quantum numbers of the two states is that K^0 has strangeness 1 and \bar{K}^0 has strangeness -1 . But, since strangeness is not conserved in weak interactions it is possible to switch back and forth between the two different states (see figure 2.6).

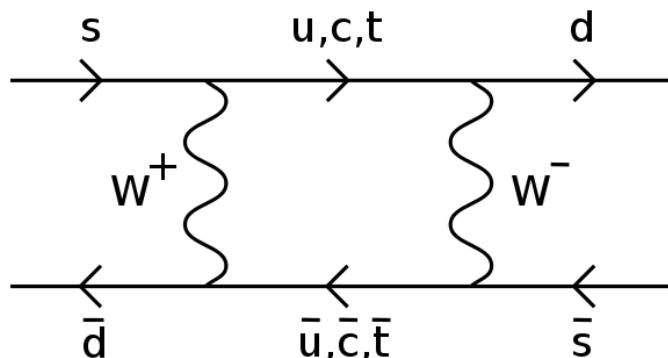


Figure 2.6: The diagram shows how the K^0 and \bar{K}^0 can oscillate back and forth by the exchange of two W bosons.

This leads to what is known as neutral kaon mixing, where the observed particles are a linear combination of the K^0 and \bar{K}^0 (see equation 2.1). The two different combinations were called K-short and K-long, named after their lifetimes. The difference in lifetime is explained by different decay patterns. Even though the two states are very similar, they are in a different CP state¹¹ and since CP violating decays are very suppressed, the final and initial particles will share the same CP eigenvalues. The K-short has a CP number of $+1$ and since the two pion final state ($\pi^+\pi^-$) also has $CP = +1$, the K-short can decay this way. The K-long has $CP = -1$ and thus needs to decay into a three pion final state. Since the mass of three pions is very close to the K-long mass, it will decay significantly slower than the K-short.

$$K_1^0 = \frac{1}{\sqrt{2}} (|s\bar{d}\rangle \pm |\bar{s}d\rangle) \quad (2.1)$$

The mass of the K^0 is $M_{K^0} = (497.614 \pm 0.024) \text{ MeV}$ and the lifetime of the two different states can be seen in figure 2.7, together with the most important decay channels. The decay of interest in this study is the $K_S \rightarrow \pi^+\pi^-$, since the K-long in general will move through the detector before

¹¹The CP state refers to the behavior under the combined charge and parity operator (for more information see the book by B.R. Martin and G. Shaw [11])

decaying and the tracking detector cannot observe the neutral pions (i.e. $K_S^0 \rightarrow \pi^0\pi^0$ cannot be detected). A Feynman diagram of that decay can be seen in figure 2.7.

Decay Process	Branching Ratio
K_S^0	$\tau = (0.8958 \pm 0.0005) \cdot 10^{-10} \text{ s}$
$\pi^0\pi^0$	$(30.69 \pm 0.05) \%$
$\pi^+\pi^-$	$(69.20 \pm 0.05) \%$
K_L^0	$\tau = (5.116 \pm 0.021) \cdot 10^{-8} \text{ s}$
$\pi^\pm e^\mp \nu_e$	$(40.55 \pm 0.11) \%$
$\pi^\pm \mu^\mp \nu_\mu$	$(27.04 \pm 0.07) \%$
$\pi^0\pi^0\pi^0$	$(19.52 \pm 0.12) \%$
$\pi^+\pi^-\pi^0$	$(12.54 \pm 0.05) \%$

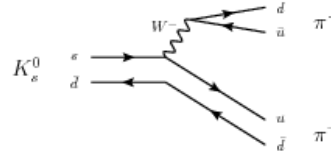


Figure 2.7: The table shows the most important decay modes for the K^0 -long and K^0 -short mesons. The Feynman diagram is the most predominant decay for the K_S^0 .

2.4.3 The Λ baryon

The Λ baryon consists of a u-,d- and s quark and thus has a total charge of zero and a baryon number of one. The anti Λ baryon, the $\bar{\Lambda}$ ($\bar{u}\bar{d}\bar{s}$), again has a charge of zero, but this time the baryon number is minus one and since no forces break the conservation of baryon number, it is not possible to change from a Λ to a $\bar{\Lambda}$ without creating new particles. The mass of the Λ is $M_\Lambda = (1115.683 \pm 0.006) \text{ MeV}$ and the lifetime is $\tau = (2.632 \pm 0.020) \cdot 10^{-10} \text{ s}$. The different decay modes can be seen in figure 2.8, together with a Feynman diagram of the predominant decay mode.

Decay Process	Branching Ratio
$p\pi^-$	$(63.9 \pm 0.5) \%$
$n\pi^0$	$(35.8 \pm 0.5) \%$
$n\gamma$	$(1.75 \pm 0.15) \cdot 10^{-3} \%$

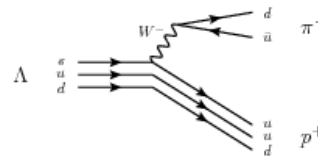
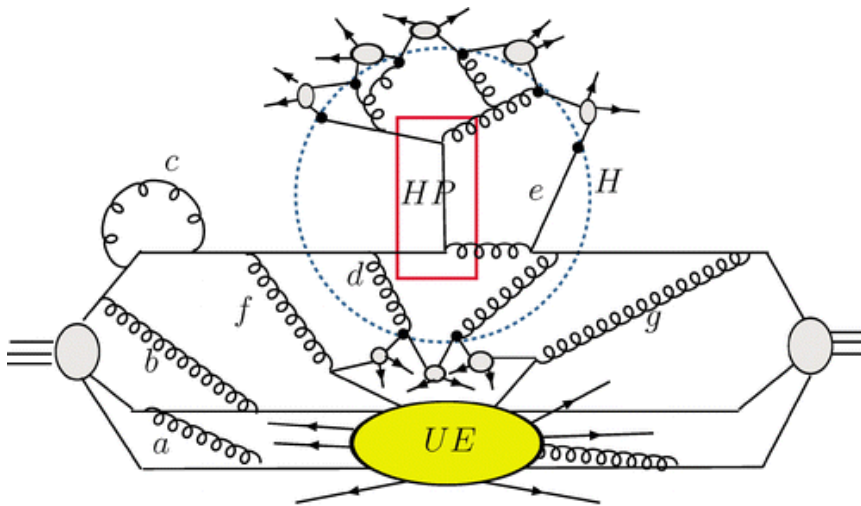


Figure 2.8: The table shows the decay modes for the Λ baryon, and the Feynman diagram shows the most predominant decay mode.

As can be seen in figure 2.8, the predominant decay mode is the $\Lambda \rightarrow p\pi^-$, thus the $\bar{\Lambda}$ will decay to a $\bar{p}\pi^+$, hence it will be possible to separate the Λ and the $\bar{\Lambda}$ particles in the detector.

3 A proton-proton collision

Even with the full knowledge of the standard model it is in no way a trivial matter to describe what happens when two protons collide. This is partly due to the calculations of the SM being cumbersome; especially for higher order amplitudes, where the number of calculations needed increases dramatically. Another challenge is that a lot of the processes are in the non-perturbative QCD area, where it is not possible to use calculations from the standard model. Instead the description of proton collisions relies on different models, which each explains a part of the full collision. In this section I will provide an explanation of the different models and how they together describe what happens in a proton-proton collision.



Mangano ML, Stelzer TJ. 2005.
Annu. Rev. Nucl. Part. Sci. 55:555–88

Figure 3.1: The drawing illustrates the complexity of a proton-proton collision. The final particles (the small lines with arrows) come from different production mechanisms of a proton-proton collision: Hard process (marked with a red square), ISR (the lines marked with letters), FSR (the lines created within the blue circle), hadronization (the small grey dots) and Underlying Event (the yellow ellipse, marked with UE).

In figure 3.1 a drawing of what happens in a proton-proton collision is shown. As can be seen from the figure, a proton-proton collision is rather complex, this is mainly due to the fact that protons are not elementary particles. With the energy available at LHC it is generally the partons inside the proton

that collide and not the protons themselves. But removing a colored object from the proton makes the left over part of the proton, the so called beam remnants (in the figure, the beam remnants are the full drawn lines going from the protons to the UE), colored itself. And since the standard model prohibits us to observe colored objects (the consequence of confinement in QCD), the beam remnants also have to interact (either to form colorless hadrons or to have multiple collisions between the partons of the two protons, known as MPI (Multiple Parton Interactions)). Together this describes what is known as the underlying event.

The collision with the highest momentum transfer between the two partons is known as the hard process. The hard process will often produce a colored particle, which may emit final state radiation (FSR) from the scattered partons and afterwards hadronize¹². The FSR is gluon radiation, the effect is similar to an electron emitting a photon, but it happens more rapidly due to the high coupling constant for the strong force. After going through FSR, the single parton will have turned into several partons called a parton shower. At the end, the colored particles of the parton shower will form colorless hadrons; this process is known as hadronization. It is also possible for the colliding partons to emit gluons before the actual collision, this is known as Initial State Radiation (ISR)¹³.

In the case of collisions resulting in particles with a large transverse momentum, it is possible to treat the different components of a proton-proton collision separately. This can be explained by looking at the different energy scales: The proton energy scale is $\Lambda_{QCD} \sim 200$ MeV, whereas in the hard collision it will be significantly above (e.g. if a Z is produced, the energy scale will be $\sim M_Z$). Thus the timeframe of the hard interaction is much shorter than that of the interactions within the proton and therefore the partons can be assumed to be free. This ends up in what is known as the QCD factorizations theorem, which can be seen in equation 3.1.

$$\sigma_X = \sum_{a,b} \int_0^1 dx_1 dx_2 f_a(x_1, \mu_F^2) f_b(x_2, \mu_F^2) \times \hat{\sigma}_{a,b \rightarrow X} \left(x_1, x_2, \{P_i^\mu\}; \alpha_s(\mu_R^2), \alpha(\mu_R^2), \frac{Q^2}{\mu_R^2}, \frac{Q^2}{\mu_F^2} \right) \quad (3.1)$$

¹²The combination of both FSR and hadronization is sometimes referred to as fragmentation.

¹³Gauge invariance forbids a sharp distinction between FSR and ISR, however radiation parallel with the scattered parton is overwhelmingly FSR and radiation parallel with the beam is only ISR.

x is the fraction of the protons momentum that a single parton carries, μ_F is the factorization scale, μ_R is the renormalization scale and Q is the kinematic scale. The functions f_a and f_b are the Parton Distribution Functions (PDFs) and $\hat{\sigma}$ is the cross section for the hard collision.

3.1 Parton distribution functions

The PDFs describe the probability to take a given parton out of a hadron with a given x -value and at a certain energy scale, called the factorization scale. It is not possible to calculate the PDFs from the standard model, since it belongs to non-perturbative QCD. Instead several groups fit experimental results to obtain the PDFs (MSTW PDF [12] and CT10 [13]). The data used comes from a lot of different experiments and different types of collisions, it includes results from the Tevatron¹⁴ as well as experiments colliding protons with various leptons.

The latest precision measurements for the proton were with the HERA accelerator at DESY. The HERA accelerator collided protons with electrons (or positrons), giving a very good handle on the PDFs through what is known as deep inelastic scattering (DIS).

In DIS the electron will scatter off a single parton and produce an electron plus hadrons (in general the energy of the electron is high enough to break up the proton).

The different partons inside a proton are divided into three types: Valence quarks, sea quarks and gluons. The valence quarks of a proton are the u and d quarks that the proton consist of and classically one would expect the most probable value of the PDFs for the valence quarks to be around $x = \frac{1}{3}$ due to a proton having three valence quarks.

This is however changed due to quantum fluctuations and the PDFs can be seen in figure 3.2. When the valence quarks move around within the

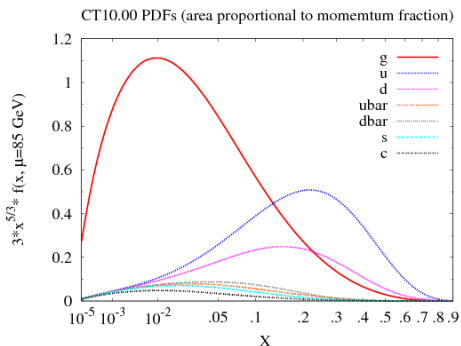


Figure 3.2: The global fit for the PDFs near the W mass scale taken from CT10 [13]. The peak for the valence quarks and the gluon dominance for low x -values can be seen in the figure.

¹⁴ $p\bar{p}$ collider located at Fermilab.

proton, they will from time to time radiate virtual gluons and sometimes these gluons create a virtual quark anti-quark pair (called sea quarks). Thus it is possible to have both gluons as well as all types of quarks colliding in a proton-proton collision, but the production of sea quarks and gluons are mainly in the low x -regime (see figure 3.2). The LHC is sometimes referred to as a gluon-gluon collider, due to the high energy available. For instance consider the production of a W -boson, at 14 TeV the x -value of the two partons is of the order $x \approx \frac{80 \text{ GeV}}{14 \text{ TeV}} = 0.006$, at this x -value the gluon's PDF is clearly dominating.

3.2 The hard interaction

The hard interaction describes the collision of two partons and it is the essential part of the proton-proton collision. It determines whether the collision becomes one of the many collisions with a set of very low transverse momentum particles (soft) or if some of the more rare collisions, such as Higgs production, take place. Essentially all particles with high transverse momentum and high mass are created within the hard interaction, hence the name. Examples of hard interactions can be seen in figure 3.3.

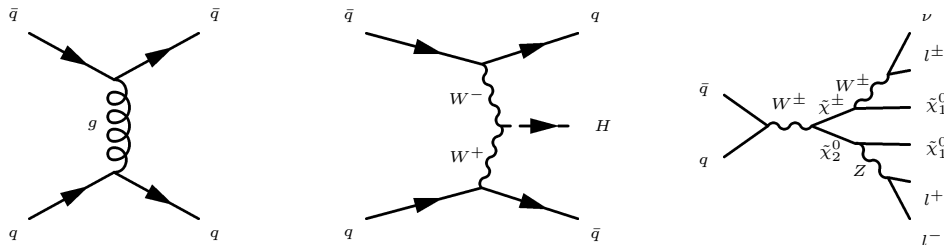


Figure 3.3: Three examples of hard interactions: A gluon exchange (left), the production of a Higgs boson through vector boson fusion (middle) and the creation of two supersymmetric particles, decaying into the lightest supersymmetric particles (right).

The different hard interactions are described by the standard model and their cross sections are calculated through perturbation calculations. Thus it is within the prediction of the hard process that the standard model is put to test¹⁵. Almost all new models beyond the standard model introduce modifications to the modeling of the hard process; in general the new models allow additional hard processes to take place.

¹⁵The prediction of the standard model within the low transverse momentum region has already been tested at previous colliders.

3.3 Soft QCD processes ¹⁶

The soft interactions are often split into several categories depending upon the type of collision. First a separation between elastic and inelastic collisions is made.

In elastic scattering all quantum numbers and masses remain unchanged and only a momentum transfer takes place. Almost no elastic events are observed in the detector¹⁷, since in general the momentum transfer has to be relatively low in order to not break up the protons. This leads to the particles escaping the detector along the beam axis. In addition it is relatively straightforward to remove any elastic events from the detector, if these are unwanted.

Inelastic scattering is every other type of collision. The total cross section can thus be described as the sum of the elastic and inelastic cross sections:

$$\sigma_{\text{tot}}(s) = \sigma_{\text{el}}(s) + \sigma_{\text{inel}}(s), \quad (3.2)$$

where s is the center of mass energy. The inelastic collisions are further divided into diffractive and non diffractive events. Diffractive events arise if the proton is excited but preserves its quantum numbers including its lack of color and then afterwards decay into a spray of particles (see figure 3.4). The diffractive events are categorized according to whether both of the protons decay (double diffractive) or if only one decays (single diffractive). The last type of diffractive events leaves both the protons intact, but creates an excited system that decays (CD).

$$\sigma_{\text{inel}}(s) = \sigma_{\text{ND}}(s) + \sigma_{\text{inel}}(SD) + \sigma_{\text{inel}}(DD) + \sigma_{\text{inel}}(CD) \quad (3.3)$$

Another combination is known as non-single diffractive (NSD), which takes all inelastic collisions except for single diffractive. For a long time the NSD events were the standard for Minimum Bias (MB) studies, but lately all inelastic collisions have been used. The reason for using NSD is the double-arm trigger, requiring activity both in the forward and backward region of the detector.

There are two different approaches to account for different types of diffractive events: The first is to apply additional cuts in the event selection and the

¹⁶This section is inspired by an overview by A. Buckley et al. [14]

¹⁷A new subdetector, ALFA, is however being commissioned to perform such measurements in the ATLAS detector.

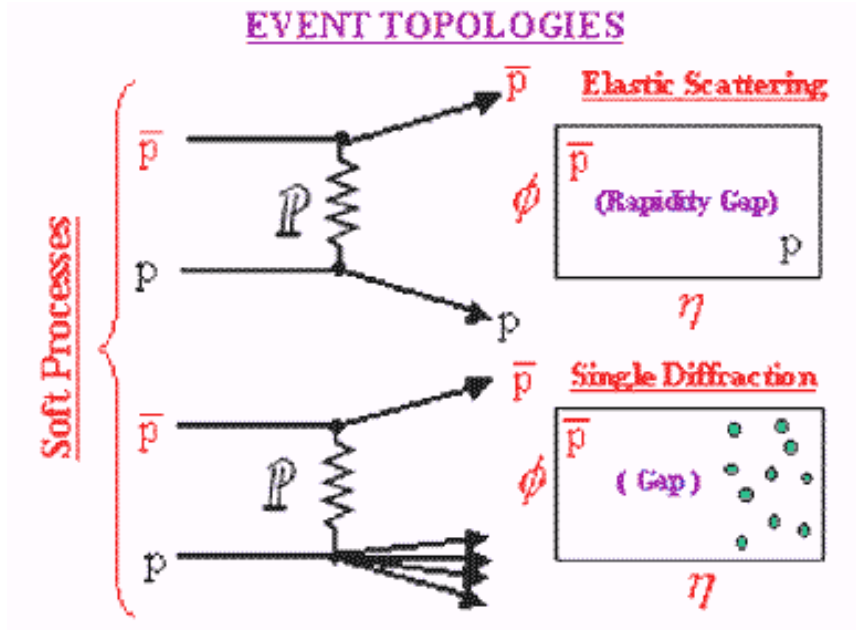


Figure 3.4: Illustration of an elastic (top) and a single diffractive (bottom) proton-antiproton collision. To the right is shown a simplified version of the expected detector response.

second method is to correct the MB selection with the use of MC simulation. Previous to the start of the LHC, the second method was widely used, especially to correct back to NSD events. The problem with the second method is that it is very model dependent, and thus when the model changes the correction has to be remade. At LHC it has been the custom to use the first method, namely to present the data corrected for detector effects, but otherwise as raw as possible and with a minimal model dependency.

3.4 Final State Radiation (FSR) and Initial State Radiation (ISR)

If the created particles from the hard interaction are charged, they may radiate photons. The same holds true for colored particles, but instead of photons they radiate gluons, which may in turn split into more colored partons. The process of going from a single colored object to a spray of particles is called FSR or parton showering. To illustrate how to calculate

the effect of FSR consider the following hard interaction: $e\bar{e} \rightarrow q\bar{q}$ ¹⁸ (see figure 3.5 for the leading order diagram).

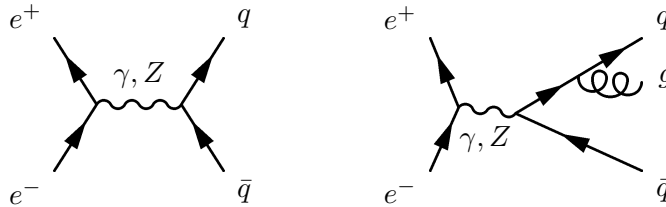


Figure 3.5: The LO Feynman diagram for the process $e^-e^+ \rightarrow q\bar{q}$ (left) and an example of the same process but with an additional gluon emitted afterwards (right).

To start with, consider the emission of an additional gluon. The corresponding Feynman diagram can be seen in figure 3.5 and the cross section is given in equation 3.4,

$$d\sigma_{q\bar{q}g} \approx \sigma_{q\bar{q}} \sum_{Partons} C_F \frac{\alpha_s}{2\pi} \frac{d\theta^2}{\theta^2} dz \frac{1 + (1-z)^2}{z} \quad (3.4)$$

where C_F is a color factor, $\sigma_{q\bar{q}}$ is the leading order cross section, θ is the opening angle between the gluon and (anti-)quark and z is the fraction of the momentum taken by the gluon. The cross section with an additional gluon is proportional to the LO cross section, and therefore it is possible to consider the rest of the cross section as coming from the radiation of a single gluon. By the use of equation 3.4, the full FSR can be calculated as an iteration of single gluon (quark) radiation, where the emitted gluons (quarks) form the basis for additional radiation.

One thing to note about equation 3.4 is that it diverges for $\theta \rightarrow 0$ and $z \rightarrow 0$. Thus the majority of the created gluons will either have a small angle or be soft. The first divergence ($\theta \rightarrow 0$) corresponds to a parton emitting a collinear gluon, but separating two exactly collinear partons is not possible in any physical experiment. Hence by introducing a minimum value for the angle, it is possible to remove the divergency for small angles. This is known as introducing a cut-off, and if the measured scale is larger than the cut-off, the measured results should be almost independent on the cut-off. Another choice for a cut-off could be to require the transverse

¹⁸The $e\bar{e} \rightarrow q\bar{q}$ interaction was chosen over the $q\bar{q} \rightarrow q\bar{q}$ interaction for simplicity, even though the last process would be the relevant one in pp collisions. But the arguments would be very similar in both cases.

momentum of the emitted gluon with respect to the quark to be above a certain threshold, this cut-off removes both the divergencies.

Since all particles can emit additional radiation, one has to be aware of not doublecounting the amount of emitted radiation. An example of doublecounting could be the calculation of the radiation of hard gluon: First the parton is found not to emit any hard gluons, but only a soft gluon. But if one then calculate the probability for the two new partons to emit a hard gluon, the possibility to emit a hard gluon has been calculated twice and thus one time too many. To solve this problem an ordering of the emitted gluons is introduced. Several different orderings are possible; the most intuitive is to require additional radiation to have a lower momentum transfer than the previous. Another possibility is to use the so called coherence-improved parton showers, which is ordered according to the opening angle. Ordering according to the opening angle will often lead to a few soft wide-angle gluons being emitted before the hardest gluon.

Just as the particle can emit a gluon after the collision, it is also possible to radiate gluons before the hard collision takes place, this radiation is known as Initial State Radiation (ISR). It follows the same physical principles as the FSR, but the way it is implemented in the calculations is quite different. The calculations start with the hard process, thus the ISR is calculated backwards. The ISR allows for the colliding partons to start with a higher momentum, but radiate the “extra momentum” away before the hard process. Thus in addition to predicting the extra particles produced, the ISR is also needed to calculate the probability to get the parton needed for the hard process.

3.5 Hadronization

The hadronization describes how the colored partons from the parton shower form colorless hadrons. Hadronization is described through models since it is within the non-perturbative region of QCD. Several models exist with the predominant models being the string model and the cluster model.

The string model¹⁹ connects the outgoing $q\bar{q}$ pairs with a string. If the string becomes too stretched (i.e. the $q\bar{q}$ move too far apart), it will break into a new $q'\bar{q}'$ pair. Continuing until the energy is too low would finish the

¹⁹In this report I will briefly describe the string model, for information about the cluster model see [14, 15]

hadronization, but even through this method is intuitive to understand it is rather cumbersome to do in a simulation. Instead it can be shown that it is possible to iteratively take single hadrons out of the string with the momentum fraction given by equation 3.5 [16],

$$f(z) \propto \frac{1}{z}(1-z)^a \exp -\frac{bm_{\perp}^2}{z} \quad (3.5)$$

where a and b are constants and m_{\perp} is the transverse mass of the hadron.

An additional effect arises due to the tunneling effect of massive particles, this leads to a suppression of heavy quarks $u : d : s : c \approx 1 : 1 : 0.3 : 10^{-11}$ [14]. To explain the production of baryons, the possibility for the string to split into diquark states is introduced.

3.6 The underlying event

The underlying event is everything not related to the hard interaction and the associated ISR/FSR and hadronization²⁰. Thus the underlying event is primarily the result of the interactions between the beam remnants. As already mentioned, the beam remnants will have to interact due to the confinement of QCD. But it is also possible for a parton from each of the protons to make an additional interaction, this is known as multiple parton interaction (MPI). In general the additional interaction will be a soft gluon exchange (see figure 3.3) and the cross section for such a process is given as:

$$d\hat{\sigma} \propto \frac{dp_{\perp}^2}{p_{\perp}^4} \quad (3.6)$$

To control the divergency seen for low transverse momenta, color screening is introduced. The color screening is due to the particles not being able to see the individual partons and thus only interact with the average color field. This leads to a change in equation 3.6: $p_{\perp}^4 \rightarrow (p_{\perp}^2 + p_{\perp 0}^2)^2$, where $p_{\perp 0}$ is a constant describing the momentum at which the color screening starts to become important.

From equation 3.6 it is possible to calculate the number of additional parton interactions per event by dividing the cross section with the total cross section. By assuming a Poisson distribution, it is possible to simulate the number of multiple parton interactions in an event generator. After the

²⁰Different definitions exist, the main difference often being on whether or not to include the ISR in the underlying event.

interactions the partons will go through ISR/FSR and hadronization.

Since the protons are not pointlike but have a finite size, it is possible for the protons to hit with different centralities. Theoretically this is described by a quantity called impact parameter, which is the transverse distance between the two centers. The event generators have to include this, by changing the average number of interactions depending upon the impact parameter. The exact function depends upon the spatial distribution of the partons within the proton, this distribution is not known and different models are used to describe it.

After the multiple parton interactions, there will still be left over partons within the “proton”. These partons will be given a transverse momentum, $P_t \sim \Lambda_{\text{QCD}}$ and afterwards be treated equally to the scattered partons. The argument for providing the transverse momentum boost is Fermi motion within the proton, resulting in a small motion perpendicular to the beam.

4 Event generators

As the name suggests, the event generators are used to create simulations of particle collisions, the so-called events. In an experiment the accelerator provides the particle collisions and the detector observes what happens. Similar in simulations, the event generator provides the particle collisions and the detector simulation gives the expected response in the detector. To obtain this, the event generators use Monte Carlo (MC) techniques to simulate the randomness observed in the collisions, hence event generators are often called MC simulations²¹. The main aspects of the physics behind the event generators are described in the previous section (section 3). Event generators are used in several different parts of the experimental process:

- To design the detector such that the relevant physics can be observed.
- To inspire the different analysis strategies on where to look for new physics.
- To correct the data for detector acceptance and efficiency²²
- To compare the experimental observations with theoretical models (most likely the SM).

In this report, the event generators are used to correct for detector effects and to compare the experimental results with theory (since the detector is already built and the analysis strategy follows similar ideas as the standard underlying event studies). Several different event generators exist, with a slightly different implementation of the physics described in section 3. In proton-proton collisions, the most used event generators are PYTHIA [17], HERWIG [15], PHOJET [18] and SHERPA [19]. All of these event generators are full event generators, in the sense that they can simulate complete events. Other generators only simulate part of the event; often they simulate the hard interaction and have to be supplemented by one of the full event generators to simulate the fragmentation. Examples of these generators are MADGRAPH, COMPHEP and MC@NLO. In this report only PYTHIA, PHOJET and HERWIG are used, thus I will provide a brief introduction to these.

The PYTHIA event generator is probably the most used event generator

²¹The two names “MC simulations” and event generators will often be used interchangeably throughout this thesis

²²This is often in combination with the full detector simulation.

in the study of LHC physics and it has also been used both at LEP (e^+e^- collisions) and HERA (ep collisions). It started in 1978 with the JETSET event generator which was later converted into PYTHIA. It applies the Lund Model of string fragmentation for the soft processes described in the previous section. For the hard processes it only includes LO calculations. In the parton showering, p_\perp ordering is used in both ISR, FSR and MPI. This allows the three different components to be implemented in a common p_\perp ordering. Two different tunes of Pythia were used, the MC09 tune [20] and the Perugia tune [21]. The MC09 tune was optimized to the Tevatron data using both MB and UE studies, whereas the Perugia0 tune only used MB data to tune the soft-QCD.

PHOJET is a MB event generator for collisions between protons and photons ($pp, \gamma p$ and $\gamma\gamma$). It builds upon the Dual Parton Model (DPM) [22] by the exchange of pomerons. A pomeron is a colorless and chargeless particle. Hence it can be used to describe elastic scattering, as well as diffractive scattering, since it only carries momentum between the two protons. Soft and hard interactions are calculated in a similar framework allowing the possibility to have both in a single event.

The HERWIG event generator works very similar to the physics outlined in the previous section. It contains a large amount of LO processes, as well as an interface to import hard processes from other generators. In addition, the HERWIG incorporates NLO correction to the parton showering for several processes. The ordering used in the parton showering follows a new variable \tilde{q} [23]. This ordering is an enhancement of the angular ordering, by also considering the p_\perp of the created particles. HERWIG implements the cluster hadronization model, instead of the string model.

4.0.1 Tuning of event generators

The different models introduce several parameters which cannot be calculated from theory. Instead the parameters have to be tuned from experiments. Some of the parameters are measured to high precision in earlier experiments and are listed in the PDG (Particle Data Group) database [10]. The database includes for instance the masses and lifetime of the hadrons and their different decay channels. But even after fixing these parameters, a large number of variables still need to be tuned. To accomplish the tuning, the variables are separated according to which part of the event generator they influence. The majority of the variables only

control small and often exclusive area of the event generators, which leads to a factorized approach to the tuning of the parameters. In addition to this separation, the variables are sorted according to their influence on the final model such that the most important variable is tuned first, followed by the second most important and so on.

The data used for tuning combines results from both e^+e^- (LEP) and pp (LHC) ($p\bar{p}$ (Tevatron)) colliders. Since the starting point in e^+e^- collisions are elementary particles, it is very useful in describing the produced jets. For instance the $e^+e^- \rightarrow Z/\gamma \rightarrow q\bar{q}$ produces exactly two jets back-to-back and no contamination from other sources affects the jets. Hence studying the shape of the jet provides very good opportunities to tune the FSR, hadronization and any physics process after the initial creation of the two colored particles. However, one should note that the jets created in e^+e^- collisions always are initiated by a quark, whereas in pp collisions it is much more frequent to have jets initiated by gluons. The production ratios of the different hadrons (e.g. $\frac{K^0}{\pi^\pm}$) are tuned according to the relative multiplicities observed at LEP.

The tuning of the underlying event has to be made with distributions from pp ($p\bar{p}$) collisions, since it is not present in e^+e^- collisions. Before the start of the LHC, this was achieved by using data from D0 and CDF²³. After the start of LHC several tunes using both data from Tevatron and LHC have been made [24, 21]. The distributions used to describe the underlying event are described in section 5. In addition to the specific UE distributions, several distributions describing the inclusive events are used. These contain the $\frac{dN_{\text{ch}}}{d\eta}$, $\frac{dN_{\text{ch}}}{dp_T}$, $\langle p_T \rangle$ vs. N_{ch} and multiplicity distributions. The different distributions are measured in different part of phase-space (e.g. $N_{\text{ch}} > 1$, $N_{\text{ch}} > 6$, $p_T > 100 \text{ Mev}$ or $p_T > 500 \text{ Mev}$) resulting in more than one hundred different distributions being used in the final tuning.

²³The two experiments located at Tevatron.

5 Studying the underlying event

To study the Underlying Event (UE), one looks at the general event structure and specific regions sensitive to the UE. This is needed, since it is not possible directly to determine whether a particle comes from the UE or from the hard interaction. In general the hard interaction will produce the jet with the highest energy (this jet is referred to as the leading jet) and due to fragmentation, additional particles associated with the hard interaction will be produced in the proximity of the leading jet. The hard interaction has to fulfill momentum conservation, thus particles will also be produced in the opposite direction of the leading jet. The momentum conservation happens within the rest frame of the hard interaction, and since this frame is often boosted along the beam axis it is not possible to find the opposite direction in the θ coordinate (or η ²⁴). Instead the difference in the azimuthal angle between the particle and the leading jet is used to divide the phase-space into three regions, the toward region, the transverse region and the away region (see figure 5.1). The toward region is $|\Delta\phi| < \frac{\pi}{3}$, the transverse region is $\frac{\pi}{3} < |\Delta\phi| < \frac{2\pi}{3}$ and the away region is $\frac{2\pi}{3} < |\Delta\phi|$.

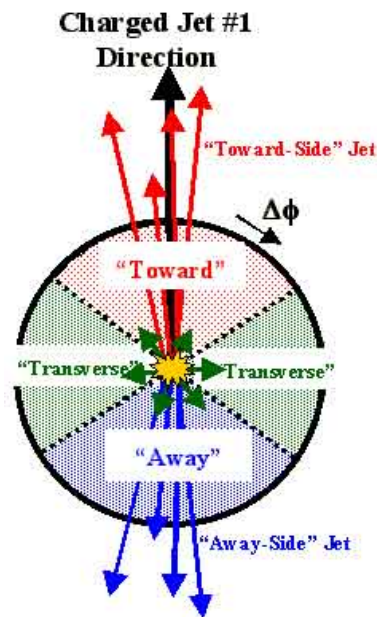


Figure 5.1: Phase-space is split into three different regions, according to the difference in azimuthal angle between the leading jet and the particle.

Since the UE is not correlated with the hard interaction, the particles created in the UE will be produced uniformly in the three regions. The particles from the hard interaction are mainly present in the toward and away regions, hence the transverse region is the most sensitive to the UE.

The observables used to study the underlying event are the $K_S^0(\Lambda)$ angular

²⁴ η is the pseudo rapidity, which is defined as $\eta = -\ln \tan\left(\frac{\theta}{2}\right)$

multiplicity density with respect to the leading jet ($(\frac{1}{N_{\text{evt}}}) \frac{d^2 N(K_S^0)}{d\Delta\phi d\eta}$ vs. $\Delta\phi$), the multiplicity density as a function of the leading jet p_T ($(\frac{1}{N_{\text{evt}}}) \frac{d^2 N(K_S^0)}{d\Delta\phi d\eta}$ vs. $p_T^{\text{leading jet}}$), the average momentum as a function of the leading jet p_T ($\langle p_T \rangle$ vs. $p_T^{\text{leading jet}}$) and the scalar sum p_T as a function of leading jet p_T ($(\frac{1}{N_{\text{evt}}}) \frac{d^2 \sum_{K_S^0} p_T}{d\Delta\phi d\eta}$ vs. $p_T^{\text{leading jet}}$).

5.1 Previous studies of the underlying event

The study of the UE using charged tracks has been carried out at the LHC collider by both the ATLAS experiment [25] and CMS experiment [26, 27] at 900 GeV and 7 TeV. In addition the UE has also been measured for neutral particles by the use of calorimeter clusters by the ATLAS collaboration [28]. Since the different approaches overall show very similar results, I will only summarize the results by the ATLAS experiment using charged tracks and only at an energy of $\sqrt{s} = 7$ TeV. The angular multiplicity density can be seen in figure 5.2 together with several different MC simulations.

For low momentum leading tracks the distribution of tracks is almost flat in the azimuthal angle, whereas the jet shape (the peak around $\Delta\phi = 0$) becomes much more apparent for higher momentum leading tracks. This can be explained by the higher number of particles created in harder jets and the fact that the UE starts to saturate for higher $p_T^{\text{leading track}}$ (see figure 5.3). The MC simulations do not describe the shape of the distribution very well; in general they predict too few particles in the underlying event. This effect becomes more apparent as the leading jet momentum is increased.

The three different distributions for the UE in the transverse region can be seen in figure 5.3. The saturation of the number of particles can clearly be seen, as it becomes almost constant for $p_T^{\text{leading track}} > 5$ GeV. The reason for this shape is that events with a low leading track momentum in general comes from peripheral collisions, whereas the central collision in general produces events with a higher $p_T^{\text{leading track}}$, which leads to a higher particle production. But at some point, the collisions are central and the reason for the higher leading track momentum is due to the PDFs. Since the UE is only influenced by how central the collisions are, the UE will become flat above a certain energy, this effect is known as saturation.

The MC simulations predict around 10 – 15 % too few particles in the transverse region, except for the PHOJET model which predicts 40 % too

5.1 Previous studies of the underlying event

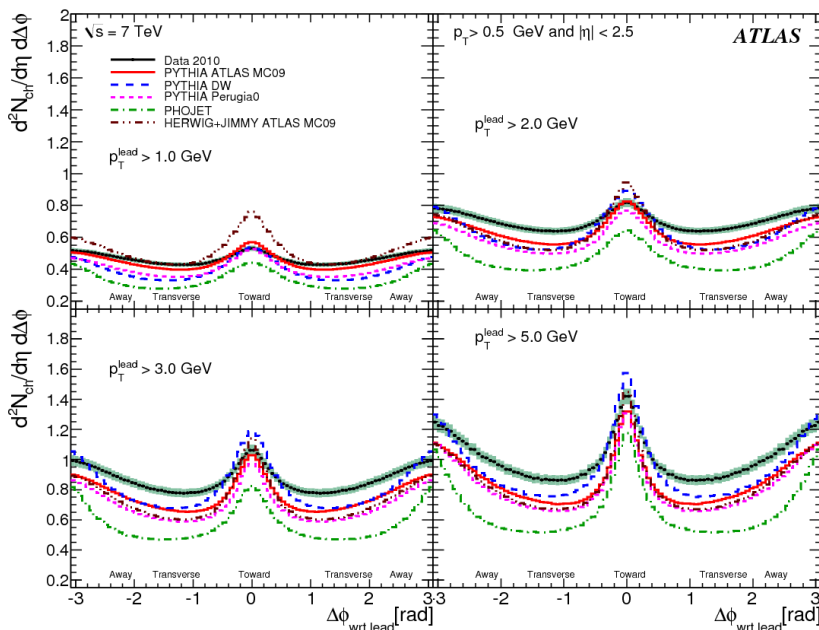


Figure 5.2: ATLAS data at 7 TeV corrected back to the particle level, showing the $\Delta\phi$ distribution of charged particle densities $\frac{d^2N_{ch}}{d\eta d\Delta\phi}$ with respect to the leading charged particle (at $\Delta\phi = 0$), for $p_T > 0.5$ GeV and $|\eta| < 2.5$. The leading charged particle is excluded. The data are compared to MC predictions by the Pythia ATLAS MC09, DW and Perugia0 tunes, the Herwig+Jimmy ATLAS MC09 tune, and Phojet. The distributions obtained by restricting the minimum leading charged particle p_T to different values are shown separately. The plots have been symmetrized by reflecting them about $\Delta\phi = 0$. The error bars show the statistical uncertainty while the shaded areas show the combined statistical and systematic uncertainty corresponding to each p_T lower cut value. (Caption and figure taken from reference [25])

few particles. The same behavior is seen for the scalar sum of the transverse momentum, whereas the average transverse momentum fits decently the data. Several new tunes have been introduced to the different MC models and are now better suited to fit the data (for examples see the new ATLAS tunes [29]).

5.1 Previous studies of the underlying event

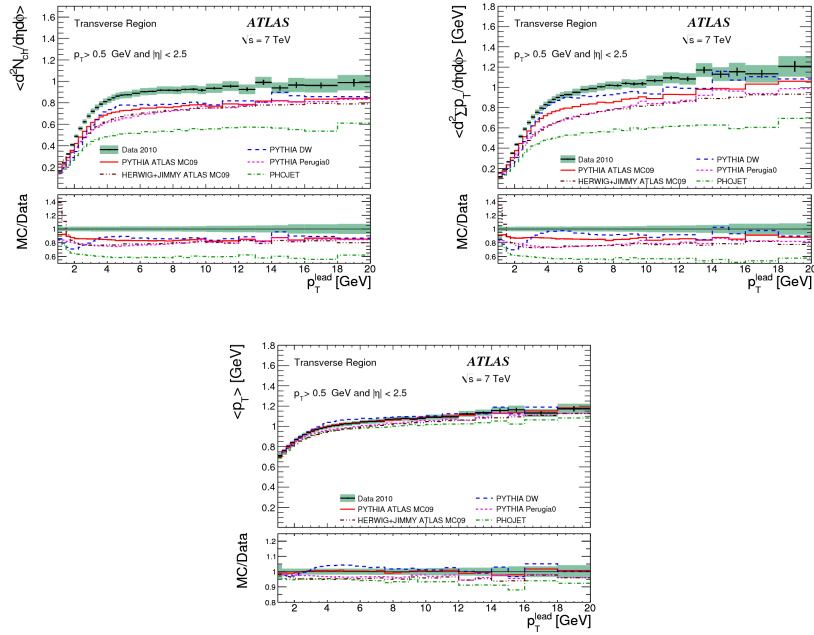


Figure 5.3: ATLAS data at 7 TeV corrected back to particle level, showing the density of charged particles against the leading track momentum (top left), the scalar P_T sum of the charged particles against the leading track momentum (top right) and the mean p_T of the charged particles against the leading track momentum (bottom), for charged particles with $p_T > 0.5$ GeV and $|\eta| < 2.5$. The data is compared with Pythia ATLAS MC09, DW and Perugia0 tunes, Herwig+Jimmy ATLAS MC09 tune, and Phojnet predictions. The error bars show the statistical uncertainty while the shaded area shows the combined statistical and systematic uncertainty. (Caption and figure taken from reference [25])

6 The Large Hadron Collider

The Large Hadron Collider is the latest addition to the particle accelerator complex based at CERN²⁵. The Large Hadron Collider is a twenty-seven kilometer long tunnel located just underneath the Swiss/French border. Starting from a bottle of Hydrogen the protons will travel through a complicated system of particle accelerators before colliding inside the LHC with almost the speed of light (see figure 6.1).

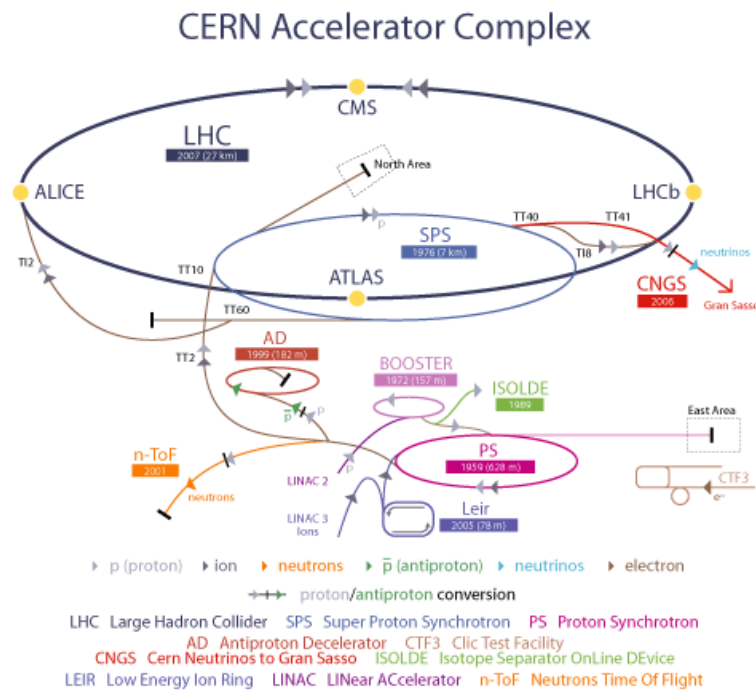


Figure 6.1: The CERN accelerator complex with all its different accelerators shown.

To obtain the protons, the electrons are stripped from the hydrogen atoms by applying an electrical field. The first accelerator is a linear accelerator (LINAC2) providing the initial boost and injecting the protons into the PS booster (the energies can be seen in table 6.1). From the PS booster the protons will travel to the PS (Proton Synchrotron) before entering the SPS (Super Proton Synchrotron). In the SPS the protons will be accelerated to an energy of 450 GeV before being injected to their final destination: The

²⁵Conseil Européen pour la Recherche Nucléaire

LHC. After arriving in the LHC the protons will be accelerated to their final energy in approximately twenty minutes. For the next hours the protons will collide within LHC ring until they are dumped²⁶ and the process starts over.

Accelerator	Energy
LINAC2	50 MeV
PSB	1.4 GeV
PS	25 GeV
SPS	450 GeV
LHC	7 TeV(*)

Table 6.1: The energy after each accelerator. (*) The current energy, it is expected to be increased to 14 TeV in 2014 after a 15 month long shutdown period.

The design energy of the LHC is $\sqrt{s} = 14$ TeV and the nominal instantaneous luminosity is $L = 10^{34} \text{ cm}^{-2}\text{s}^{-1}$. Due to an accident in September 2008 the LHC has only been running with half the nominal energy, $\sqrt{s} = 7$ TeV, and will continue with this energy until the end of 2012. Afterwards a shutdown for around 15 months is needed to bring the LHC up to full energy. The goal was to gather data corresponding to an integrated luminosity of 1 fb^{-1} in 2011 and hopefully be able to gather 5 fb^{-1} before the shutdown.

However, the LHC has throughout 2010 and 2011²⁷ already delivered a total of 2.59 fb^{-1} . The amount of collected data can be seen in figure 6.2. With a maximum instantaneous luminosity of $L = 2.37 \cdot 10^{33} \text{ cm}^{-2}\text{s}^{-1}$, the current hope is to double the amount of data before the end of this year.

6.1 The four major experiments at LHC

There are four major physic experiments studying the collisions provided by the LHC, namely ALICE, ATLAS, CMS and LHC-B. The ATLAS and CMS experiments are multipurpose experiments designed to study the standard model and a general spectrum of theories beyond the standard model. The ALICE experiment focuses on heavy ion collisions, and from these they try to understand the created Quark-Gluon Plasma. As the name suggest LHC-

²⁶Either as a safety measure or because the luminosity becomes too low

²⁷Up till 1. September 2011

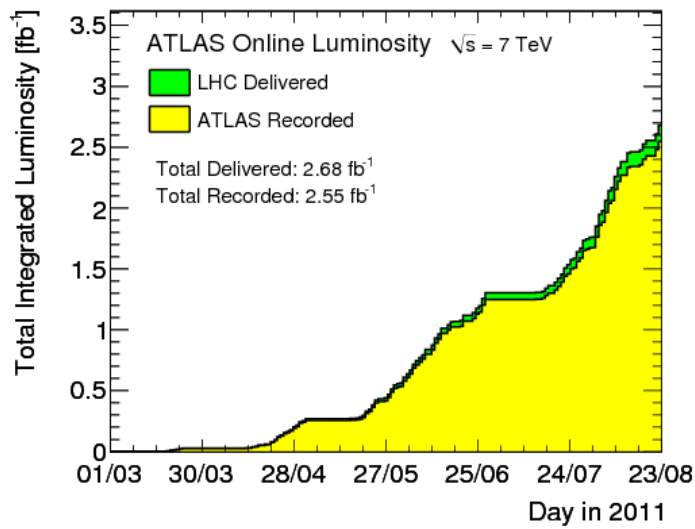


Figure 6.2: The integrated luminosity recorded by the ATLAS experiment in 2011.

B studies the b-quark, where especially CP-violation is an exciting topic for finding physics beyond the standard model.

7 The ATLAS Detector

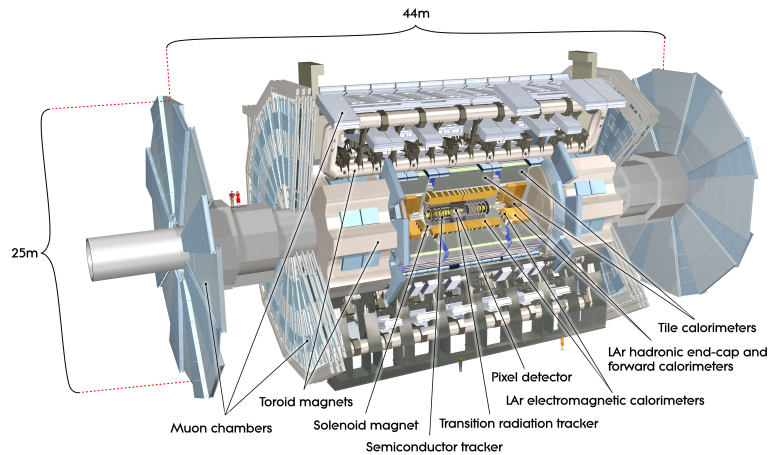


Figure 7.1: The ATLAS detector [30].

The ATLAS (A Toroidal LHC ApparatuS) detector is with a length of 44 meters and a height of 25 meters the largest of the detectors at LHC. The design of the detector follows the standard onion-shape with tracking detectors in the center, followed by calorimeters (electromagnetic and hadronic) and last muon chambers. The inner tracker provides a measurement of the momentum of charged tracks as well as the position of the primary vertex. Due to the close position of the inner most layer to the beam, it is also possible to distinguish secondary vertices from the primary vertex even for small separations, and this is used for particle identification (for example b-tagging of jets). The energy of the particles (except for the muon and neutrinos) is measured in the calorimeter, which is separated into two parts (the electromagnetic calorimeter and the hadronic calorimeter) allowing one to distinguish between electrons/photons and hadronic jets. The muon chamber is used to identify muons as well as provide a more precise measurement of their momentum. The identification is in principle straight forward, since muons should be the only known SM particles producing a signal in the muon chambers²⁸. A simplified version of how particle identification is achieved is drawn in figure 7.2.

²⁸The neutrinos do not at all interact with the detector, and all other SM particles should be stopped before reaching the muon calorimeter.

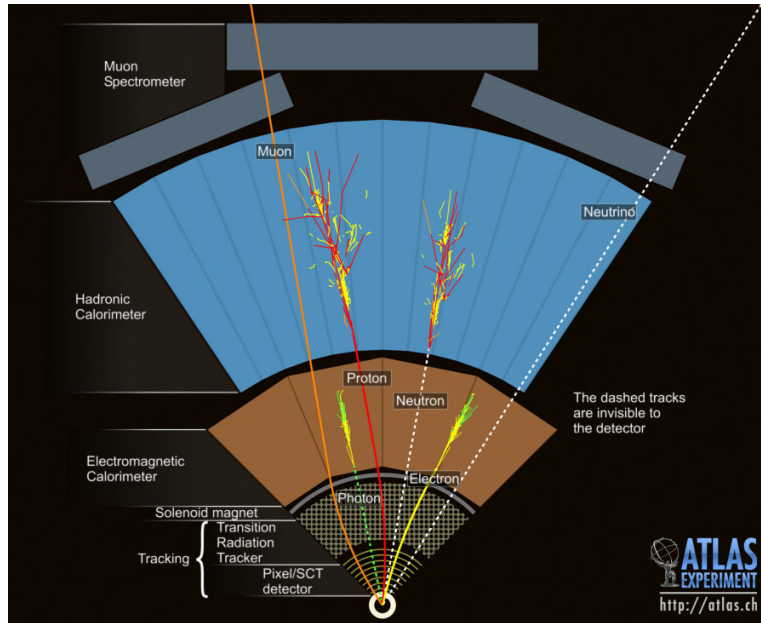


Figure 7.2: The detector signatures of different particles traversing the ATLAS detector.

With this architecture of the ATLAS experiment, it will be possible to conduct a wide range of different searches for anything beyond the standard model as well as precision measurements of known SM processes. The ATLAS detector is therefore referred to as a general purpose detector. In this thesis I will only study data gathered with the inner detector, thus I will only describe this part of the detector in details (for further information about the calorimeters and muon chambers refer to the general description of the ATLAS detector [31]).

7.1 Measuring charged particles

Charged particles travelling through the detector will deposit energy according to the Bethe-Bloch formula [32]. The deposited energy will depend upon the type of particle, type of material and the speed of the particle.

In the case of a silicon detector, several electron/hole pairs will be created by the deposited energy [33]. By counting the number of electron/hole pairs, it is possible to determine whether a particle hit the detector or not and also measure the amount of energy deposited. For low momentum particles, the deposited energy can be used to identify different hadrons (e.g. pions and kaons). The different hadrons can be identified in figure 7.3 if the momentum

is below ≈ 0.5 GeV. For higher momenta, the particles deposit almost the same energy and are therefore indistinguishable by this method. Particles in the high momentum region are called minimum ionizing particles (MIPs); the name refers to the minimum in the Bethe-Bloch formula.

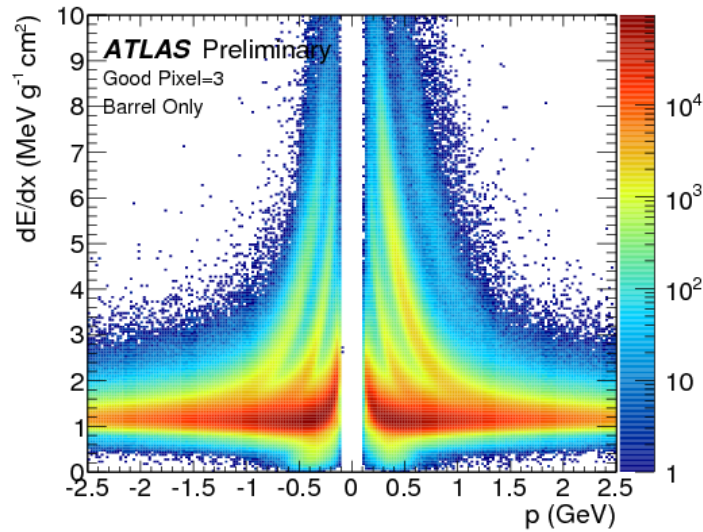


Figure 7.3: Scatter plot of the deposited energy divided by the transversed distance and the particle momentum. The vertical lines in the lower momentum region are due to different types of particles. The three lines are respectively for pions, kaons and protons. The horizontal line is from minimum ionizing particles.

A gas detector works by measuring the ionization of particles travelling through the gas. By applying an electric field, the free electrons, created by ionization, will drift towards the electrode allowing the amount of ionization to be measured. The initial electrons will create an avalanche amplifying the otherwise small signal multiple times (The number depends on the voltage as well as other detector specific parameters, but it varies between $10^4 - 10^6$ for proportional chambers [33]). The standard gas detector has a lower resolution than a silicon detector, but it is cheaper and has a lower material budget.

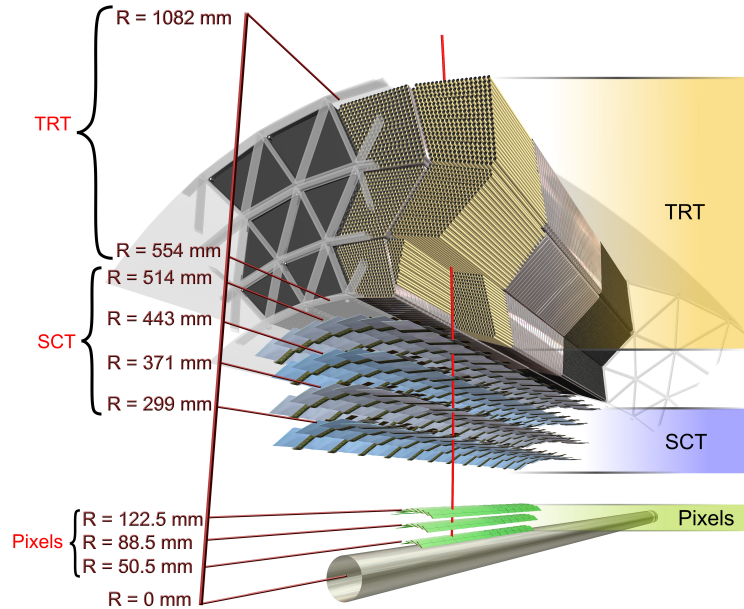


Figure 7.4: The different parts of the ATLAS inner detector. The pixel and SCT are silicon detector, whereas the TRT is a gas detector.

7.2 The Inner Detector²⁹.

The inner detector consists of two types of silicon detectors (pixel and SCT) and a Transition Radiation Tracker (TRT) (see figure 7.4). It covers the region $|\eta| < 2.5$ ($\eta = 2.5$ corresponds to $\theta = 9.4^\circ$) and has a full azimuthal coverage, allowing only particles moving along the beam direction to escape undetected. The central part of the inner detector ($|\eta| < 1$) is called the barrel region and the parts in the two forward regions are called endcaps. The inner detector is placed within a 2 T axial magnetic field, thus particles travelling through the inner detector will follow a helix trajectory. The momentums of the particles are determined by measuring the radius of the helix trajectory, which is proportional to the momentum [33].

²⁹The different numbers used in this section is taken from the ATLAS collaboration [31]

7.2.1 Silicon pixel detector

The innermost part is the silicon pixel detector, which (with its three layers of pixel) provides very precise measurements of spatial position of the particle hits in both the $(r - \phi)$ -plane and along the beam axis. Each pixel³⁰ has a size of $50 \times 400 \mu\text{m}^2$, resulting in a resolution of $10 \times 115 \mu\text{m}^2$. The closest layer is called the b-layer and is located 50.5 mm from the collision point. This layer is very important in the reconstruction of the vertex position and potential secondary vertices (these are used in the identification of b-quarks, hence the name of the layer). The two other layers are located respectively 88.8 mm and 122.5 mm from the beam position. It would not be possible to continue the use of a pixel detector throughout the full detector, due to the electronic readout. Each pixel has to be readout individually resulting in a total number of $80 \cdot 10^6$ channels, just in the three pixel layers installed.

7.2.2 Silicon strip detector (SCT)

The silicon strip detector (SCT) is made of 4 double layers, thereby measuring up to a maximum of 8 spacepoints. The spatial resolution of the SCT in the $r - \phi$ plane is almost as good as for the pixel detectors, namely $17 \mu\text{m}$. It is possible to measure the z-position by introducing a stereo angle of 40 mrad between the strips, though the resolution in the z-direction ($580 \mu\text{m}$) is significantly worse compared to the pixel detector. The loss in z-resolution is of less importance, due to the particle's momentum being measured in the $r - \phi$ plane.

7.2.3 Transition Radiation Tracker (TRT)

The TRT is the outer most part of the inner detector. It consists of a lot small tubes filled with gas. The TRT's spatial resolution is worse than for the silicon detectors, but the number of measurements and the larger size of the detector make it useful in measuring the momentum. In addition, the TRT provides electron identification based upon transition radiation. Ultra relativistic particles moving from one material to another (and thereby between two different refraction indexes) will have a probability to emit a photon; these photons are called transition radiation. Being the lightest of the charged particles, the electrons will have a higher γ -factor for similar momenta and thereby produce more transition radiation [33]. An overview of the different spatial resolutions can be seen in table 7.1.

³⁰The numbers given are within the barrel region, for the end caps see table 7.1.

Item	Intrinsic Accuracy [μm]
Pixel	
Barrel	10 ($r - \phi$) 115 (z)
Endcaps	10 ($r - \phi$) 115 (r)
SCT	
Barrel	17 ($r - \phi$) 580 (z)
Endcaps	17 ($r - \phi$) 580 (r)
TRT	130

Table 7.1: Overview of the expected detector resolutions for the inner detector

7.2.4 Material budget

One of the major concerns when designing the inner detector is the material budget. The aim is to keep the amount of material in the inner detector as low as possible such that it interacts the least amount possible with traversing particles. If too much material is present, the showers seen in the calorimeter will already have started before entering the calorimeter and thus the energy measurements will be biased. In figure 7.5 the material budget for the inner detector is shown and one thing to note is that not only the active detector elements, but also services, electronics, cooling, etc. contributes to the material budget.

7.2.5 Track reconstruction

The track reconstruction combines both the pattern recognition and the final track fitting. Previously the pattern recognition and the track fitting were often separated, but modern algorithms combine them into one common algorithm. The pattern recognition combines hits in the detector into track candidates. The track candidates are then fitted to obtain the physical parameters of the track. The tracks are parameterized as function of d_0 , z_0 , ϕ_0 , θ_0 and $\frac{q}{p}$, where d_0 , z_0 are respectively the distance perpendicular to the beam axis, the distance along the beam axis at the closest point towards the beam axis and $\frac{q}{p}$ is the charge divided by the momentum.

Most of the modern track algorithms build upon the Kalman filter [34]. The Kalman filter is an estimator, i.e. it estimates parameters from inaccurate data. It is designed to optimize the mean square error of the estimated parameters in the case of Gaussian errors. If the errors are non Gaussian, it is the best linear estimator.

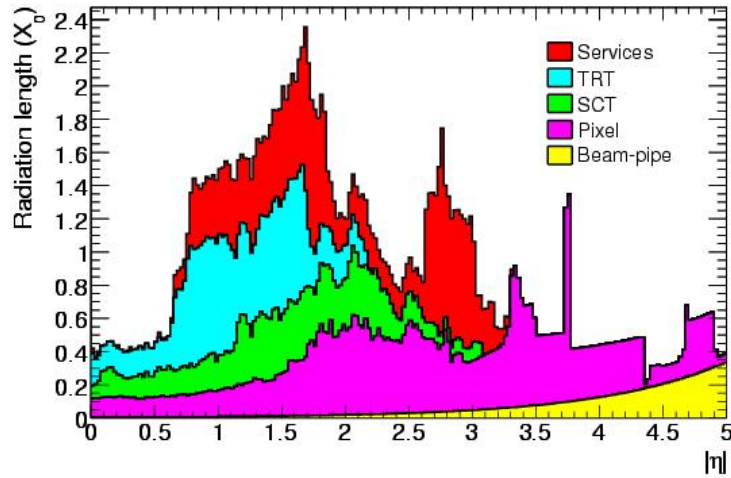


Figure 7.5: The material budget of the inner detector separated into the contribution from the different subdetectors. Since the central region (pseudorapidity close to zero) is the most sensitive region to new physics, the detector is designed with a low material budget in this region.

The Kalman filter starts with an initial guess from the track seed and adds the additional points afterwards³¹. It works by first predicting the next point and then compares the prediction with the measured point to give a new estimate for the track parameters:

- Extrapolate the state vector³² to the next point.
- Predict the next point to be measured from the estimated parameters.
- Calculate the variance between the predicted and the measured point.
- Calculate the Kalman Gain function, which describes how much the new point changes the state vector.
- Calculate the new state function incorporating the newly measured point.
- Update the covariance matrix

After all the points are added, an additional smoothing is applied. The smoothing uses the information from all the points to recalculate the

³¹For a full description of how the Kalman filter technique is used in track reconstruction see Frühwirth et al. [34]

³²For track reconstruction the state vector contains the track parameters.

prediction of the individual points, which again is used to correct the state function. The smoothing is applied in the opposite direction of the Kalman filter; hence if the track is calculated inwards out, the smoothing is applied outwards in.

In addition to estimating the track parameters, the Kalman filter also provides pattern recognition, since it predicts the position of the next point. By looking in the neighborhood of the prediction in the detector, it is possible to find the hits belonging to the track and thus produce the track candidates. Since the Kalman filter also provides the track parameters it fulfils both the pattern recognition and track fitting required in a full track reconstruction.

The Kalman filter is recursive so the individual points can be added separately compared to a global fit where all the data needs to be available. This makes it faster than the global fitting method. Due to the amount of tracks created in the ATLAS detector, the speed of the algorithm is very important. The algorithm implemented in the ATLAS reconstruction software can reconstruct about one event per second on a standard computer [35].

The ATLAS track reconstruction runs the Kalman filter twice, first inside-out and then outside-in. As the name suggest the inside-out sequence starts with the pixel detectors and then move outwards to the SCT/TRT. Since the pixel detector provides three-dimensional space points, the initial track recognition is easier in the pixel detector than in the TRT. The outside-in sequence is needed to find tracks coming from particle decays, examples being K_S^0 and Λ . Also particles with a high energy loss, often electrons, might lead to an extrapolation of the track into a wrong area of the SCT and TRT detector, resulting in the track not being reconstructed.

7.2.6 Tracking resolution

Figure 7.6 show the relative transverse momentum resolution and the transverse impact parameter, d_0 , resolution. For low momentum tracks, the major contribution to the resolutions is from multiple-scattering, where as for high momentum the resolution is dominated by the intrinsic detector resolution. The resolution on the transverse impact parameter gives a simplified estimate on the scale for the minimum separation of vertices the inner detector can distinguish and this parameter is therefore very important in b-tagging and tau identification.

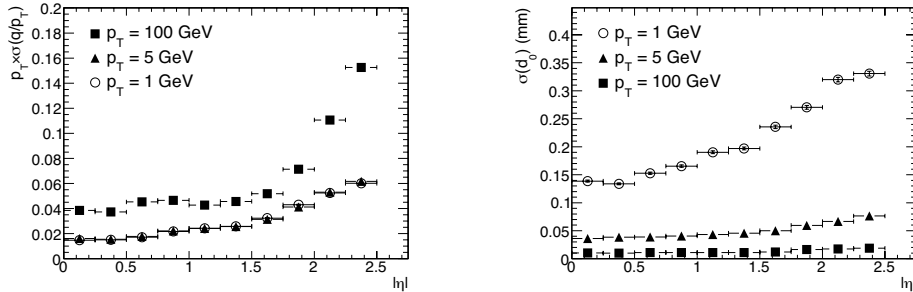


Figure 7.6: The relative transverse momentum resolution for muons (left) and the transverse impact parameter resolution for pions (right). Both of the resolutions are shown for three different energies.

7.2.7 Vertex Reconstruction

If two or more track points towards a common point, the point is referred to as a vertex. It often indicates that the tracks originate from the same interaction or decay. Most of the tracks will point towards the collision point between the two protons; this point is known as the primary vertex. All other vertices are referred to as secondary vertices and come from either particle decays or interactions between particles and the detector.

The vertex reconstruction starts with all tracks likely to originate from the collision point, where a common fit to a single vertex is made. Outliers from the found vertex are removed and used as seeds for possible new vertices. This process continues until all vertices are found. Different fitting routines are implemented in the ATLAS framework to determine the vertex [36]. The most widely used fitting routine is the one proposed by P. Billoir [37], which uses all the track parameters and the covariance matrix for the tracks. The track parameters, \mathbf{q}_i , can be calculated as a function of the vertex position, \mathbf{V} , and the three-momentum of the track, \mathbf{p}_i : $\mathbf{q}_i = F(\mathbf{V}, \mathbf{p}_i)$. The fitting procedure then minimizes the χ^2 defined in equation 7.1, by varying the vertex position and the three-momentum for each track:

$$\chi^2 = \sum_i \Delta \mathbf{q}_i^T \mathbf{W} \Delta \mathbf{q}_i, \quad (7.1)$$

where $\Delta \mathbf{q}_i = \mathbf{q}_i^{\text{measured}} - F(\mathbf{V}, \mathbf{p}_i)$ and \mathbf{W}^{-1} is the covariance matrix. This algorithm refits all the found tracks and therefore becomes rather slow if a lot of tracks are present. Under the assumption that the uncertainty on the transverse track parameters can be neglected close to the vertex, it is

possible to show that one can remove the need to refit the track parameters and thus greatly increase the speed of the algorithm [37].

7.3 Simulation of the ATLAS detector

A full simulation of the ATLAS detector is made with the GEANT4 program (GEometry ANd Tracking) [38, 39, 40]. The geometry of the detector is entered in the program, which contains the full physics information on how particles interact with matter. Each particle is transported through the detector in small steps. At each step GEANT checks if the particle decays, interacts with the detector material or just passes through. The detector response (e.g. voltage or time) is calculated from the deposited energy in the sensitive detector elements. At this stage, detector noise is added to all the sensitive elements to provide a better description of the expected detector response. The digitalization process³³ of the detector response is simulated. At this point the simulation is equivalent to the recorded data and the same reconstruction and analysis can be applied to both the data and simulation.

Thus, if both the event generators and the detector simulation were completely accurate, the simulated event would look exactly like the observed data. This is of course not the case, since it is already known that the event generators are only models, which are dependent on the tuning from data input. The detector simulation depends a lot on how well the material distribution is known and mistakes in this will produce a wrong simulation of the events. To estimate the effect of a wrong material distribution, simulations with an increased amount of material are made.

The simulation is used in almost every analysis with the ATLAS experiment. In general it is used to correct for the efficiency in the reconstruction of the particles from the collision. Sometimes the created particles will go through the detector, but not be detected. The size of this effect can be calculated by comparing the particles before and after the detector simulation. The simulation is also used to estimate systematic uncertainties on the results.

7.4 Data driven controls of the simulation of the inner detector

Since the simulation is used to correct the data, the precision of it is very important. Thus data driven test of the simulation is one of the major

³³The digitalization process is the transformation from analogue inputs registered in the detector to a digital number used further up in the analysis chain.

goals with the first available data from LHC. A method to test the amount of material within the detector is to look at the placement of secondary vertices not coming from particle decays, these vertices will instead be from charged tracks interacting with the material of the detector. In figure 7.7 the origins of the secondary vertices are plotted and the different detector parts are visible.

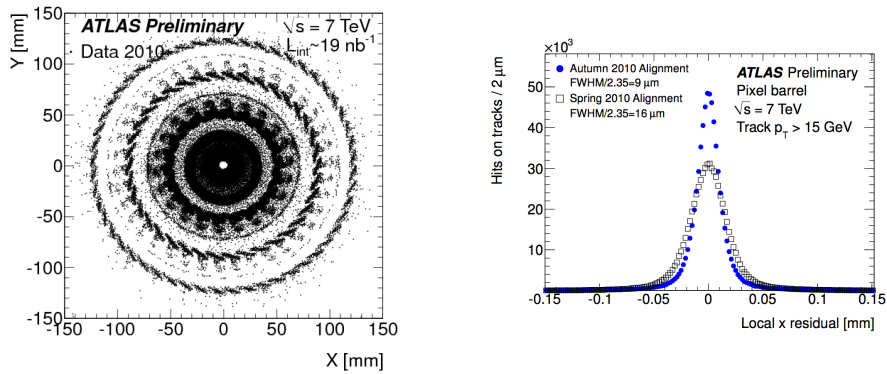


Figure 7.7: Data driven controls of the ATLAS detector: The x-y position of secondary vertices with a veto against K_0^- , λ_0^- and γ^- vertices [41] (left). The innermost circle is the beam pipe and the three next layers are from the pixel detector. The residuals for the pixel detector before and after alignment [42] (right).

The alignment of the detector can be determined by comparing the individual hits to the expected hits from the full track fit; such a plot is shown in figure 7.7. This is used to optimize the alignment of the detector and also determine the uncertainty due to misalignment [42].

8 The analysis

The aim of the analysis is to extract the K_S^0 and Λ particles from the ATLAS data. The obtained data will be presented like the distributions of charged particles shown in section 5. These distributions also have to be corrected back to event generator level to compare the data with the predictions from theory. The corrections need to account for all the efficiencies and smearing effects introduced by the detector.

The analysis chain is split into two different categories, depending on whether the final distribution includes p_T of the K_S^0/Λ or not. If only the number of K_S^0/Λ particles is needed, a fit is used to remove the background. This is not possible if the transverse momentum is needed in the final distributions (average p_T and sum p_T) and in this case the background has to be removed through simulations. Otherwise, the two analysis chains follow almost identical patterns. I will therefore describe the analysis chain for the angular multiplicity density distributions in detail and afterwards highlight any difference in the other analysis. During the description, the differences between K_S^0 and Λ particles (e.g. efficiencies and cuts) will be listed.

8.1 Overview of the analysis

First I will present a brief overview of the analysis chain before going into the detailed correction procedures. In figure 8.1 a sketch of the analysis can be seen. In appendix A a complete list of all the different cuts imposed is shown.

The trigger used to decide whether to store a collision or not, was the minimum bias trigger. The first part of the analysis is the event selection; this part has to pick out the ND events from the triggered sample of events, while removing the diffractive events. This is achieved by requiring the presence of a vertex and a certain amount of activity in the inner detector (i.e. a certain number of tracks). The leading jet is found, by first reconstructing all the tracks originating from the primary vertex. The tracks have to fulfill the requirement specified in the track selection in order to make sure that they are in fact tracks and not just combinatorial background. With all the tracks found, the jets are formed by clustering the tracks with the so-called “anti- k_t jet algorithm” and the leading jet is taken as the jet with the highest transverse momentum.

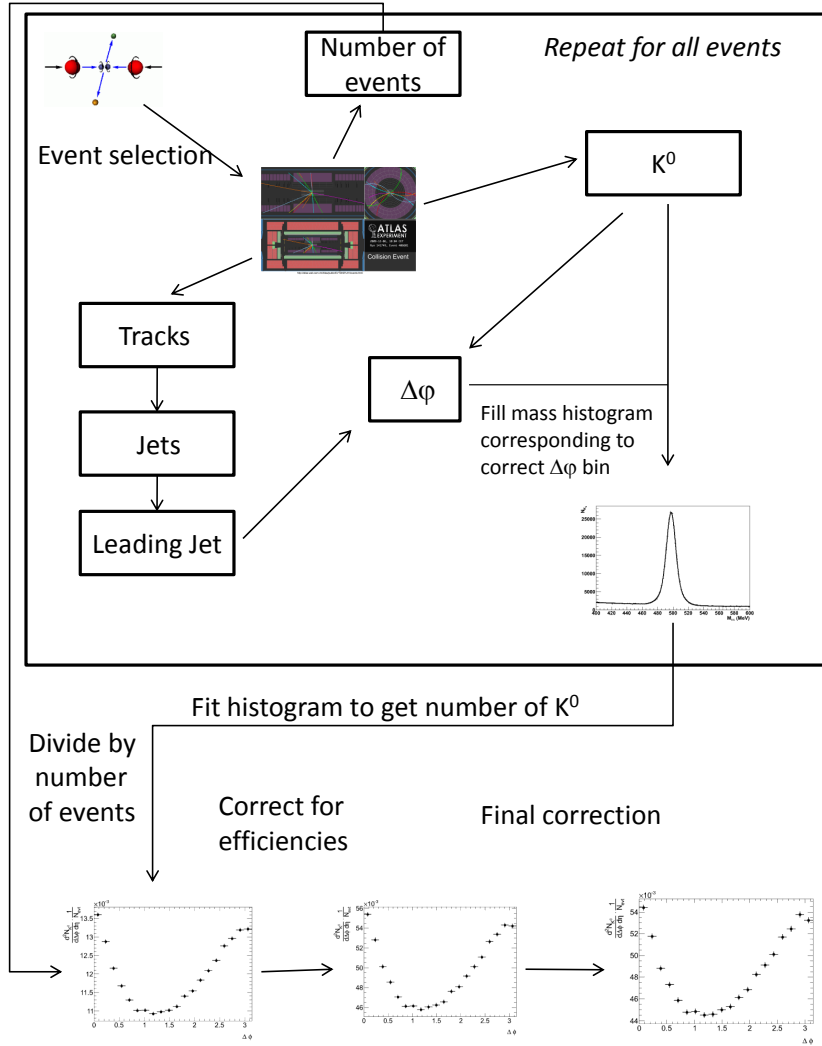


Figure 8.1: An overview of the analysis chain, starting from the collision of the two protons (top left) going all the way down to the final distribution (bottom right).

The K_S^0 mesons are found by their decay into two charged pions. These produce a secondary vertex, which can be observed in the detector. Secondary vertices can be created through other processes (combinatorial background, interactions with the detector and other particle decays). The background not originating from particle decays can be significantly reduced

by applying additional cuts on the vertex probability, transverse flight distance and cosines to the pointing angle (`CosThetaPointing`)³⁴.

For each bin in the final distribution a histogram of the invariant mass of the two pions is created. Calculating the azimuthal angle between the leading jet and the K_S^0 candidate tells which mass histogram to fill. This process is repeated for all the K_S^0 candidates within the chosen region of acceptance in all events.

The invariant mass histogram is fitted with a double Gaussian (signal) and a third order polynomial (background) and the area under the double Gaussian is the number of K_S^0 mesons. The number of K_S^0 mesons are divided by the number of events to get the wanted distribution. To correct back to event generator level, a correction is applied for the different efficiencies. For each bin in the final distribution, the average weight (due to reconstruction efficiency) of the K_S^0 candidates is calculated and applied as a correction. In the end, a final bin-by-bin correction is made to account for the fitting function and bin-to-bin migration.

The statistical errors are calculated by assuming Poisson distributed entries in the invariant mass histograms and are afterwards propagated through the fit and the different corrections. The different systematic errors are estimated through both data driven methods and MC simulation (see section 9) and is plotted along with the statistical errors in the final distribution.

8.2 Data selection

The data used for this study was taken with the ATLAS detector in March and April 2010. At this time, the LHC was running with a collision energy of 7 TeV. The data was recorded during seven runs and the different integrated luminosities can be seen in table 8.1. To decide whether to store an event or not, the MB trigger was used. After the trigger requirement, a total of 14338978 events were stored and used for this study corresponding to a total integrated luminosity of 0.22 nb^{-1} . The average number of collisions per bunch crossing was around 0.01, thus the probability to have additional collisions during the same bunch crossing was minimal (“pile-up” was minimal).

³⁴See section 8.6 for definition of the variables.

Run number	integrated luminosity [nb ⁻¹]	#Events selected
152166	0.0077	525098
152214	0.0041	279926
152221	0.022	1456644
152345	0.019	1214411
152409	0.083	5433321
152441	0.072	4641246
152508	0.012	788332
total	0.22	14338978

Table 8.1: The data runs used in this study. For each run the integrated luminosity for stable beams is shown, together with the number of events selected by the MB trigger.

8.3 Event selection

Since I want to study ND events, the event selection should reflect that by only selecting ND events. The event selection can be split into two: The standard MB selection and the additional cuts to get only ND events. To mimic the effect of the event selection on the data, several phase-space cuts are applied to the event generators.

8.3.1 Minimum bias event selection

The MB event selection is the same as used in the ATLAS UE article [25]. The aim of the event selection is to pick up all collisions with as low bias as possible, but still remove all the background originating from beam-halo events and cosmic rays. To accomplish these goals the events are required to satisfy the following requirements:

- The minimum bias trigger needs to have fired.
- A primary vertex reconstructed with at least two tracks fulfilling the follow conditions³⁵:
 - $|\eta| < 2.5$ and $p_T > 100$ MeV
 - $|d_0^{BS}| < 4$ mm
 - $\delta(d_0^{BS}) < 5$ mm and $\delta(z_0^{BS}) < 10$ mm
 - $n_{\text{pixel}} \geq 1$, $n_{\text{SCT}} \geq 4$ and $n_{\text{silicon}} \geq 6$

³⁵See track selection (section 8.4 for description of the variables used.

- A veto against events with multiple vertices to remove pile-up events: If more than two vertices with four tracks are present, the event is rejected.

The minimum bias trigger consists of two components: A forward detector to check for any energy deposits in the forward direction (MBTS) and a BPTX to check the beams are synchronized. The MBTS (Minimum Bias Trigger Scintillators) are scintillator counters placed in the forward direction ($2.12 < |\eta| < 3.85$). The counters are split in 8 different azimuthal regions and two η regions resulting in a total of 16 counters on each side of the detector. The trigger used is a single-arm trigger and only require a single of the total 32 counters to be above threshold. The BPTX (Beam Pickup Timing devices) are placed ± 175 m from the center of the ATLAS experiment. The BPTX measure the beam presence and coincidence between the two detectors is required such that the two beams collide within the center of the ATLAS detector.

In the case of no high momentum tracks the direction of the hard interaction is badly defined. Since the study of the underlying event relies heavily upon the difference in orientation between the leading track (hard interaction) and the rest of the particles, it is problematic to do the calculation if the hard interaction becomes too soft. Especially since the probability to misidentify the leading track becomes larger if no high momentum tracks are present. Therefore an extra cut is added; to have at least a single high momentum track.

- At least a track with $p_T > 1$ GeV.

8.3.2 Non diffractive event selection

To select only ND events, different additional cuts can be added to the event selection, the most common is to require at least 6 tracks in addition to the standard MB selection. The amount of diffractive events left in the simulated data after different cuts in the phase-space region can be seen in table 8.2. The large difference between the models shows the need to implement non model dependent cuts. The requirement of 6 tracks removes most of the diffractive events and if an additional track with at least 1 GeV in transverse momentum is required, the amount of diffractive events drop even lower. Thus the requirement of six tracks was chosen as an additional cut to the MB selection:

- Require at least 6 tracks with $p_T > 500$ MeV.

Phase-Space Region		$\sqrt{s} = 7 \text{ TeV}$		
min n_{ch}	min p_T MeV	PYTHIA6	PYTHIA8	PHOJET
2	100	21 %	21 %	14 %
1	500	17 %	21 %	14 %
6	500	0.4 %	10 %	8 %

Table 8.2: The fraction of diffractive events in the simulated data for different phase-space regions. All tracks are required to have $|\eta| < 2.5$. (The table is taken from the ATLAS MB article [43])

8.3.3 Phase-space cuts on the event generators

To make the event generators compatible with the data, the following phase-space cuts were imposed on the event generators.

- At least one track with $p_T > 1 \text{ GeV}$ and $|\eta| < 2.5$
- At least six tracks with $p_T > 500 \text{ MeV}$ and $|\eta| < 2.5$

8.4 Track selection

A track is the collection of hits in the detector describing the path of a particle. In figure 8.2 an event display shows the first collision in the ATLAS experiment. The dots are hits in the detector and the lines/curves are reconstructed tracks. As can be seen by the eye, the reconstruction algorithm misses a few tracks which is most likely due to the low transverse momentum of the tracks³⁶. The tracks can either come from the primary collision, from secondary collisions with the detector or from secondary vertices (particle decays). In addition to these tracks, there are backgrounds coming from wrongly combining hits to tracks and in rare cases also cosmic rays produces tracks. The tracks of interest in most MB studies are the tracks coming from the primary collision, but since this study revolves around finding K_S^0 and Λ particles from

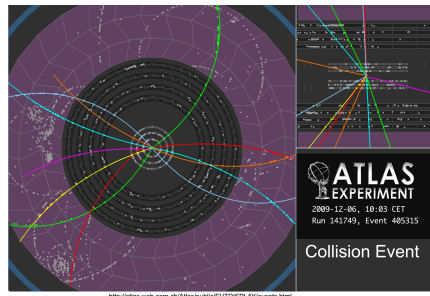


Figure 8.2: The first proton-proton collision observed by the inner part of the ATLAS detector at $\sqrt{s} = 900 \text{ GeV}$.

³⁶Low transverse momentum corresponds to very bended tracks.

their decay products, secondary tracks are also needed. Thus, in this study I will work with three types of tracks: Primary tracks, beamspot tracks and decay tracks³⁷.

The primary tracks are, as the name suggests, the tracks coming from the primary vertex. These tracks are used to find the leading jet (or just the leading track) which again is used to determine the ϕ direction of the hard interaction. The beamspot (BS) tracks are selected as close to the primary tracks as possible, but with no vertex constraint. Instead of using vertex information the distances are measured to the center of the beamspot, hence the name. These tracks are used in finding the primary vertex and the corresponding efficiency. The decay tracks are used to find secondary vertices from decaying particles and thus the selection is different from the other two track types. The different selection for the three types of tracks can be seen in table 8.3.

	Primary track	BS track	Decay track
$ d_0 < ? \text{ mm} (*)$	1.5	1.8	no
$ z_0 \sin(\theta) < 1.5 \text{ mm}$	yes	no	no
b-layer hit if expected	yes	yes	no
nPixel hits	1	1	no
nSCT hits	2, 4, 6(**)	2, 4, 6(**)	2
$p_T > 100 \text{ MeV}$	yes	yes	yes
$ \eta < 2.5$	yes	yes	yes
χ^2 probability > 0.01 if $p_T > 10 \text{ GeV}$	yes	yes	no
Veto against tracks used in secondary vertices	yes	no	no

Table 8.3: The different track selections for primary tracks, BS tracks and decay tracks. (*) The d_0 is measured to the primary vertex for primary tracks and to the BS for BS tracks. (**) 2,4 or 6 for respectively $p_T < 200 \text{ MeV}$, $200 \text{ MeV} < p_T < 300 \text{ MeV}$ and $300 \text{ MeV} < p_T$.

The requirement on the number of hits in the detector is used to remove combinatorial background. The η cut represents the coverage of the inner detector, particles with $|\eta|$ above 2.5 do not hit the inner detector and thus cannot be reconstructed. The efficiency to reconstruct the tracks

³⁷The selection of primary tracks and beamspot tracks follows the one used in the second ATLAS MB paper [43]

decreases rapidly in the very low p_T region, thus a cut on the minimum p_T is introduced.

The transverse impact parameter, d_0 , is the closest transverse distance between the track and either the primary vertex or the BS. z_0 is the closest longitudinal distance and θ is the angle between the track and the beam direction. These variables are used to distinguish between primary and secondary tracks. The d_0 distribution is dominated by primary tracks around zero (see figure 8.3) and only approximately one percent of the events come from secondary particles.

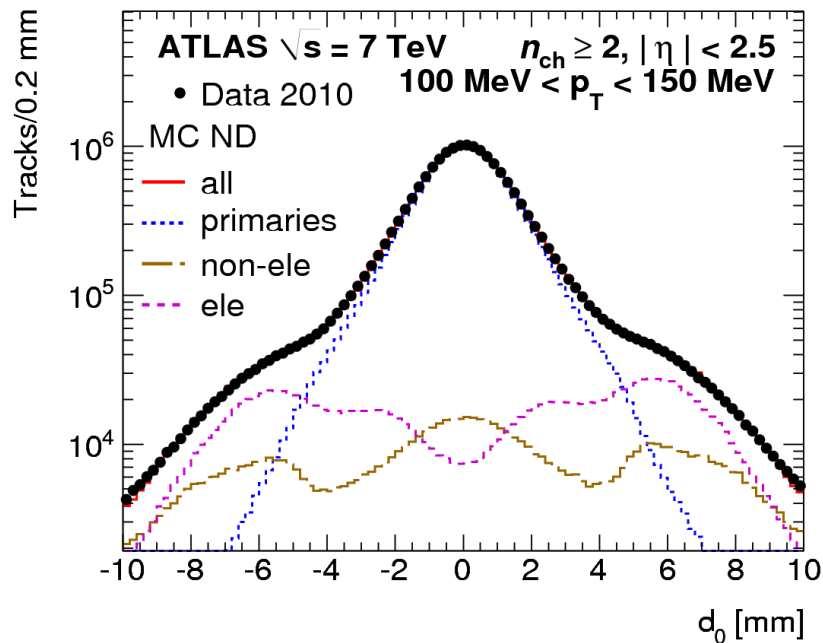


Figure 8.3: The transverse impact parameter distribution for MC simulation and data at $\sqrt{s} = 7$ TeV. The ND MC simulation agrees well the observed data. (Figure is taken from [43])

The requirements for tracks used for the ND event selection are the same as for the primary tracks except for the additional requirement of $p_T > 500$ MeV. The same goes for the single high momentum track required in the event selection, except of course the demand being $p_T > 1$ GeV.

8.4.1 Phase-space cuts on the event generators

To select similar tracks for the event generators, the following conditions were imposed on all tracks in the event generator:

- $p_T > 100 \text{ MeV}$
- $|\eta| < 2.5$
- charge $\neq 0$

8.5 From tracks to jets

The colored partons participating in the hard interaction will fragment into a strongly fluctuating number of hadrons. Therefore, the leading charged hadron might not always be a good representative of the scattered partons and this will sometimes lead to a wrong definition of the transverse region. In section 3.4 it was noted that the created particles will tend to fly collinear with the particle from the hard interaction. Thus creating a single entity, called a jet, of the particles, flying close to each other, provides a better representation of the hard interaction.

As was noted in section 3.4, several cut-off scales had to be introduced to simulate the effect of the radiated gluons. It is possible to reduce the dependency on the cut-off scales by using jets instead of single particle tracks. Imagine a particle emitting an almost collinear particle just above the cut-off limit. By increasing the cut-off a little bit, the otherwise two particles now becomes one single particle. This illustrates that the number of tracks depends upon these cut-off values, whereas the jet will look the same, no matter whether it stays as one particle or becomes two particles. If the jet algorithm fulfils this property it is known as collinear safe. A similar problem arises at the other divergency for the radiation of gluons (equation 3.4) corresponding to the radiation of low momentum gluons. Jet algorithms that preserves the same jets, even in the case of soft radiation are known as infrared safe, which combined with collinear safe are called IRC safe jet algorithms.

The jet algorithm used in this analysis is the anti- k_t algorithm [44]. The starting point is to calculate the distance between all the reconstructed tracks³⁸, d_{ij} , and the distance between the tracks and the beam, d_i . The

³⁸It is also possible to use the algorithm on for instance clusters in the calorimeter.

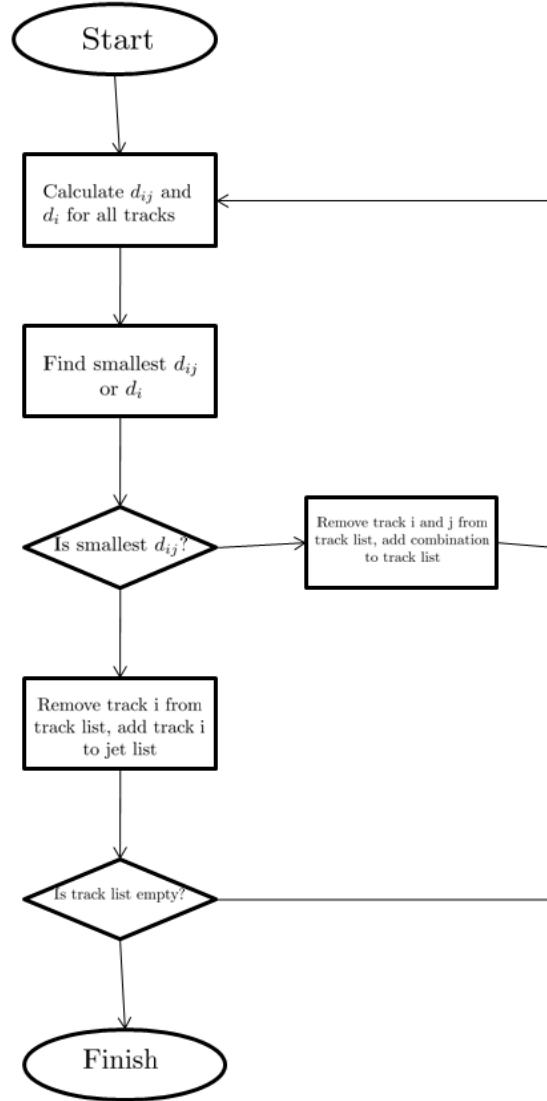


Figure 8.4: A flowchart of the jet algorithm. The starting point is a list of all tracks in the event and at the end a list of all the jets is produced.

definition of the distances is given in equation 8.1,

$$d_{ij} = \min \left(\frac{1}{p_{Ti}^2}, \frac{1}{p_{Tj}^2} \right) \frac{\Delta_{ij}^2}{R^2} \quad (8.1)$$

$$d_i = \frac{1}{P_{Ti}^2}$$

where $\Delta_{ij}^2 = (y_i - y_j)^2 + (\phi_i + \phi_j)^2$ ³⁹ and R is a radius parameter determining the size of the jet. The reason for using rapidity (y) instead of the angle is that the hard system might be boosted, and thus the angle difference would depend upon the reference frame, where the rapidity difference stays the same. One selects the smallest of the distances and if it is a pair of tracks (i.e. d_{ij}), the two tracks are combined into a single “pseudo-track” and added to the list of tracks and the two original tracks are removed from the list. If the smallest distance is a single track (d_i), the track is removed from the list of tracks and added to the list of jets. This process continues until all the tracks are removed and only jets are remaining (see figure 8.4).

The properties of the anti- k_t jet algorithm can be understood by considering jets close to each other. In the case of a hard and soft jet ($p_{T1} \gg p_{T2}$) the first jet will take almost all the nearby soft particles. Whereas if the two jets have about the same momentum ($p_{T1} \sim p_{T2}$), the jets will share the soft particles. This property can be seen in figure 8.5 together with a comparison of different jet algorithms. The anti- k_t algorithm also makes regular shaped jets, which gives a very nice graphical interpretation of the area of the jet. In the case of only a single jet in an area, the shape of the jet will be a circle.

8.6 Measuring the number of K_S^0 and Λ particles

The K_S^0 particles⁴⁰ are identified through their decay into two charged pions. Thus the start of the search is a secondary vertex with two different charged tracks pointing towards it (see figure 8.6). In addition to decaying particles, secondary vertices can also arise if a single particle interacts with the material in the detector and change direction by emitting a new particle. Another background is a simple combinatorial background; two tracks pointing towards the same spatial point, even though none of them originated from the point.

To distinguish between the secondary vertices from K_S^0 decays and the background, several cuts on the secondary vertices are implemented. These cuts mainly serve the purpose of removing the background not coming from particle decays.

³⁹In the definition rapidity is used, but this is not possible in the experiment and instead one uses pseudorapidity.

⁴⁰In this section the method will be described for K_S^0 particles, the method is very similar in the case of Λ particles and any difference will be highlighted.

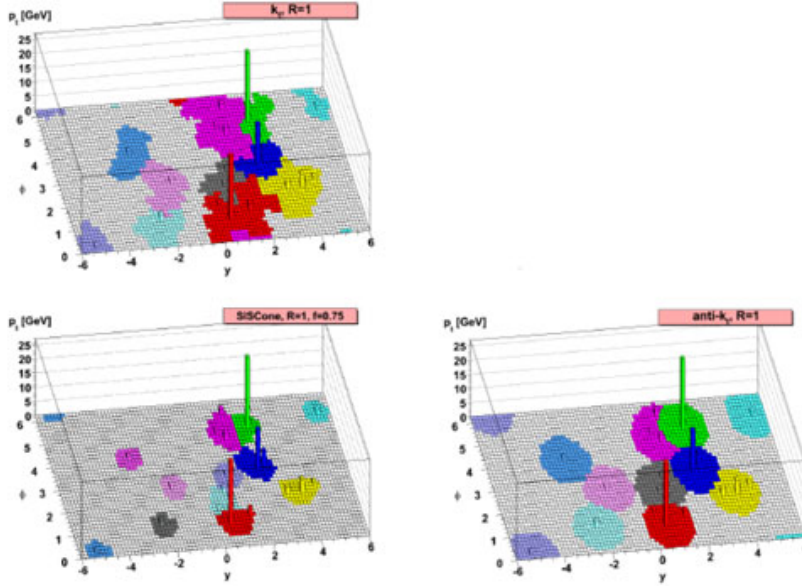


Figure 8.5: The shape of the same event reconstructed by different jet algorithms. Each colored area represents a jet and also which soft particles would be added to which jet.

To find the number of K_S^0 particles, one assumes the two tracks are pions and calculates the invariant mass. If the secondary vertex comes from a K_S^0 decay, the invariant mass will be equal to the mass of a K_S^0 meson. Detector effects will smear this to a wider peak and by fitting and then calculating the area under the peak, the number of K_S^0 particles can be found.

8.6.1 Selection of secondary vertices

The selection of secondary vertices is based upon different cuts on the transverse flight length, χ^2 , CosThetaPointing . There are several considerations to take into account before deciding where to cut. The final results should be independent of the cuts chosen, since they reflect detector effects⁴¹. The aim of the cuts is to minimize the uncertainty, but the uncertainty comes in two variations: statistical uncertainty and systematic uncertainty. If no extra measures to remove the background was taken, the statistical uncertainty could be minimized by maximizing the

⁴¹The cut on transverse flight distance is also imposed on the event generators, and thus the result will of course depend upon the cut on this variable.

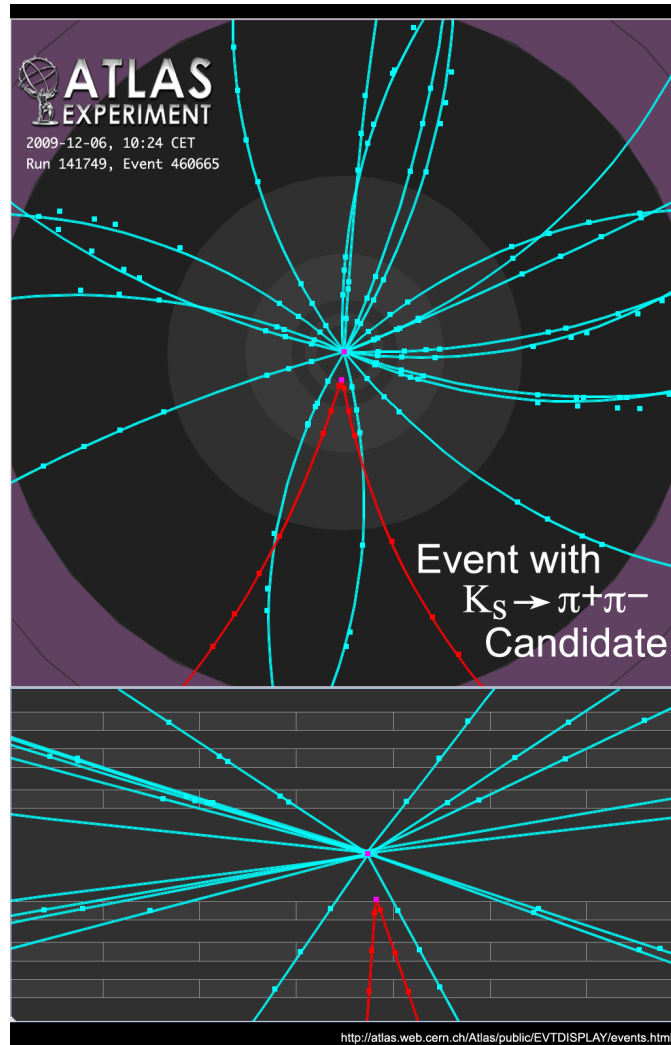


Figure 8.6: A candidate for a K_S^0 decaying into two charged pions observed with the ATLAS detector. The two charged tracks bend in opposite direction indicating opposite charges and their vertex is clearly separated from the primary vertex.

significance $\frac{s}{\sqrt{b}}$, s being the number of signal events and b the number of background events. But since additional cuts (there might be correlated) and afterwards a fitting method are implemented to further remove background, the significance might not be the best estimate to minimize the statistical uncertainty. Instead one should propagate the effect of the cut to the final statistical uncertainty and then minimize this by varying the cut parameters.

But also the systematic uncertainties have to be considered, these are much

harder to calculate and no single estimate on how to minimize can be given. In addition it is preferable if the cuts are similar to other analysis of the same phenomenon making the results more easily comparable. If too different cuts are implemented in an otherwise equal analysis, MC simulation is needed to make them comparable, which may introduce an additional systematic uncertainty.

The three different considerations do not always agree on the same value and a compromise has to be made. This analysis follows the general set of cuts used in other analysis of K_S^0 and Λ hadrons with the ATLAS detector. The final cuts can be seen in table 8.4. In addition, the two tracks both have to fulfill the requirements for decay tracks listed in table 8.3.

	K_S^0	Λ
d_{xy} [mm]	> 4	> 17
χ^2	< 15	< 15
CosThetaPointing	< 0.999	< 0.9998
mass veto	yes	yes
p_T [MeV]	< 100	< 500
$ \eta < 2.5$	yes	yes
decay tracks	$p_T < 100$ MeV $ \eta < 2.5$ $N_{\text{SCT}} \geq 2$	$p_T < 100$ MeV $ \eta < 2.5$ $N_{\text{SCT}} \geq 2$

Table 8.4: The different cuts imposed to select secondary vertices originating from primary particle decays. The three first cuts remove the contamination coming from non-primary particle decays and the mass region veto is to separate the decays from primary particles. The three first cuts are described in the following sections, whereas the mass veto cut is described in the fitting section 8.6.5. The acceptance cut on p_T and η is due to the very low efficiency outside this region.

8.6.2 Transverse flight distance

If the secondary vertex is close to the primary vertex, it is more likely that the two vertices are in fact one common vertex and two tracks pointing at a slightly different direction are due to miss measurement in the detector. This background is reduced by applying a cut on the transverse flight distance, d_{xy} , such that the two vertices have to be separated. The background

distribution has its maximum at $d_{xy} = 0$ (see figure 8.7) and the later peaks are due to the material of the detector. The peak at 30 mm is due to the beam-pipe and the first and second layer of the pixel detector produces respectively the second peak at 50 mm and the smaller peak at 90 mm.

The distribution for K_S^0 has a peak around ~ 9 mm and afterwards falls off exponentially. The exponential drop is expected from theory, since it is a decay process. The rise at the beginning is due to the efficiency of the detector. The probability to detect particles decreases rapidly as d_{xy} goes to zero. The different efficiencies are discussed in details in section 8.7.3, but the efficiencies are not parameterized as a function of d_{xy} . Rather, it is parameterized as a function of p_T and these two quantities are related by the time dilation of the special relativity. In the reference frame of the detector, the high momentum particles will have a longer lifetime and thus move further in the detector before decaying. This means that low transverse momentum K_S^0/Λ particles most likely correspond to low transverse flight distance.

For K_S^0/Λ a peak is also observed at the beam pipe, but at the pixel layers a combination of a decrease and a peak is observed (the decrease is most obvious at the pixel layer at ~ 90 mm, for the layer at ~ 50 mm it looks more like a combination of a peak and a decrease). This decrease is the K_S^0 mesons undergoing nuclear interactions with the detector resulting in either a momentum transfer or sometimes a complete absorption or photon conversion. The peak at the beam-pipe is probably again due to nuclear interactions, but this time the end result is two charged particles coming from the interaction. Both the enhancement (Nuclear interaction resulting in two charged tracks) and the suppression (absorption) is probably present at both the beam-pipe and the pixel layers and the difference can be explained mainly by the different amount of material. The beam-pipe is thinner than the pixel layers hence less K_S^0 mesons are absorbed and the created charged particles have a higher probability leaving the detector without scattering.

One way to test the origin of the particles created in the beam-pipe is to impose a cut on `CosThetaPointing`⁴². If the particles come from a nuclear interaction the reconstructed K_S^0 mesons will in general not point towards the primary vertex. The distributions with the implemented cuts are shown

⁴²See section 8.6.4 for a description of the pointing angle

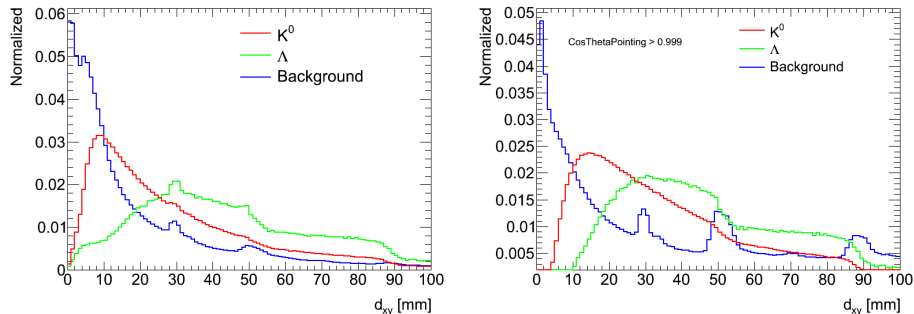


Figure 8.7: MC simulation of the distribution for the transverse flight length of secondary vertices separated according to the origin of the secondary vertex (left) and the same distribution but with an additional cut on $\text{CosThetaPointing} > 0.999$ to remove decay from non-primary particles (right). The plotted secondary vertices are after full reconstruction and the identification as either K_S^0, Λ and background is done through a hit based matching. The area under the curves are normalized to one.

in figure 8.7 and the peak at the beam-pipe has disappeared for the K_S^0 particles.

The Λ distribution shows the overall same behavior as the K_S^0 distribution. It is shifted to the right due to a combination of a longer lifetime and a different reconstruction efficiency. The longer lifetime also produces the more flat shape observed for the Λ particles.

8.6.3 Secondary vertex probability

The cut on χ^2 is imposed in the reconstruction phase and no tightening is afterwards implemented. The χ^2 variable only helps discriminating between real secondary vertices and wrong combinatorials leading to secondary vertices. The χ^2 distributions for K_S^0, Λ and the background follow the same overall shape, except for the background having a flatter slope. This leads to the background having relatively twice as many events at $\chi^2 = 15$ (see figure 8.8)⁴³

⁴³Since all the curves are normalized, it is the relative number of events used and the ratio refers $\frac{\left(\frac{N_{bin}}{N_{total}}\right)_{bkg}}{\left(\frac{N_{bin}}{N_{total}}\right)_{K_S^0}}$.

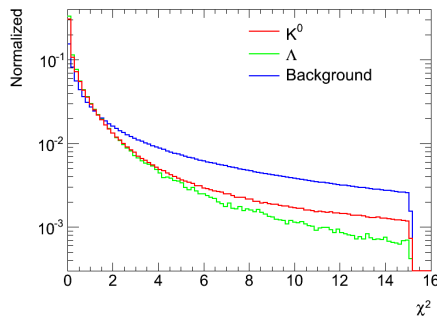


Figure 8.8: MC simulation of the χ^2 distributions for secondary vertices separated according to the origin of the secondary vertex. The plotted secondary vertices are after full reconstruction and the identification as either K_S^0 , Λ and background is done through a matching to the generated particles. The areas under the curves are normalized to one.

8.6.4 CosThetaPointing

Another relevant parameter is the pointing angle. The pointing angle is defined as the angle between the momentum vector of the K_S^0 and the spatial vector from the primary vertex to the K_S^0 (see figure 8.9). The pointing angle should be very small in the case of primary particle decaying, since its momentum vector should point back towards the primary vertex. Whereas decays from secondary particles and miss combined tracks in general not will point towards the primary vertex. Instead of using the pointing angle directly, one uses cosines to the pointing angle instead (this variable will be labeled CosThetaPointing in the plots).

The CosThetaPointing distribution for both the K_S^0 and the Λ baryons have a very distinct peak at one (see figure 8.10). The background shares the same peak, but the fraction of secondary vertices in the peak is lower compared to the other part of the distribution. Away from the peak the relative background to signal ratio is approximately 10 and 25 for K_S^0 mesons and Λ baryons respectively. The amount of signal particles in the peak is also much larger compared to the number of signal particles outside the peak, thus almost no signal is lost by requiring a high value of CosThetaPointing and almost all the background not from primary particle decays is removed.

In the above figures only the normalized distributions were considered, which

8.6 Measuring the number of K_S^0 and Λ particles

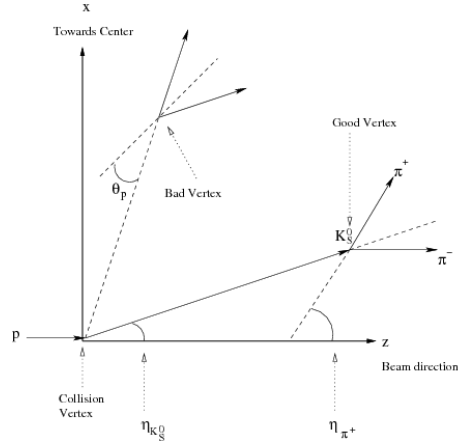


Figure 8.9: A drawing showing the pointing angle for both a secondary vertex coming from a particle decay and a secondary vertex from something else. The pointing angle is only shown for the bad vertex, since it would be impossible to see for the good vertex.

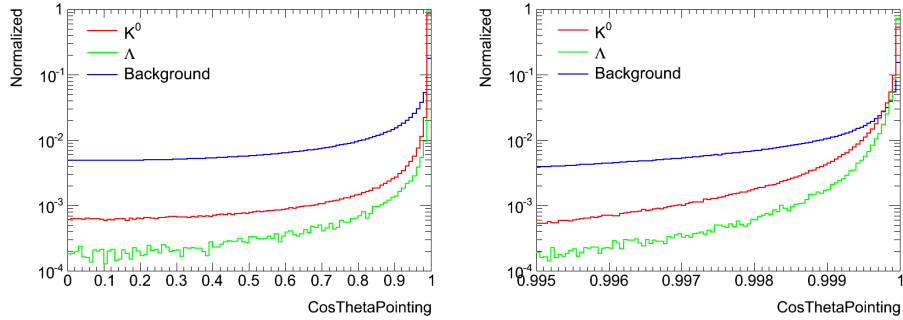


Figure 8.10: MC simulation of the CosThetaPointing distribution for secondary vertices separated according to the origin of the secondary vertex (left). The right figure shows the same distribution zoomed in around the cut values. The plotted secondary vertices are after full reconstruction and the identification as either K_S^0, Λ and background is done through a hit based matching. The areas under the curves are normalized to one.

do not reflect the overall difference in the number of background and signal particles. After only the reconstruction and before any additional cuts are implemented the overall K_S^0 to background ratio is 0.013 and the Λ to background ratio is $8.6 \cdot 10^{-4}$. After implying the additional cuts the two ratios have improved to respectively 14 and 3.5. The effects of the individual cuts are shown in table 8.5.

8.6 Measuring the number of K_S^0 and Λ particles

	N_{bkg}	N_{K^0}	N_{Λ}	$\frac{N_{K^0}}{N_{\text{bkg}}}$	$\frac{N_{\Lambda}}{N_{\text{bkg}}}$
No cuts	$6.35 \cdot 10^8$	$8.45 \cdot 10^6$	$5.44 \cdot 10^5$	0.013	$8.6 \cdot 10^{-4}$
d_{xy} cut (*)	$(4.94/2.57) \cdot 10^8$	$8.28 \cdot 10^6$	$5.20 \cdot 10^5$	0.017	$2.0 \cdot 10^{-3}$
CosThetaCut (*)	$(1.92/0.966) \cdot 10^7$	$5.26 \cdot 10^6$	$4.18 \cdot 10^5$	0.27	0.043
χ^2 cut	$6.34 \cdot 10^8$	$8.44 \cdot 10^6$	$5.44 \cdot 10^5$	0.013	$8.6 \cdot 10^{-4}$
mass veto (*)	$(6.17/6.16) \cdot 10^8$	$8.29 \cdot 10^6$	$4.84 \cdot 10^5$	0.013	$7.9 \cdot 10^{-4}$
Full cuts (*) (**)	$(2.85/0.837) \cdot 10^5$	$4.25 \cdot 10^6$	$2.95 \cdot 10^5$	14	3.5

Table 8.5: The number of different secondary vertices in twenty million simulated events. (*) Different cuts are applied in the K_S^0 and Λ selections and the first number in the background refers to the K_S^0 selection and the second to the Λ selection. (**) For the full cuts, the K_S^0 / Λ candidates are required to have an invariant mass within a broad region around the expected mass.

8.6.5 Fitting the mass histogram

All the three cuts above remove background not originating from primary particle decays, thus almost all the secondary vertices left are decays. But since several different decays are possible, a method is needed to separate these. This separation is achieved by the difference in mass between the particles, thus by calculating the invariant mass of the two decay products and looking for a peak around the particles mass, it is possible to count the number of a single type of particles. Since the calculation of the invariant mass requires the knowledge of particle identification and the inner tracker does not provide this particle identification, different hypothesises are tested.

In the case of a K_S^0 decay, both the tracks are assumed to be pions and the invariant mass is calculated. For the Λ particles the assumption is that the positive charged track is a proton and the negative charged track is a pion. Under the assumption of a two pions decay, a Λ decay will produce the distribution seen in figure 8.11 and can thus be mistaken as a K_S^0 . This background can be removed by setting a veto against particles that have the mass of the Λ particle under the assumption of a decay into a proton and a pion⁴⁴: All secondary vertices with $|M_{p\pi} - M_{\Lambda}| < 5.8 \text{ MeV}$ ⁴⁵ are rejected. For the Λ particles a similar cut is imposed, namely: $|M_{\pi^+\pi^-} - M_{K_S^0}| <$

⁴⁴The $\bar{\Lambda}$ particles are removed as well by assuming the negative charged track to be the proton and the positive to be the pion.

⁴⁵5.8 GeV corresponds to $2.5\sigma_1$, where σ_1 is the smallest of the two calculated σ s in the Λ mass fit.

14.4 MeV⁴⁶.

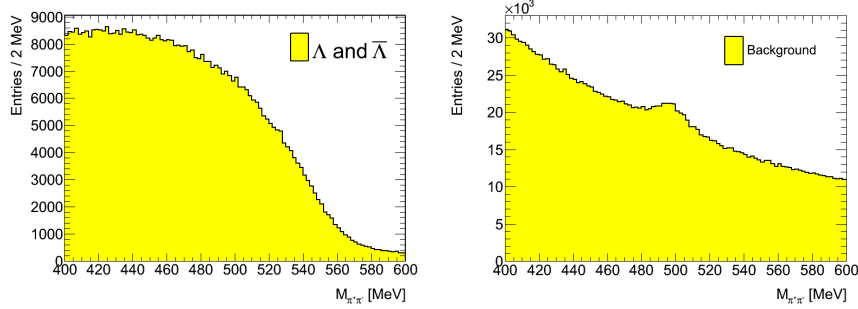


Figure 8.11: The invariant mass distribution assuming a decay into two pions for respectively the Λ particles (left) and background (right). The background is found by taking all secondary vertices not matched to either a K_S^0 or a Λ particle. The peak observed just around the K_S^0 mass in the background distribution is due to K_S^0 particles not being matched correctly and thus being placed in the background category.

The reason for specifically rejecting the Λ particles and not just including them in background fit is their distribution under the double pion assumption. The distribution starts to decrease just around the K_S^0 mass, but before and after the K_S^0 mass region it is relatively flat (see figure 8.11). Describing this effect in a fit underneath the huge peak from the K_S^0 particles is problematic and it is a better solution to simply just remove the Λ particles. The veto cut will also remove some of the real K_S^0 particles, but this effect is handled in the efficiency corrections.

In figure 8.12 the invariant mass distribution around the K_S^0 and Λ mass are shown. The distributions are fitted to a double Gaussian (signal) plus a third order polynomial (background). The number of K_S^0 and Λ particles can thus be calculated as the integral of the double Gauss function. The mean of the Gaussian functions are forced to the same value and otherwise all parameters are free.

The fit procedure goes through several steps to ensure that the fit converges in the expected way:

- First an initial guess on the parameters according to known values or

⁴⁶Which again corresponds to $2.5\sigma_1$, but calculated from the K_S^0 mass distribution.

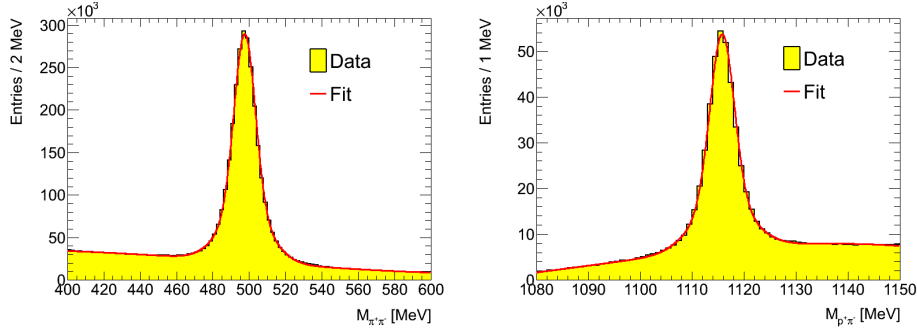


Figure 8.12: The mass histograms for K_S^0 (left) and Λ (right) for all secondary vertices passing the K_S^0 and Λ selections, respectively.

simple calculations is carried out. This includes setting the overall amount of events to the integral of the histogram. The mean of the two Gaussians is set to be the known mass (of either the K_S^0 or Λ). The standard deviations of the Gaussian functions are estimated by comparing the height of the Gaussian to the area below it. The zero and first order terms of the background polynomial are found by looking at the bins longest away from the Gaussian peak. The second and third order terms are set to predetermined values.

- Secondly the background distribution is fitted in the side bands to give a better estimate of the parameters.
- Then the overall fit is made with all the parameters free.
- After the fit several tests are made to check whether the fit converged in the wanted form or not. The most common way for the fit to converge in a wrong way is that one of the Gaussians is used to describe the background instead of the signal. This might produce an overall correct fit, but the afterwards calculated number of K_S^0 particles would be wrong (see figure 8.13). To check for this the following conditions had to be fulfilled:

$$- \left| \frac{\sigma_1}{\sigma_2} \right| < 7 \text{ and } \left| \frac{\sigma_2}{\sigma_1} \right| < 7. \text{ If one of the Gaussian distributions is used to describe the background instead of the signal it will have a very high } \sigma \text{ due to the relative flat background. This cut will prevent this from happening. In addition it will prevent one of the Gaussian from having a very low } \sigma \text{ used only to describe the center point in the distribution.}$$

- The fraction between the two Gaussians has to be between zero and one. This also helps to prevent the use of the Gaussian distributions in describing the background.
- The relative uncertainty on the number of particles cannot be too high ($\frac{\delta_{N_{K_S^0}}}{N_{K_S^0}} < 0.2$ if $N_{K_S^0} > 50$ and otherwise $\frac{\delta_{N_{K_S^0}}}{N_{K_S^0}} < 1$). If the relative uncertainty is high, it indicates that one of the Gaussians has a low σ and are only used to describe the center bin.
- The background function is not allowed to have a low minimum at the mean of the Gaussians ($\frac{bkg_{centerbin}}{bkg_{firstbin}} < 2$ and $\frac{bkg_{centerbin}}{bkg_{lastbin}} < 2$). This also helps to prevent the signal Gaussians to describe the background instead of the expected background function.
- If the fit did not pass the checks it is repaired by fixing the background function to the initial function fitted in the side band regions. With the background function fixed, a new fit of the double Gaussian is made. This made all the fits converge according to the above criteria.

The checks on the fit are mainly needed in the mass histograms with low statistics. Thus one has to be really careful about splitting the data into too many bins and imposing too many cuts reducing the amount of data significantly.

All the fits described above are log likelihood fits and the error on the bins is assumed to be Poisson distributed. The total number of K_S^0 is given by the area under the two Gaussian distribution and the statistical uncertainty is taken from the fit.

8.6.6 Phase-space cuts on the event generators

To reflect the selection of K_S^0 and Λ hadrons in the data, several phase-space cuts are introduced in the event generator (see table 8.6). By staying as close to the data selection as possible, the event generators are not used to extrapolate the data to areas, which are not probed by the data. Thus the model dependency is reduced, which allows for a better comparison between the data and different event generators. One problem with the very detector (and selection) specific cuts is the comparison between different experiments. For instance the ATLAS experiment often use $|\eta| < 2.5$ for tracks, whereas CMS only uses $|\eta| < 2$. To correct for such differences, one often has to rely on the event generators and thus reintroducing the model dependency.

8.6 Measuring the number of K_S^0 and Λ particles

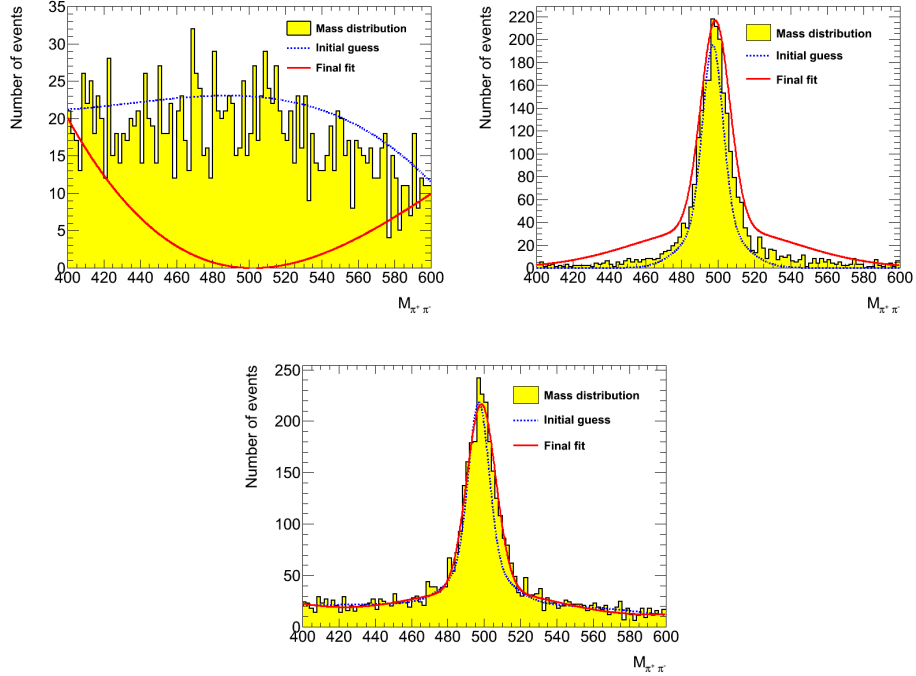


Figure 8.13: An example of a fit of the MC simulation, where the fit does not converge as expected. The mass distribution is split into background (top left) and signal (top right) by the use of the ΔR -matching (see section 8.7.2 for definition of ΔR -matching). In the bottom the mass histogram with both background and signal is shown. The overall fit seems to describe the data fairly well, but separating into the background and signal clearly shows how the background function does not describe the background and similar for the signal function.

	K_S^0	Λ
$p_T > [\text{MeV}]$	100	500
$ \eta < 2.5$	yes	yes
$d_{xy} > [\text{mm}]$	4	17
Decay tracks:	$p_T > 100 \text{ MeV}$ $ \eta < 2.5$ charge $\neq 0$	$p_T > 100 \text{ MeV}$ $ \eta < 2.5$ charge $\neq 0$

Table 8.6: The phase-space cuts imposed on the event generators selection of K_S^0 and Λ hadrons

8.7 Efficiencies and corrections procedures

Several different corrections are applied to the data to account for the detector effects. One could of course make a single correction comparing the final reconstructed distribution with the generated distribution. But this method would impose a high model dependency and it would not be possible to explain the physical origin of the full correction factor, which would make the correction lose credibility. Instead the corrections are split into several categories depending upon which part of the analysis procedure they affect. In addition some of the corrections are split even further to better give a physical explanation of the origin of the correction. It would be preferable to use data driven methods to estimate the different corrections, in order to minimize the use of the MC simulation. But the timeline has not allowed for this, and instead a data driven control of the overall correction procedure was made.

8.7.1 Event wide corrections

The event wide corrections come from the trigger efficiency, vertex efficiency, ND efficiency and UE efficiency⁴⁷. The trigger efficiency, vertex efficiency and ND efficiency are parameterized by the number of BS tracks in the event. The BS tracks are used because they do not depend upon the vertex and thus can be found even with no vertex present.

The trigger efficiency was studied in the ATLAS MB paper [45] and for events with more than 4 BS tracks the efficiency is above 99.5%. Since this study requires at least 6 tracks, the correction due to the trigger is negligible and is thus ignored for this study.

Both the vertex efficiency and the ND efficiency are estimated from simulation of non-diffractive pp collisions using the ATLAS MC09 tune of PYTHIA. The vertex efficiency is parameterized as a function of the number of BS tracks and is found by dividing the number of events passing the vertex cut with the number of simulated events:

$$\epsilon_{\text{vtx}}(N_{\text{BS}}) = \frac{N_{\text{evts}}^{\text{rec}}(N_{\text{BS}})}{N_{\text{evts}}^{\text{gen}}(N_{\text{BS}})} \quad (8.2)$$

The same method is used to estimate the ND efficiency and the two efficiencies are shown in figure 8.14. The vertex efficiency quickly goes to

⁴⁷The “ND efficiency” refers to the requirement of at least six tracks with $p_T > 500$ MeV and the “UE efficiency” refers to the requirement of a single track with $p_T > 1$ GeV

one (at $N_{BS} \approx 4$), whereas the ND efficiency has a much slower rise (it first becomes one at $N_{BS} \approx 25$). This is due to the vertex cut only requires two tracks while the ND efficiency cut requires six tracks.

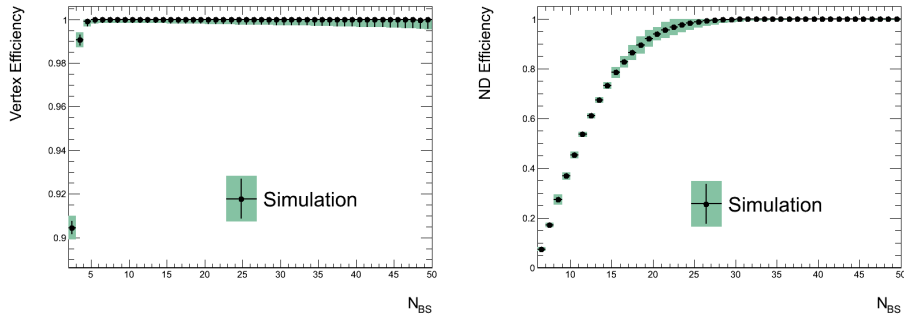


Figure 8.14: The vertex efficiency (left) and the ND efficiency (right) as a function of the number of BS tracks. The vertical lines show the statistical uncertainty. Both the efficiencies were derived from simulations.

To account for the requirement of a single track with $p_T > 1$ GeV, the probability is calculated for the situation that all tracks with $p_T > 1$ GeV are not reconstructed (see equation 8.3, where the product runs over all reconstructed tracks with $p_T > 1$ GeV). The efficiency (ϵ_{UE}) is then given as one minus the probability. This method slightly overestimates the correction needed, since it only uses the reconstructed tracks and not the true number of tracks. For instance, if four tracks are created in the interaction, but only three are reconstructed. This method calculated the probability that the three tracks are not found, whereas it should calculate the probability that four tracks were not found. This effect is corrected for in the final bin-by-bin correction.

$$\epsilon_{UE} = 1 - P(\text{Miss all } p_T > 1 \text{ GeV tracks}) = 1 - \prod_i (1 - \epsilon_{trk}^i(p_T, \eta)) \quad (8.3)$$

The total correction is the product of the three corrections and can be seen in equation 8.4. This correction is applied both to the total number of events as well as the individual K_S^0 and Λ particles found in the event. Hence one could state that this correction is applied both to the nominator and denominator in the final distributions. But the correction still needs to be implemented to correct for a bias if the production of K_S^0 or Λ particles

depends upon the event wide efficiency.

$$w_{\text{evt}}(N_{\text{BS}}) = \frac{1}{\epsilon_{\text{vtx}}(N_{\text{BS}})} \cdot \frac{1}{\epsilon_{\text{ND}}(N_{\text{BS}})} \cdot \frac{1}{\epsilon_{\text{UE}}} \quad (8.4)$$

8.7.2 Track corrections

The track correction consists of both the track efficiency and the correction for fake and secondary tracks.

The track efficiency is found from simulation by comparing the reconstructed to the generated particles and is parameterized by p_T and η . The reconstructed tracks are matched to generated tracks by requiring the two tracks to be within the same region of phase-space ($\Delta R < 0.15^{48}$) and also share at least one pixel hit. Dividing the number of matched tracks with the total number of generated tracks provides the tracking efficiency (see equation 8.5).

$$\epsilon_{\text{trk}}(p_T, \eta) = \frac{N_{\text{rec}}^{\text{matched}}(p_T, \eta)}{N_{\text{gen}}(p_T, \eta)} \quad (8.5)$$

where p_T and η is from the generated particle. The reconstruction efficiency as a function of respectively p_T and η are shown in figure 8.15 (integrated over the η variable in the p_T plot and vice versa for the η plot). The low p_T tracks have a relative low efficiency, but as the transverse momentum increases to ~ 1 GeV the efficiency becomes almost flat at around 80%. The efficiency in the central part of the detector is almost flat and first at around $\eta \approx 1$ does the efficiency start to drop.

The amount of fake tracks is estimated by the MC simulation as the number of reconstructed tracks not matched to any of the generated tracks. It is parameterized as a function of both p_T and η . The biggest amount of fake tracks comes from reconstructed tracks just on the border of the kinematical range (e.g. tracks with $\eta \sim 2.5$). These tracks might be reconstructed to pass the kinematic cuts, whereas the generated particles might not pass these cuts. This effect is clearly visible in the distribution of fake tracks (see figure 8.16), where the fake rate increases by a factor of ~ 10 just around the η cut. Except for just around the kinematical cuts the fake rate is less than 1‰ and just around the cuts it increases to around 7‰.

The fraction of secondary tracks is estimated by the MC simulation and

⁴⁸ $\Delta R = \sqrt{(\Delta\phi)^2 + (\Delta\eta)^2}$ and I will refer to this type of matching as ΔR matching or cone-matching.

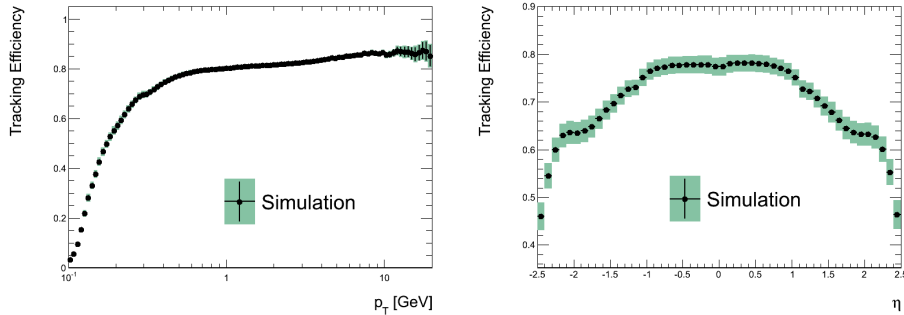


Figure 8.15: The track efficiency as a function of respectively p_T (left) and η (right). The statistical uncertainty is shown as vertical lines and the shaded areas represent the sum of the statistical and systematic uncertainties added in quadrature. The efficiencies were derived through the use of simulations (equation 8.5).

is parameterized as a function of p_T . The fraction of secondary tracks varies between 2 – 10 ‰ depending upon p_T (see figure 8.16).

A weight, $w_{\text{trk}}(p_T, \eta)$, is assigned to each track and it is calculated as a product of the individual corrections (see equation 8.6). The weight is used to correct any final distributions where tracks are used (e.g. the number of tracks or the sum of track momenta). The weight is not used in the calculation of the leading jet since it is an average correction and is not suitable to be used on an event-to-event basis. Instead the correction for the leading jet is handled in the final bin-to-bin migration correction.

$$w_{\text{trk}}(p_T, \eta) = \frac{1}{\epsilon_{\text{trk}}(p_T, \eta)} \cdot (1 - f_{\text{sec}}(p_T)) \cdot (1 - f_{\text{fake}}(p_T, \eta)) \quad (8.6)$$

8.7.3 Correction for K_S^0 and Λ efficiencies

The K_S^0 and Λ efficiencies are derived from simulations similar to the case of the tracks. The matching also uses the ΔR -matching, but no common hit in the pixel detector is required⁴⁹. The efficiencies are parameterized as functions of both p_T and η and are drawn in figure 8.17.

⁴⁹Requiring such a hit is not possible, since the K_S^0 and Λ particles do not produce any hits in the detector due to them being neutral

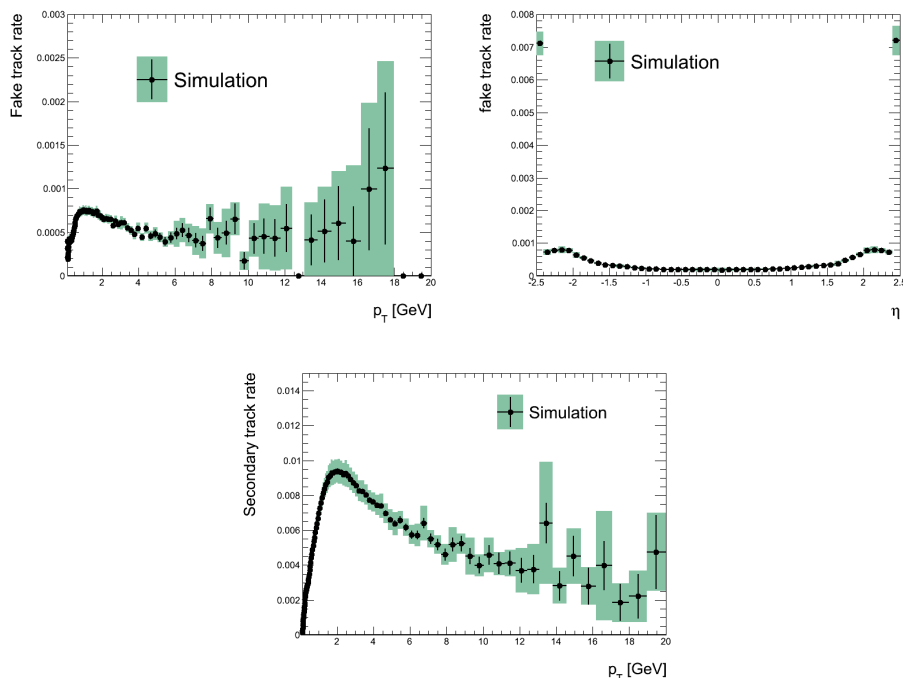


Figure 8.16: The fake track rate as a function of respectively p_T (top left) and η (top right). At the bottom the amount of secondary tracks is shown as a function of p_T . The statistical uncertainty is shown as vertical lines and the shaded areas represent the sum of the statistical and systematic uncertainties added in quadrature. The different rates were derived through the use of simulations.

The K_S^0 efficiency increases with higher transverse momentum until around 1 GeV, where it becomes steady at an efficiency of $\sim 40\%$. The Λ efficiency shows similar trends except that it only increase to a steady value at $\sim 25\%$. The efficiency is almost flat in η around zero, but for higher absolute values of η it starts to decrease.

For each bin in the final distribution the correction is calculated as the average of the individual corrections from the K_S^0 or Λ candidates entering this bin. In principle a better correction would be obtained by splitting each bin in the final distribution in both p_T and η , similar to the binning used in the efficiency calculations. The problem with this method is the limited statistics available afterwards. Binning in both $\Delta\phi$, p_T and η would result in each mass histogram only having $\sim \frac{1}{20 \cdot 20 \cdot 20} = \frac{1}{8000}$ of the total statistics⁵⁰

⁵⁰ Assuming an equal amount of data in each bin and binning in twenty bins.

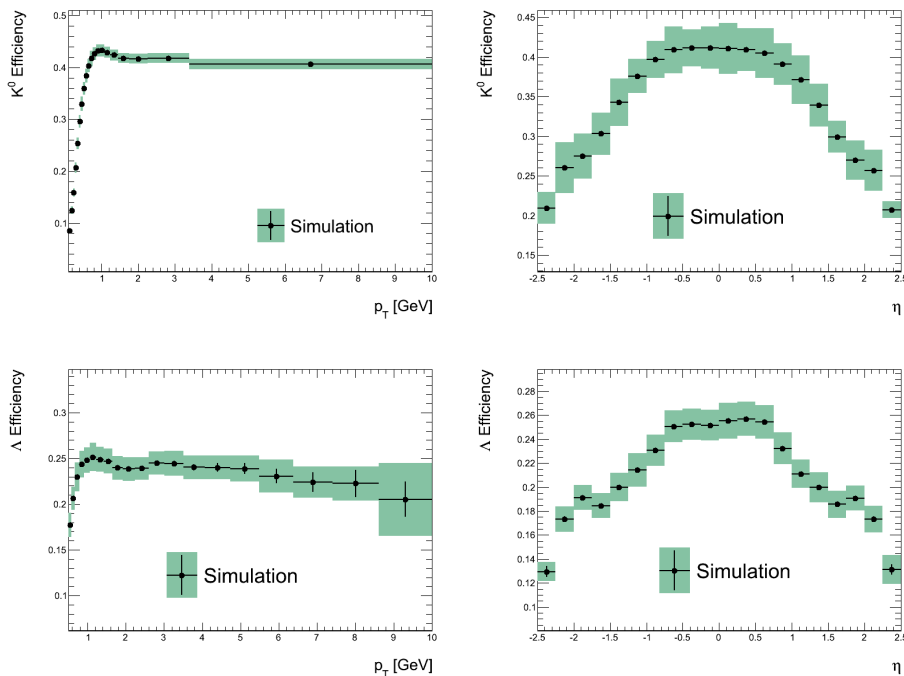


Figure 8.17: The efficiencies for reconstruction of K_S^0 (top) and Λ (bottom) hadrons. The efficiency is parameterized as a function of p_T (left) and η (right). The efficiencies are derived through simulation by comparing the number of matched particles to the number of generated particles. The statistical errors are shown as vertical lines and the shaded areas show both the systematic and statistical uncertainty.

and the fits would have a very hard time converging. Therefore this method was abandoned in favor of using the average correction.

8.7.4 Final correction

A correction to all the final distributions is applied to handle the difference between the number of fitted particles and the number of matched particles, and bin-to-bin migration.

By comparing the number of K_S^0 or Λ particles from the fit to the number of matched particles put into the mass histogram, it is possible to test the correctness of the fit. If the fit worked correctly it would produce a distribution with the number of matched particles as the mean, which is almost the case for K_S^0 . For Λ particles the fit tends to overestimate the number of Λ particles compared to the number found by matching.

The bin-to-bin migration comes from miss identified leading jets. If for instance the leading jet is not reconstructed correctly, the next to leading jet will be tagged as the leading jet and thus the $\Delta\phi$ between the leading jet and the K_S^0 and Λ particles will not be correct. This leads to the particle being added to the wrong bin, hence the name bin-to-bin migration.

To correct for these two effects, a final bin-by-bin correction is implemented. This correction is calculated for each bin by dividing the reconstructed value with the generated value. The final correction can be seen in figure 8.18 for K_S^0 and Λ particles, respectively. The K_S^0 correction is constant and only of the order of $\sim 3\%$. The Λ correction is not flat and instead decreases for lower values of $\Delta\phi$. The correction was not expected to depend upon $\Delta\phi$ and it has not been possible to find any explanation for this dependency. Therefore, an additional systematic uncertainty is added to account for the unexpected behavior (section 9.6).

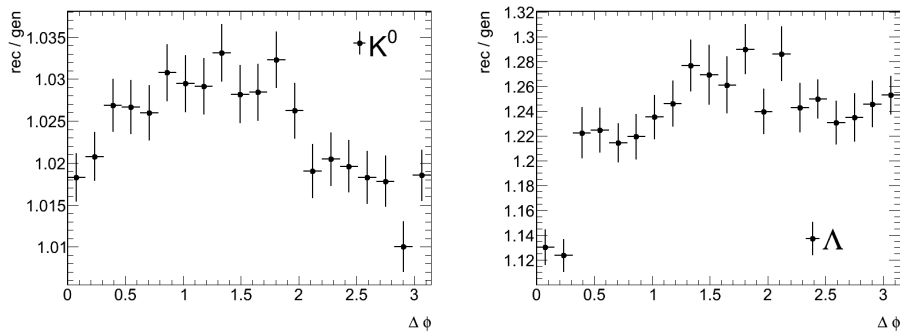


Figure 8.18: The final bin-by-bin correction shown for K_S^0 (left) and Λ (right). The vertical lines indicate the statistical uncertainty from limited MC statistics.

8.8 Differences between the analyses for the different final distributions

In the following sections I will describe the differences between the presented analysis used to find the angular multiplicity density and the other final distributions.

8.8.1 $K_S^0(\Lambda)$ multiplicity density as a function of $p_T^{\text{leading jet}}$

The multiplicity density as a function of $p_T^{\text{leading jet}}$ follows an almost similar procedure as described for the angular multiplicity density. The difference is of course the binning in $p_T^{\text{leading jet}}$ instead of $\Delta\phi$. The final correction is shown in the bottom of figure 8.19 and a clear tendency is observed. This effect can be explained by bin-to-bin migration for the leading jet p_T .

To show that bin-to-bin migration is responsible, a simple estimate was made of the qualitative and quantitative effects. In general the detector reconstructs a lower transverse momentum for the jet compared to the generated jet transverse momentum, due to not finding all the tracks in the jet. To estimate the size, a profile histogram was filled with the generated jet p_T and the reconstructed jet p_T (see figure 8.19). To obtain the scaling factor (often referred to as the jet energy scale), the profile was fitted with a linear fit and the slope was found to be $k = 0.8096 \pm 0.0001$.

To quantitatively estimate how the lower jet p_T changes the shape of the final distribution, first the MC final distribution was fitted to obtain a functional expression. The function used is shown in equation 8.7, where a, b, c and d are constants and erf is the error function⁵¹. The fit can be seen in figure 8.19 together with the final MC distribution.

$$g(p_T^{\text{leading jet}}) = a + b \cdot \text{erf}(c \cdot p_T) + d \cdot p_T \quad (8.7)$$

To estimate the final reconstructed distribution, function 8.7 was used with the same parameters, but instead of p_T using $\frac{p_T}{k}$, where k is the previously found slope. The estimated final correction is thus the estimated reconstructed distribution divided with the generated distribution:

$$\frac{\text{Rec}}{\text{MC}}(p_T^{\text{leading jet}}) = \frac{a + b \cdot \text{erf}(\frac{c}{k} \cdot p_T^{\text{leading jet}})}{a + b \cdot \text{erf}(c \cdot p_T^{\text{leading jet}})} \quad (8.8)$$

where $p_T^{\text{leading jet}}$ refers to the generated leading jet p_T . In figure 8.19 the simple estimate is plotted together with the simulated final distribution. The two curves do not match entirely because fluctuations are missing in the estimated effect, but the size of the effect and the general structure is similar. Hence, it is plausible that bin-to-bin migration explains the tendency observed in the final correction.

⁵¹This choice of function only reflects the shape of the function and do not have any physical interpretation.

8.8 Differences between the analyses for the different final distributions

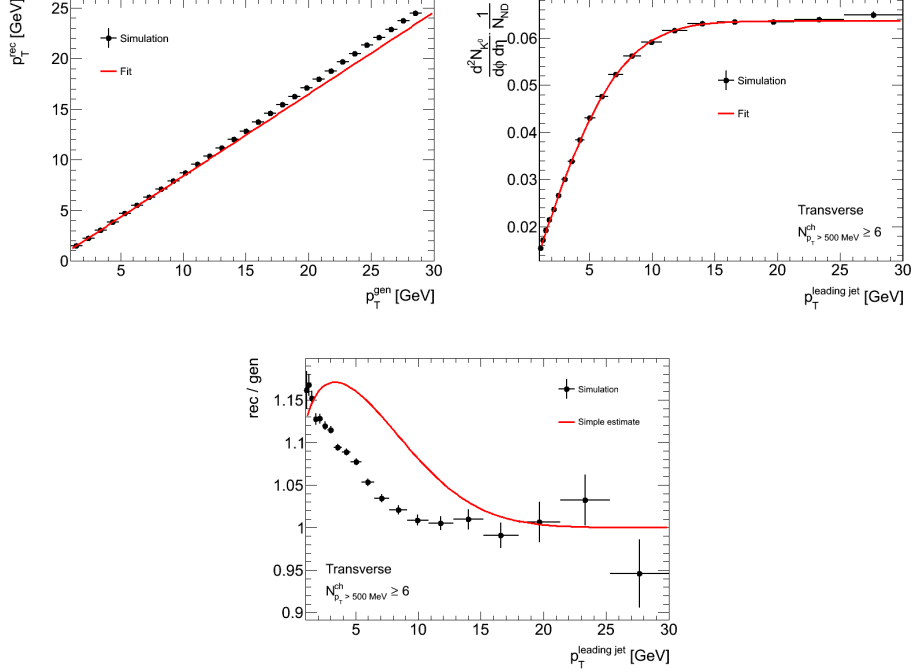


Figure 8.19: The top left figure shows a comparison between the generated leading jet p_T and the reconstructed leading jet p_T . At the top right is shown the multiplicity density vs. $p_T^{\text{leading jet}}$ at generator level, together with a fit described in equation 8.7. The bottom plot is the final correction (reconstructed divided by generated) for the K_S^0 multiplicity density distribution. The vertical lines are the statistical errors.

8.8.2 The average p_T distribution and the sum p_T distribution

The average p_T distribution and the sum p_T distribution use the same data selection, event selection and secondary vertex selection. But, since p_T of the K_S^0 (Λ) particle is needed; it is not possible to use the fitting method described above. Instead a simple cut on the invariant mass is imposed, such that it is possible to separate signal from background on an individual basis. The final correction at the end accounts for any background passing the mass cut. The average p_T is calculated as a weighted average for all K_S^0 (Λ) particles in all events, where each single particle is weighted according both to the event weight and the K_S^0 (Λ) efficiency.

The $\sum p_T$ is calculated for each event, as the sum of the K_S^0 (Λ) p_T multiplied by the corresponding K_S^0 (Λ) weight. The overall average is calculated as a

weighted mean, where each $\sum p_T$ is weighted by the event weight.

The final corrections show the same tendency as observed for multiplicity density correction and has the same explanation. The effect is smaller for the average p_T due to a general slower rise in the final distribution.

8.8.3 Track based distributions

To compare the final distributions with the track based results, similar distributions were calculated using tracks instead of K_S^0 or Λ particles. The analysis method follows almost similar patterns, except for not needing the fits to remove the background. The different selection cuts for tracks were already described in section 8.4 and the efficiency correction described in section 8.7.2.

Since the tracks are also used to calculate the leading jet, an inevitable bias is going to be introduced. This is especially apparent in the close proximity to the leading jet. Thus calculating $\Delta\phi$ for tracks with $\Delta\phi < 0.6$ is going to be very biased, since the track might have been used to determine the jet direction. This lead to the decision of using the leading track instead of the leading jet for the angular multiplicity density.

9 Systematic uncertainties

The systematic uncertainties were estimated by a combination of MC tests and data-driven tests. The systematic uncertainties considered were the following:

- Variations of cuts
- Material distribution
- Model dependency
- Fitting method (MC statistics)
- Bin-to-bin migration
- Final correction for Λ

I will describe how these were estimated in the following sections. In the end I will summarize the size of the different systematic uncertainties.

9.1 Systematic uncertainties from variation of cuts

The systematic uncertainty from the selection cuts imposed on the K_S^0 and Λ candidates were found by individually varying the following cuts, while keeping the other cuts constant:

- The d_{xy} cut was removed.
- The CosThetaPointing cut was removed.
- The number of hits required on the decay tracks was changed from 2 SCT hits to 4 silicon hits.
- The χ^2 cut was changed from 15 to 7.

The efficiency of the change in cut values were measured by fitting the mass histogram before and after applying the cuts in both data and reconstructed MC, respectively. To get the systematic uncertainty, the ratio between the MC and data efficiencies was used. In table 9.1 the different systematic uncertainties are shown for both the K_S^0 and Λ cuts. The predominant uncertainty comes from the CosThetaPointing cut and it was found to be 1.5 % for K_S^0 and 4 % for Λ . The total systematic uncertainty from the cuts was calculated by adding the different components in quadrature: 1.5 % for K_S^0 and 4.1 % for Λ .

9.2 Systematic uncertainties from adding extra material

	ϵ_{data}	ϵ_{MC}	$\left \frac{\epsilon_{\text{MC}} - \epsilon_{\text{data}}}{\epsilon_{\text{MC}}} \right $
K_S^0			
d_{xy}	0.9994	0.9991	0.02 %
CosThetaPointing	0.886	0.872	1.5 %
Extra hits	0.9799	0.9792	0.07 %
χ^2	0.9822	0.9815	0.07 %
Λ			
d_{xy}	0.974	0.980	0.6 %
CosThetaPointing	0.91	0.95	4 %
Extra hits	0.9969	0.9936	0.3 %
χ^2	0.9703	0.9696	0.08 %

Table 9.1: The efficiencies of the different cuts applied to the secondary vertices. The efficiencies are found by fitting the mass histogram before and after applying the cut. The systematic uncertainty is obtained by taking the ratio between the efficiency for the MC and data.

Since this systematic uncertainty only describes the overall efficiency, it does not affect the average p_T measurements. Therefore it was not included in the calculation for the total systematic uncertainty on the average p_T .

9.2 Systematic uncertainties from adding extra material

The material distribution has been validated to a maximum uncertainty of 7% in the inner detector⁵². To obtain this uncertainty, secondary vertices from hadronic interactions between primary particles and the material were studied. By comparing the distribution of these secondary vertices in the MC simulation with the same distribution from the data, it was possible to evaluate the simulation of the material.

A simulation with 10% extra material was used to calculate the uncertainty in the final distributions due to the material uncertainty. The efficiencies were recalculated with the new simulation and the data was corrected according to these efficiencies. A comparison between the data corrected with the standard simulation and the simulation with extra material was made and the difference was taken as the systematic uncertainty. To account for the difference between the 10% in the simulation and the 7% uncertainty in the material, a factor of 0.7 was multiplied to the difference.

⁵²Only published in internal notes so far.

Using the difference between the two simulations overestimates the uncertainty, because it does not take into account statistical fluctuations due to limited MC statistics. In the case of high statistics, this overestimation is very small and negligible. But for low MC statistics, the overestimation becomes rather large. Thus for Λ particles in bins with a high cut on $p_T^{\text{leading jet}}$, the estimated uncertainty becomes too large.

9.3 Systematic uncertainties from model dependency

The model dependency was studied by comparing two different event generators. In the ATLAS UE studies [25], the highest discrepancy was found between the PYTHIA and PHOJET event generators, thus it was decided to use these to estimate the model dependency. The systematic uncertainty was calculated similar to the method used for extra material, i.e. the data was reconstructed both with the efficiencies determined from the PYTHIA simulation and the PHOJET simulation and the difference was used as the systematic uncertainty.

9.4 Systematic uncertainties from the fitting method

The systematic uncertainty from the fitting method was determined with the use of MC simulation. The number of fitted particles was divided by the number of matched particles and the distributions can be seen in figure 9.1. The ratio between the fitted and matched particles was observed to be almost flat for the distributions. In this case, the systematic uncertainty was taken as the statistical uncertainty on the ratio between the fitted and matched particles. Thus, this systematic uncertainty also incorporates the systematic uncertainty from limited MC statistics.

This systematic uncertainty was only used for the final distributions which were calculated by fitting. For the other distributions, the systematic uncertainty from limited MC statistics was taken as the statistical uncertainty in the final correction.

9.5 Systematic uncertainties from the bin-to-bin migration correction

The biggest uncertainty on the bin-to-bin migration comes from misunderstanding the jet energy scale. A comparison between jets reconstructed with the inner detector (using tracks) and the same jets reconstructed in

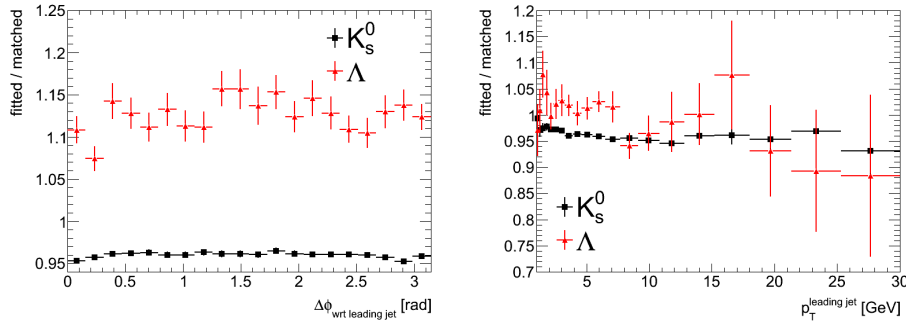


Figure 9.1: The number of fitted particle divided by the number of matched particles for the angular multiplicity density distribution (left) and the multiplicity density as a function of $p_T^{\text{leading jet}}$ (right). The distributions were found by the use of MC simulation.

the calorimeter (using the energy deposit) was made. The study concluded that the systematic uncertainty was 2%. Another method is to take the systematic uncertainty on the jet cross section and translate it into a systematic uncertainty on the energy scale. In a recent ATLAS study on track jets [46], the uncertainty on the cross section was found to be around 8%. This translates into an uncertainty on the jet scale to be around 2%, which agrees with the other study.

The uncertainty from the jet scale was translated into an uncertainty on the final distribution, by the use of the functional description of the final distribution (equation 8.7). The relative uncertainty on the final distribution, g , was calculated according to equation 9.1.

$$\frac{\delta g}{g} = \frac{1}{g} \frac{dg}{dp_T} \delta p_T = \frac{p_T}{g} \frac{dg}{dp_T} \frac{\delta(p_T)}{p_T} \quad (9.1)$$

9.6 Systematic uncertainties from final correction for Λ

The final correction for Λ particles was observed to depend upon $\Delta\phi$ (figure 8.18), and since no dependency was expected, a systematic uncertainty was introduced to account for this. To estimate the size of the systematic uncertainty, the part of the final correction coming from the fitting method was removed (see figure 9.2). Since the correction was found to vary between 1.02 and 1.12, a systematic uncertainty of 5% was included.

9.7 Summary of the systematic uncertainties

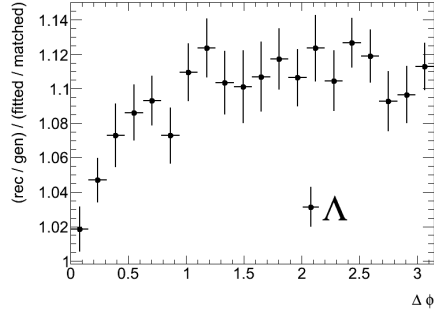


Figure 9.2: The final correction for Λ particles, where the part originating from the fitting method was removed.

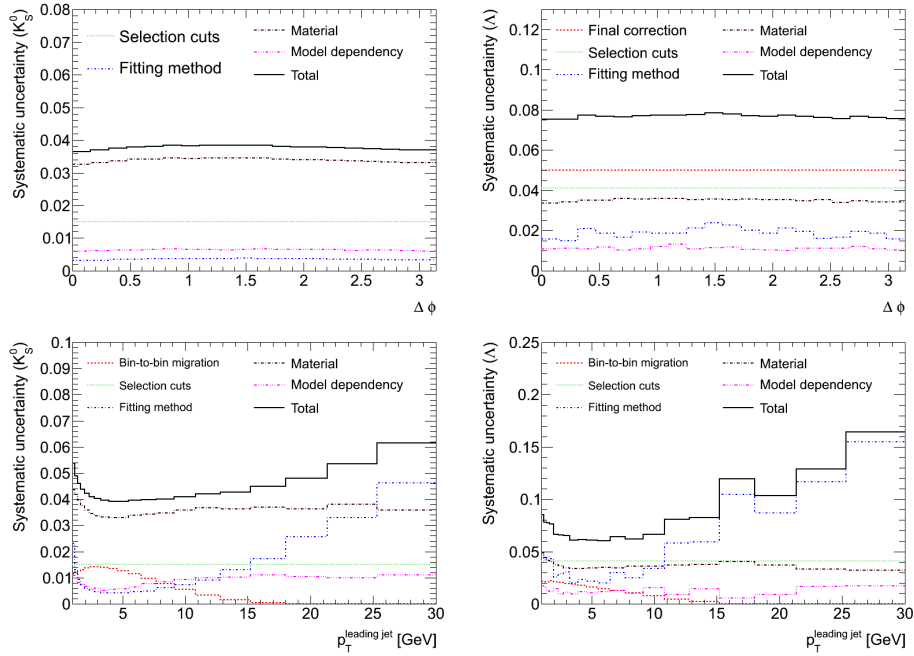


Figure 9.3: Summary of the systematic uncertainties for the different distributions. The top plots show the systematic uncertainty on angular multiplicity density for K_S^0 (left) and Λ (right). The cut on the leading jet transverse momentum was set to 1 GeV ($p_T^{\text{leading jet}} > 1 \text{ GeV}$). The bottom plots show the systematic uncertainties on the multiplicity density distribution in the transverse region. The total line indicates the sum of all the systematic uncertainties added in quadrature.

9.7 Summary of the systematic uncertainties

The value for the different systematic uncertainties can be seen in figure 9.3 and 9.4, together with the total systematic uncertainty found by adding

the individual uncertainties in quadrature. Figure 9.3 shows the systematic uncertainty for the angular distributions and the K_S^0 (Λ) multiplicity in the transverse region. For the angular distribution of K_S^0 particles, the systematic uncertainty stays just below 4% in the whole region. The dominant contribution is from the material distribution, which is almost stable at 3.3%. The systematic uncertainty from the model dependency and the fitting method both stays below 1%. For Λ particles, the final correction uncertainty becomes the dominant source of uncertainty with its 5%. The systematic uncertainty from the cut selections increases to 4.1% and the uncertainty from the material remains unchanged. The uncertainty from the fitting method is increased to around 2%, due to the lower amount of statistics for Λ particles.

For the K_S^0 multiplicity the systematic uncertainty is dominated by the material uncertainty for low leading jet p_T . As the leading jet p_T increases, the amount of statistics decreases and the systematic uncertainty from the fitting method starts to take over. The systematic uncertainties from bin-to-bin migration peaks at $p_T^{\text{leading jet}} = 3 \text{ GeV}$ and goes to zero as the leading jet becomes above 18 GeV. This is because the final distributions becomes almost flat at high leading jet p_T , and thus bin-to-bin migration does not change anything. The Λ distribution has much lower statistics and is thus much more dominated by the uncertainty from the fitting method. At the highest leading jet p_T , the total uncertainty has maximum with 16%.

The systematic uncertainty on the average momentum is lower than for the other distributions. This is due to the uncertainty being largest on the overall number of K_S^0 (Λ) particles and with this number not being important in the measurement of the average momentum, the overall uncertainty becomes lower. The total uncertainty starts around 0.8% and then increases to 2% for K^0 . For Λ the systematic uncertainty starts about 2% and ends at $\sim 5\%$. The high increase in the uncertainty in the model dependency for the last bin is an example of limited MC statistics and is thus not due to model dependency.

The systematic uncertainties for the $\sum p_T$ distribution shows very similar tendency as for the multiplicity distributions: The material distributions dominate the high statistics areas (low $p_T^{\text{leading jet}}$) and the MC statistics (fitting method) becomes dominant in the lower statistic cases (high $p_T^{\text{leading jet}}$).

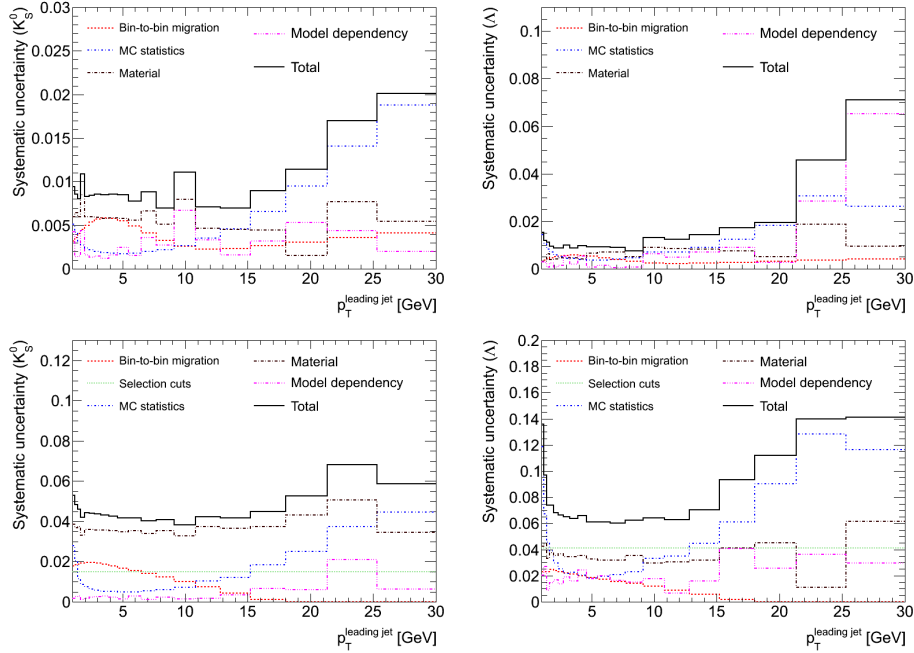


Figure 9.4: Summary of the systematic uncertainties for the different distributions. The top plot shows the systematic uncertainty on the average p_T distributions for K_S^0 (left) and Λ (right) and the bottom plots show the systematic uncertainties on the $\sum p_T$ distributions. All the plots are in the transverse regions. The total line indicates the sum of all the systematic uncertainties added in quadrature.

10 Lifetime distribution

Since the lifetime distribution is known to very high precision and it does not depend on the type of collision, it provides a good test of the analysis method. Especially it tests the ability for the simulation to provide the correct efficiencies as a function of the transverse decay length, since this would otherwise change the measured lifetime. To obtain the lifetime, the data was binned in bins of $c\tau$, where c is the speed of light and τ is the proper decay time⁵³. This removes the dependency on p_T , which otherwise existed due to time dilation from the special relativity theory. Each bin was corrected for the average efficiency, similar to the correction used in the final plots. The final correction was found by dividing the reconstructed distribution with the expected true distribution (an exponential decay). Since only the shape was of interest, all histograms were normalized to have the same area below the curve ($= 1$).

⁵³The proper decay time is the decay time in the rest frame of the particle.

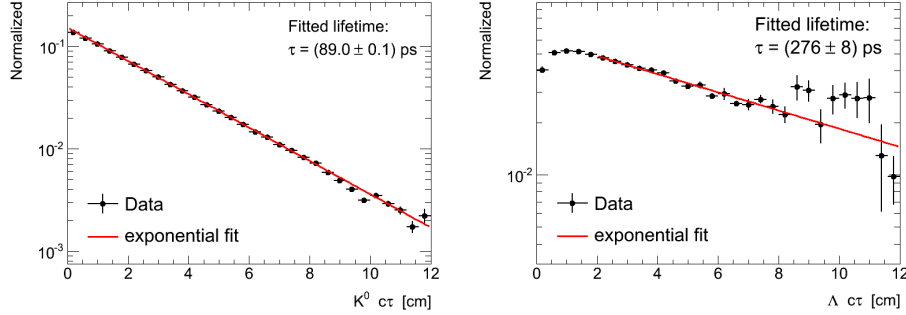


Figure 10.1: The $c\tau$ distributions for K_S^0 (left) and Λ (right) is plotted together with an exponential fit. The distributions were corrected for detector efficiencies and a final bin-by-bin correction was applied. The vertical lines indicate the statistical uncertainty.

In figure 10.1 the corrected $c\tau$ distributions are shown for respectively the K_S^0 meson and the Λ baryon. The corrected data has the expected exponential behavior for both K_S^0 and Λ particles. To obtain the lifetime, the corrected data was fitted with an exponential function. The K_S^0 lifetime was found to be (89.0 ± 0.1) ps, which agrees rather well with the known value (89.58 ps), considering that no systematic uncertainties were included. One could use the deviation as a systematic uncertainty ($\frac{|\tau_{\text{data}} - \tau_{\text{PDG}}|}{\tau_{\text{PDG}}} = 0.006$), but the size is negligible compared to other systematic uncertainties included. Also including this uncertainty would most likely introduce an overcounting of the systematic uncertainties, since the lifetime distribution is affected by the material distribution and thus the uncertainty from the material distribution would be counted twice.

Similar to the K_S^0 distribution, the lifetime of the Λ baryon was found by fitting with an exponential function. Due to the cut on d_{xy} ($d_{xy} < 17$ mm), the Λ distribution was only fitted from $c\tau = 2$ cm to $c\tau = 12$ cm. The fitted lifetime was found to be $\tau = (276 \pm 8)$ ps, which agrees within 5% ($\frac{|\tau_{\text{data}} - \tau_{\text{PDG}}|}{\tau_{\text{PDG}}} = 0.049$) of the known lifetime (263.2 ps). This indicates that the method works as expected.

11 Results

11.1 Angular multiplicity density

The K_S^0 angular multiplicity distribution with respect to the leading jet is shown in figure 11.1. The data is presented for four different minimum leading jet p_T cuts. The increase observed around $\Delta\phi = 0$ is due to K_S^0 produced inside the leading jet. It can also be observed that for higher leading jet p_T the jet like structure becomes more apparent. The two different PYTHIA tunes and the PHOJET MC predicts too few K_S^0 compared to the observed. The highest discrepancy is seen in the transverse area, where the MC simulation predicts about 30 – 40 % below the observed. In the toward region the discrepancy is lower and especially in the case of low p_T leading jets, where the difference is only 5 – 20 %. The HERWIG MC shows complete opposite tendencies and predicts around 50 – 70 % too many K_S^0 mesons⁵⁴.

There are several possible physical explanation for the observed discrepancy, one possibility could be that the event generators simply produce an overall too low amount of K_S^0 particles. This would result in the ratio between the event generators and the data being flat. Another possibility is that only the UE predicts too few K_S^0 mesons, and since the UE produces the same amount of particles in all $\Delta\phi$ bins, this would lead to a constant difference between the event generators and the data. The ratios found in figure 11.1 are not constant, but trying to distinguish between whether the ratios or differences (or neither) are constant is almost impossible since the overall distribution is rather flat. It is possible to enhance the jet structure in the distribution by imposing a cut on $\Delta\eta$ between the K_S^0 and the leading jet.

The same distributions as in figure 11.1 but with the additional requirement ($|\Delta\eta| < 1$) are shown in figure 11.2 and the enhanced jet structure is observed in the toward region. The measured ratio between the MC generators and the data in the toward region has come closer to one and one of the event generators predict too many K_S^0 particles for low leading jet p_T . For higher leading jet p_T the event generators starts to predict too few K_S^0 particles in the toward region again. This illustrates that at least for low leading jet

⁵⁴For all the results following the HERWIG generator will tend to disagree dramatically with all other MC simulation. The HERWIG simulation used is a standard ATLAS production, but the huge discrepancy could indicate that the HERWIG simulation was not tuned correctly. I will present the HERWIG MC for all the distributions, but I will not comment further on the discrepancy between the data and the HERWIG simulation.

11.1 Angular multiplicity density

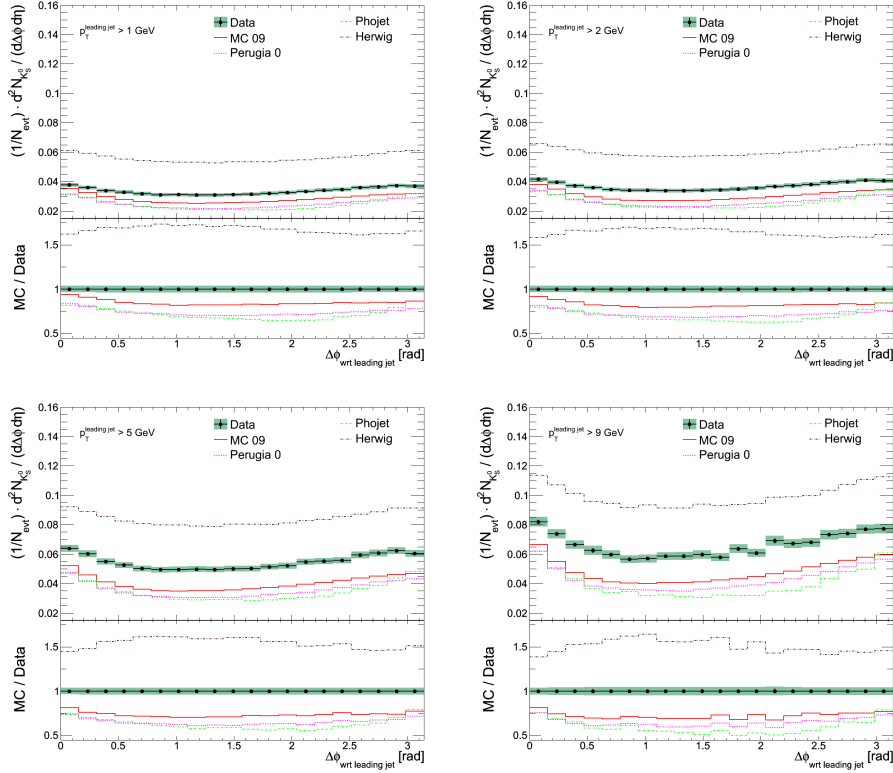


Figure 11.1: The angular multiplicity density distribution of K_S^0 particles with respect to the leading jet. The data are corrected back to particle level and are compared to several MC simulations. The distributions are separated according to different cuts on the leading jet p_T . The vertical error bars show the statistical uncertainty and the shaded areas show the systematic and statistical uncertainty added in quadrature.

p_T the ratio between event generators and the data is non-constant. The difference is also seen to be non-constant and thus an overall increase of UE activity cannot reproduce the measured results. One possibility could be that the event generators predicts too many K_S^0 particles within the hard interaction and too few in the UE. This would not be unlikely if some parameter, such as the $\frac{s}{u}$ ratio in the Lund string fragmentation, had been tuned to agree with the average kaon production. But it is not possible to make final conclusion from these results alone and further studies will be needed.

The angular distribution for Λ particles with respect to the leading jet can

11.1 Angular multiplicity density

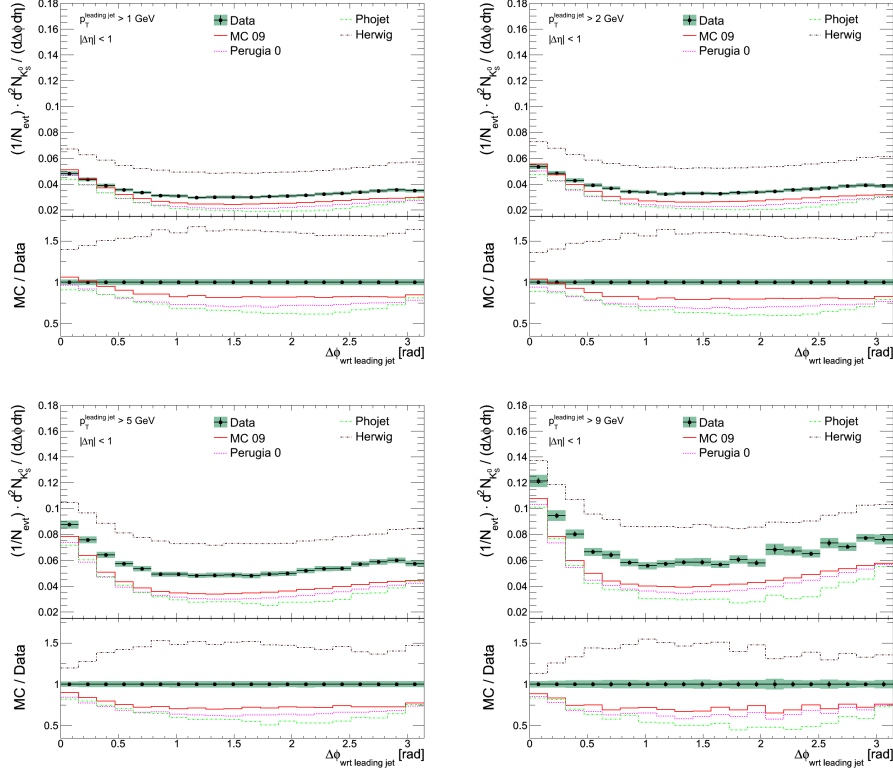


Figure 11.2: The angular multiplicity density distribution of K_S^0 particles with respect to the leading jet with an additional cut on $\Delta\eta$ imposed to enhance the jet structure. The data are corrected back to particle level and are compared to several MC simulations. The distributions are separated according to different cuts on the leading jet p_T . The vertical error bars show the statistical uncertainty and the shaded areas show the systematic and statistical uncertainty added in quadrature.

be seen in figure 11.3. The data shows the same structure as was measured for the K_S^0 , but the overall level is lower for Λ particles. At $\Delta\phi = 0$ the production of K_S^0 particles is found to be $\frac{1}{N_{\text{evt}}} \frac{d^2 N_{K_S^0}}{d\Delta\phi d\eta} = 0.038$, whereas for Λ baryons the observed number is $\frac{1}{N_{\text{evt}}} \frac{d^2 N_{\Lambda}}{d\Delta\phi d\eta} = 0.0063$ for $p_T^{\text{leading jet}} > 1 \text{ GeV}$. Thus the ratio between K_S^0 and Λ is: $\frac{N(K_S^0)}{N(\Lambda)} = 6.0$. This is expected, since the Λ particle is heavier than the K_S^0 particle, resulting in it being harder to produce.

The measured amount of Λ baryons is also much higher than the predicted

11.1 Angular multiplicity density

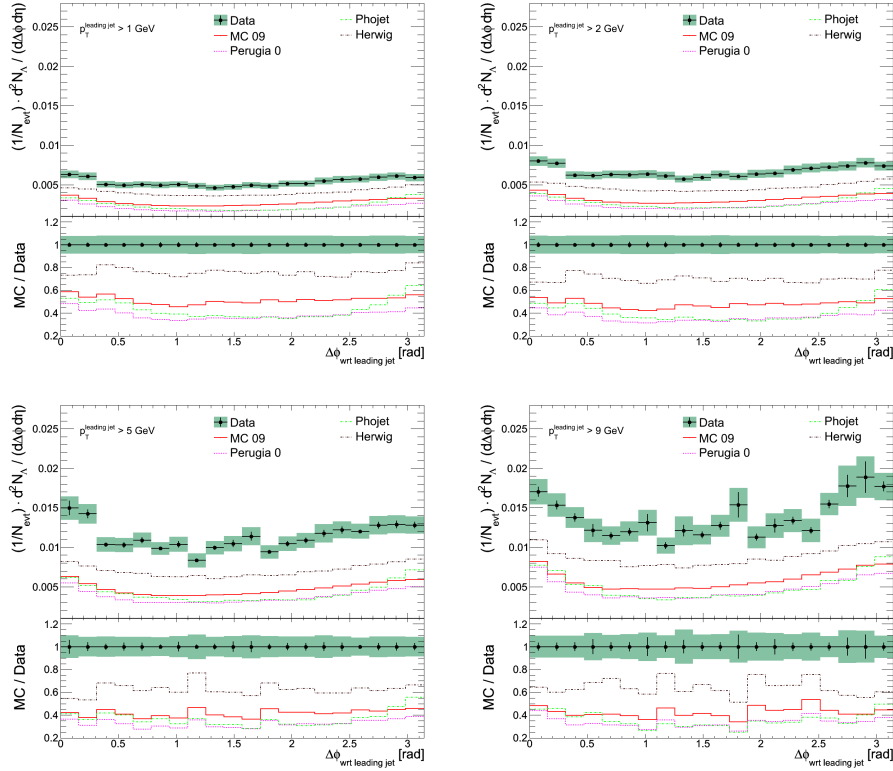


Figure 11.3: The angular multiplicity density distribution of Λ particles with respect to the leading jet. The data are corrected back to particle level and are compared to several MC simulations. The distributions are separated according to different cuts on the leading jet p_T . The vertical error bars show the statistical uncertainty and the shaded areas show the systematic and statistical uncertainty added in quadrature.

number from the event generators. In general the event generators only predict between 30 – 60 % compared to the measured number. The MC09 tune is slightly closer to the measured values, but it is still nowhere close to providing a good description. The discrepancy seems to be slightly larger in the transverse region (as observed for the K_S^0 particles too), but the effect is rather small and it is hard to tell whether it is just statistical fluctuation or if the discrepancy varies.

Similar as for K_S^0 , it is possible to enhance the jet structure to test how the event generators react compared to the data. In figure 11.4 the angular density distributions are shown with the additional cut on $\Delta\eta$. The MC and data gets slightly closer to one another within the toward region (as

11.2 Multiplicity density vs. $p_T^{\text{leading jet}}$

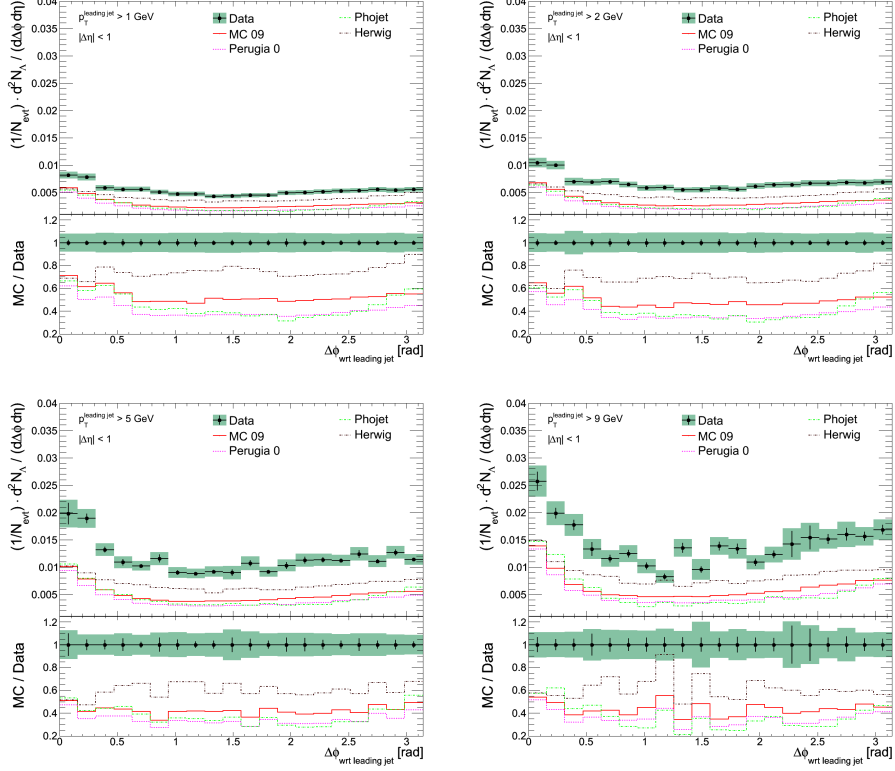


Figure 11.4: The angular multiplicity density distribution of Λ particles with respect to the leading jet with an additional cut on $\Delta\eta$ imposed to enhance the jet structure. The data are corrected back to particle level and are compared to several MC simulations. The distributions are separated according to different cuts on the leading jet p_T . The vertical error bars show the statistical uncertainty and the shaded areas show the systematic and statistical uncertainty added in quadrature.

compared to the distributions without the $\Delta\eta$ cut), but it is not very significant compared to the statistical uncertainty. Especially since the two first bins do not follow the rest of the distribution.

11.2 Multiplicity density vs. $p_T^{\text{leading jet}}$

The multiplicity densities for respectively K_S^0 and Λ particles as a function of the leading jet p_T are shown in figure 11.5. The data is separated into three regions according to $\Delta\phi$, namely the toward, transverse and away region. For low $p_T^{\text{leading jet}}$ the number of K_S^0 (Λ) particles increases almost linearly with the leading jet p_T . But at around $p_T^{\text{leading jet}} \approx 8 - 9$ GeV, the distributions becomes almost constant, this effect is observed in all the

three regions and both for K_S^0 and Λ particles. The level of the flat plateau is slightly lower in the transverse region than the toward region, which again is lower than the away region. The transverse region is expected to show this lower level of activity due to it not being influenced by the hard interaction. The reason that the away region being higher than the toward region is that most of the p_T in the toward region is used to create the leading jet, and due to momentum conservation the total amount of available p_T is expected to be similar in the toward and away regions.

Again the event generators predicts too few particles, for K_S^0 the event generators predict around 85 – 95 % at the lowest p_T lead bin. This value decreases until $p_T^{\text{leading jet}} = 7 - 8 \text{ GeV}$, where it becomes almost steady at 50 – 75 % depending on the event generator. The same behavior is observed for Λ baryons, except that the steady region is 35–50 % of the observed yield.

As can be seen from the event generators, it was expected that the distribution had a small positive inclination even at higher $p_T^{\text{leading jet}}$. It is not possible to see this effect in the data, but it is most likely due to the rather large statistical uncertainty for high $p_T^{\text{leading jet}}$ values.

11.3 Average transverse momentum vs. $p_T^{\text{leading jet}}$

The average p_T distributions are shown in figure 11.6. In the transverse region the average p_T distributions shows very similar trends as for the multiplicity density: Namely a rise for $p_T^{\text{leading jet}} < 8 - 9 \text{ GeV}$ followed by a constant plateau. In the toward region, the sharp rise is followed by a less steep rise for the K_S^0 particles, whereas it is not possible to tell whether it becomes steady or keeps rising for the Λ baryons. In the away region, the rise in the average p_T continues all the way, with only a small decrease in the slope.

The event generators describe the measured average p_T rather well. The only big discrepancy is between PHOJET and the data for K_S^0 in the transverse region. Otherwise the discrepancy stays within 10 % (except for a few bins with high statistical uncertainty).

11.4 Sum p_T vs. $p_T^{\text{leading jet}}$

The sum p_T distributions combines both the average p_T distributions and the multiplicity density, thus a rise in the beginning is expected as a combination of a higher number of particles and a higher average p_T . As $p_T^{\text{leading jet}}$

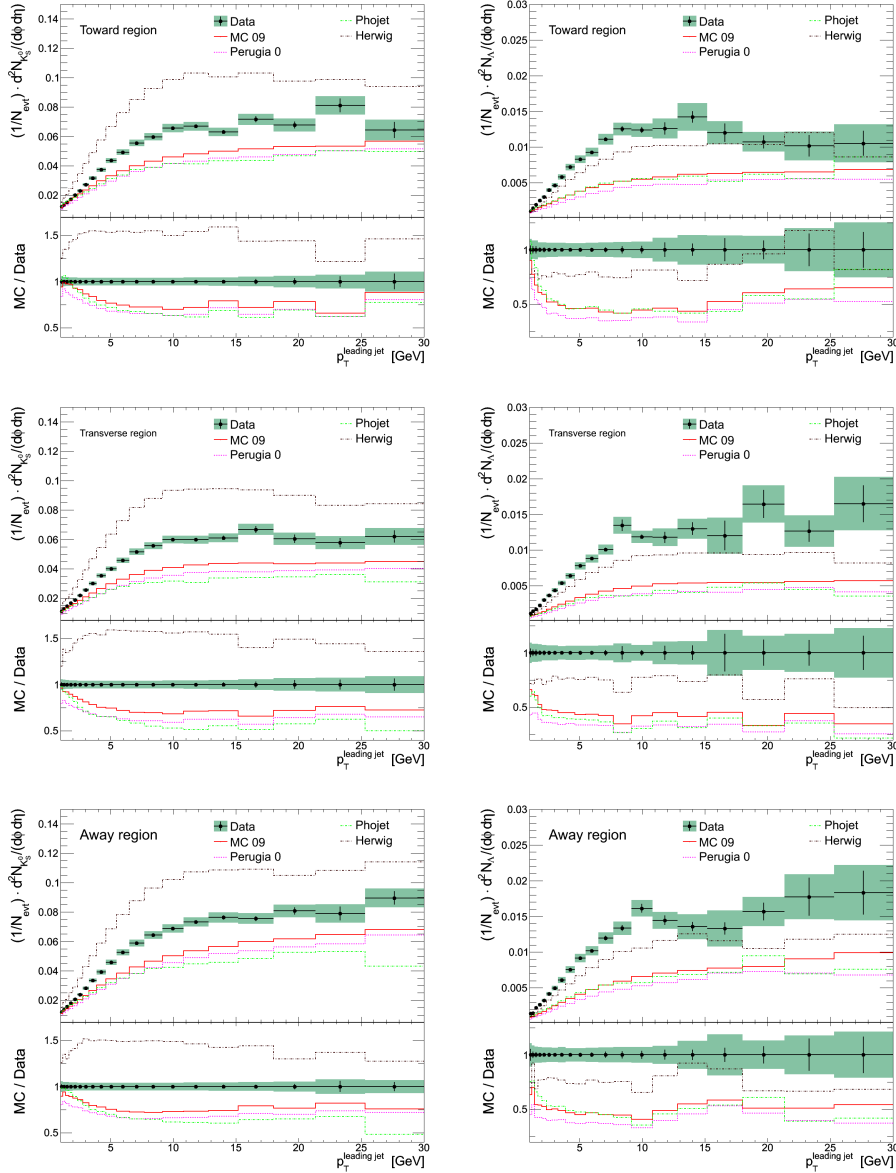


Figure 11.5: The multiplicity density vs. $p_T^{\text{leading jet}}$ for K_S^0 (left) and Λ (right) in the toward (top), transverse (middle) and away (bottom) region, respectively. The data is corrected back to particle level and is compared to several event generators. The vertical error bar indicates the statistical uncertainty and the shaded area shows the systematic and statistical uncertainty added in quadrature.

becomes above 8 – 9 GeV, the number of particles becomes almost steady, whereas the average p_T keeps increasing in the toward and away region,

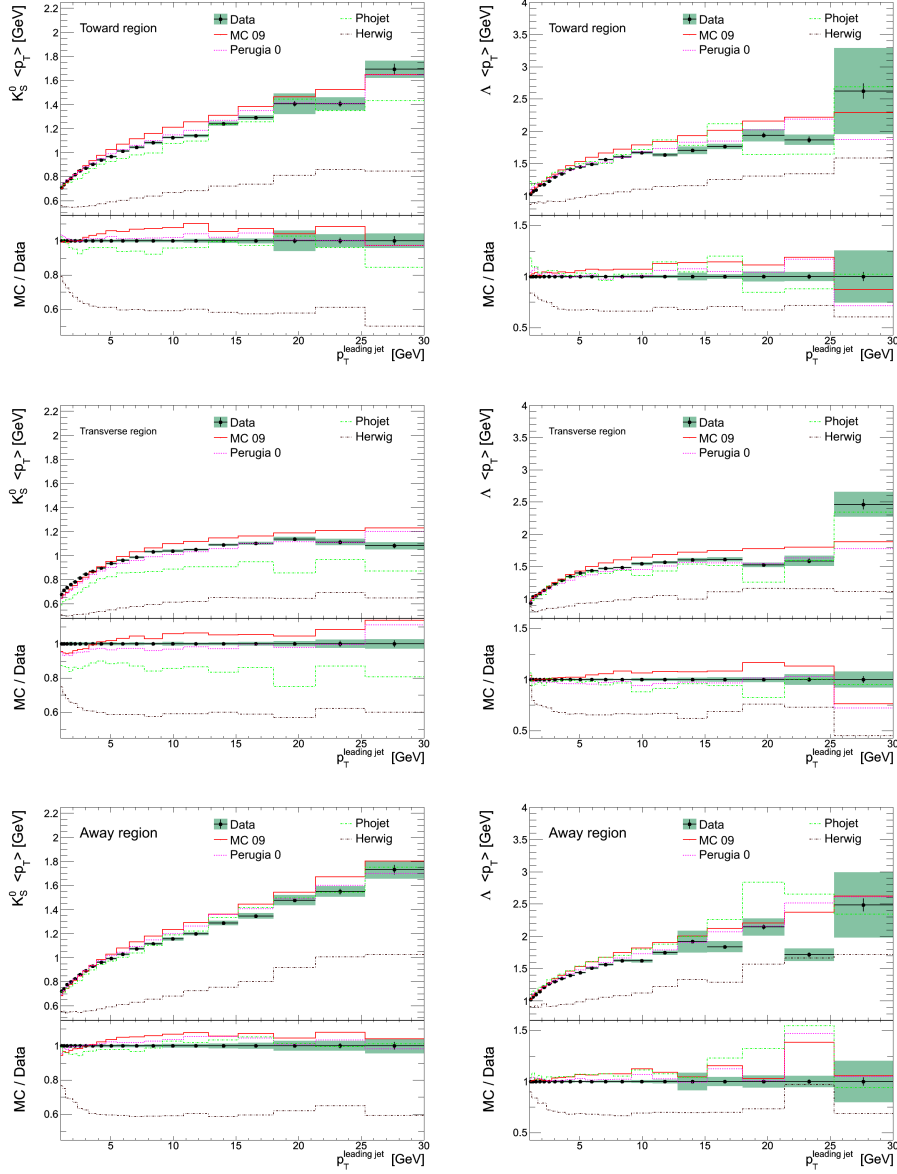


Figure 11.6: The average transverse momentum vs. $p_T^{\text{leading jet}}$ distribution for K_S^0 (left) and Λ (right) in the toward (top), transverse (middle) and away (bottom) region, respectively. The data are corrected back to particle level and are compared to several event generators. The vertical error bar indicates the statistical uncertainty and the shaded area shows the systematic and statistical uncertainty added in quadrature.

resulting in an increased sum p_T . These effects can be seen in figure 11.7, where the sum p_T distributions are shown. The event generators predict a too low $\sum p_T$, which is due them predicting too few K_S^0 and Λ hadrons.

11.5 Comparison to track based results

By comparing the previous results to track based results, it is possible to tell whether the observed deviations are only for hadrons with strange quarks or are a more generic feature for all particles. Almost all observed primary tracks are pions, since this is the lightest hadron. Thus the comparison to tracks is in principle a comparison between three different types of particles: K_S^0 , Λ and π^+/π^- . The main properties of the particles are listed in table 11.1.

	K_S^0	Λ	π^+/π^-
Mass [MeV]	497.614	1115.683	139.57018
Charge	0	0	± 1
Baryon number	0	1	0
Strangeness	-1/1	-1	0

Table 11.1: The main properties of the K_S^0 , Λ and π^+/π^- .

The ratios between the angular density distributions for respectively K_S^0 and Λ , and tracks can be seen in figure 11.8. The ratios are flat, except for a small increase in proximity to the leading track⁵⁵. The ratio is about ~ 0.026 for K_S^0 and $\sim 0.0045 - 0.006$ for Λ , which indicates their different production ratios⁵⁶. This number can be compared to the observed jet fragmentation at 45 GeV (from LEP). According to PDG [10], the ratio $\frac{N(K_S^0 \rightarrow \pi^+\pi^-)}{N(\pi^+) + N(\pi^-)}$ can be calculated:

$$\frac{N(K_S^0 \rightarrow \pi^+\pi^-)}{N(\pi^+) + N(\pi^-)} = \frac{\frac{1}{2} \cdot 0.692 \cdot 2.049}{2 \cdot 17.02} = 0.021 \quad (11.1)$$

⁵⁵In this plot the leading track was used instead of the leading jet. This is due to the bias introduced by using the tracks to both find the leading jet and afterwards calculate the distribution. Also note that the leading track was not added in the calculation of the angular multiplicity density distribution.

⁵⁶One has to account for the different phase-space cuts applied on the K_S^0 and Λ particles, thus this ratio does not directly give this number.

11.5 Comparison to track based results

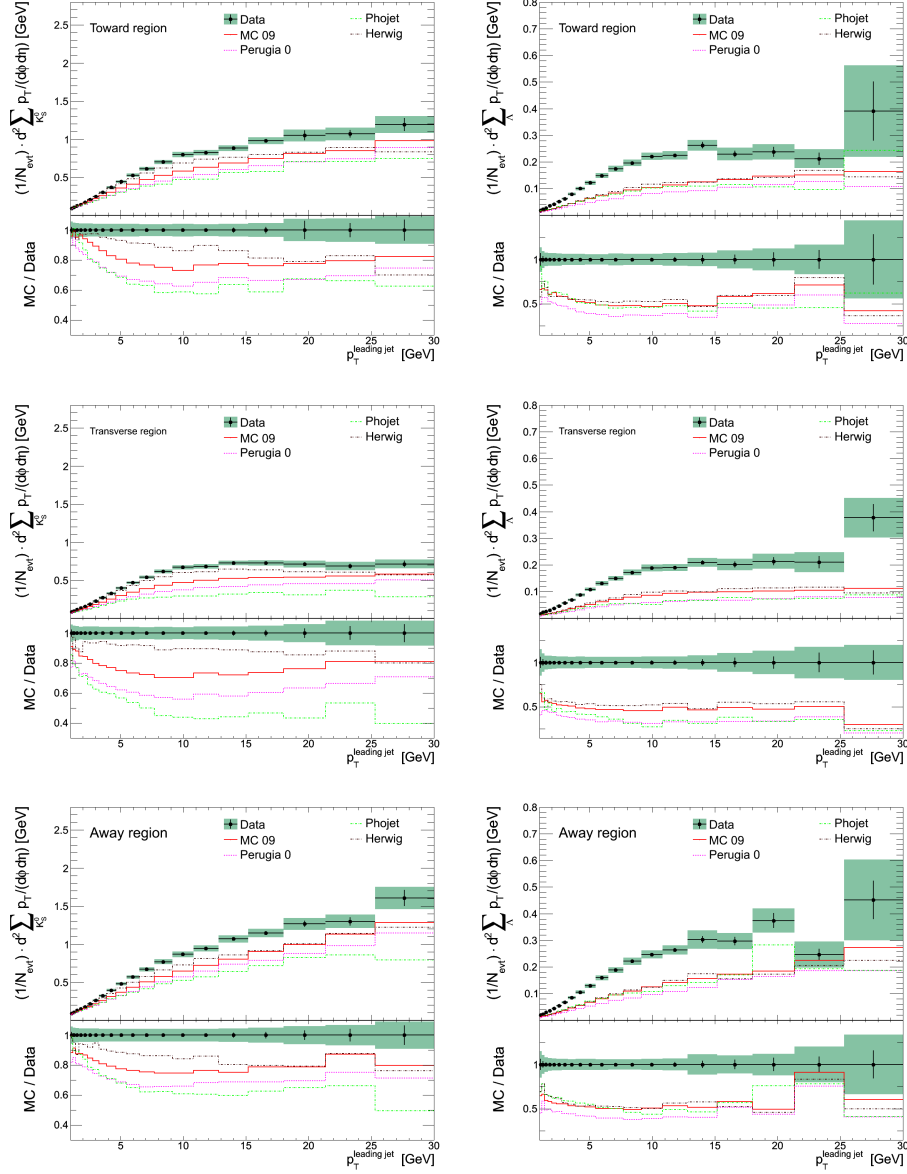


Figure 11.7: Sum p_T vs. $p_T^{\text{leading jet}}$ for K_S^0 (left) and Λ (right) in the toward (top), transverse (middle) and away (bottom) region, respectively. The data are corrected back to particle level and are compared to several event generators. The vertical error bar indicates the statistical uncertainty and the shaded area shows the systematic and statistical uncertainty added in quadrature.

Thus the ratio found at the LEP experiment is in agreement with the observed result for $\frac{N(K_S^0)}{N(\text{trk})}$. For Λ the ratio at LEP is found to be 0.0037,

which is lower than the measured value above.

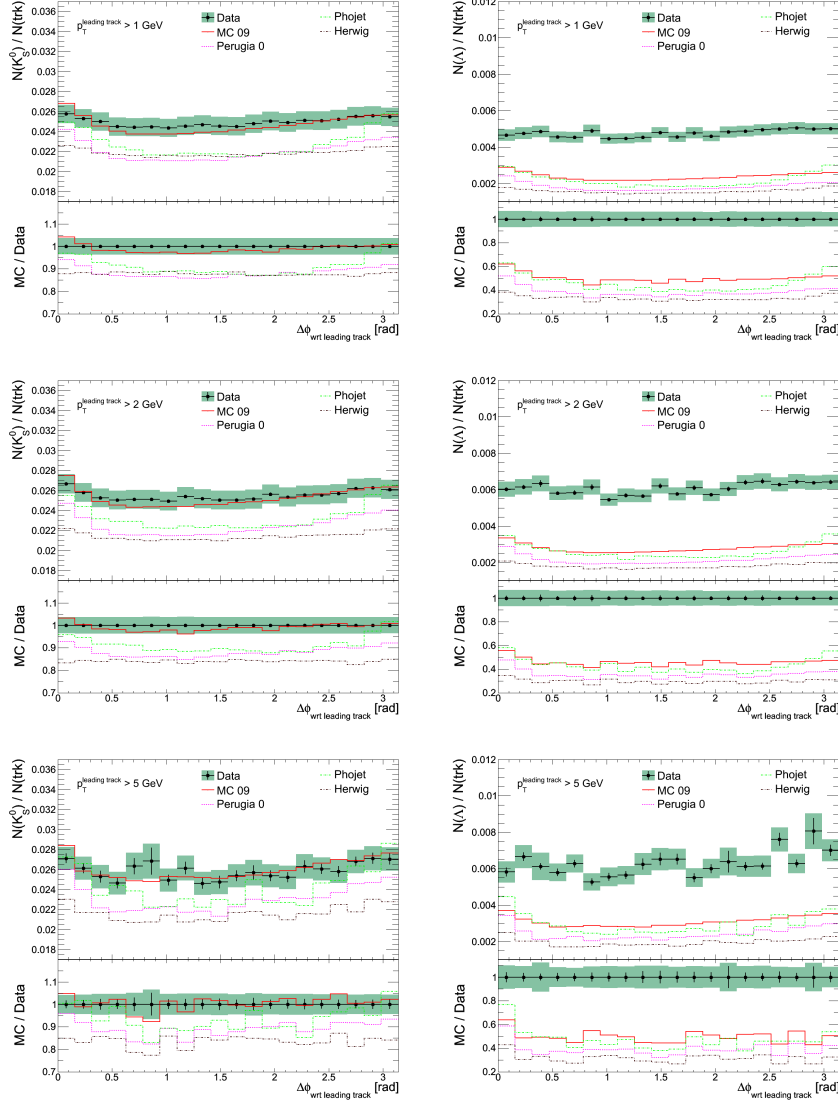


Figure 11.8: The ratio between $N_{K_S^0}$ and N_{trk} (left) and N_{Λ} and N_{trk} (right) as a function of $\Delta\phi$. The data are presented with three different cuts on $p_T^{\text{leading track}}$ (this is with leading track and not leading jet). The data are corrected back to particle level and are compared to several event generators. The vertical error bar indicates the statistical uncertainty and the shaded area shows the systematic and statistical uncertainty added in quadrature. The systematic uncertainty was calculated only for the $N_{K_S^0}$ (N_{Λ}), since the systematic uncertainty on the number of tracks was assumed to be smaller.

The MC09 tune describes the K_S^0 ratio within 5%, which indicates a good understanding of the relation between the number of π^\pm and K_S^0 . This also shows that if a new tune is tuned to the track data, it will most likely also describe the number of K_S^0 produced. The PHOJET and Perugia 0 tunes are slightly below the measured ratio, and the discrepancy is about 10%.

The event generators underestimate the Λ ratio by about 40 – 60%, which indicates a clear problem in the understanding of the relation between π^\pm and Λ baryons. To understand the origin of this difference, one has to look at the difference between the K_S^0 and Λ hadrons. They have both strangeness and their mass difference can probably not describe the observed difference (since there already is a mass difference between K_S^0 and π^\pm , and the event generators is able to describe this ratio rather well). The only big difference is that Λ is a baryon and K_S^0 is a meson, thus one explanation could be that the baryon production is set too low in the event generators. A way to test this would be to look for the production of other baryons and test whether the event generators reproduce the measured results or not.

The ratio between the K_S^0 (Λ) multiplicity density and the track multiplicity density as a function of $p_T^{\text{leading jet}}$ is shown in figure 11.9. The ratio is almost flat for high $p_T^{\text{leading jet}}$, but decreases as $p_T^{\text{leading jet}}$ becomes smaller. One of the reasons for the drop off is the bias introduced by the event selection. With a requirement of at least six tracks, the track multiplicity will of course be higher. This effect influences the result most for low $p_T^{\text{leading jet}}$, since for high $p_T^{\text{leading jet}}$ the event is much more likely to produce the six tracks. The ratio in the flat plateau for K_S^0 (Λ) is ~ 0.053 (~ 0.011) in the transverse region and in the toward and away region the ratio was found to be a little below half the value of the transverse region. This is in agreement with the previous results with the ratio found in the angular density distributions.

The event generators describe the ratio much better than the individual results for K_S^0 . Especially the MC09 tune is spot on the curve, whereas the PHOJET and Perugia are about 10% below. The predicted Λ ratios are in general 60% of the measured ratio, with the Perugia tune being slightly below the other two event generators.

The ratio between the average transverse momentum of K_S^0 (Λ) and the average transverse momentum for primary tracks is shown in figure 11.10. In the toward region, first a small increase is seen (until $p_T^{\text{leading jet}} \sim 3 - 4$ GeV) followed by a long decline. The small increase in the beginning

11.5 Comparison to track based results

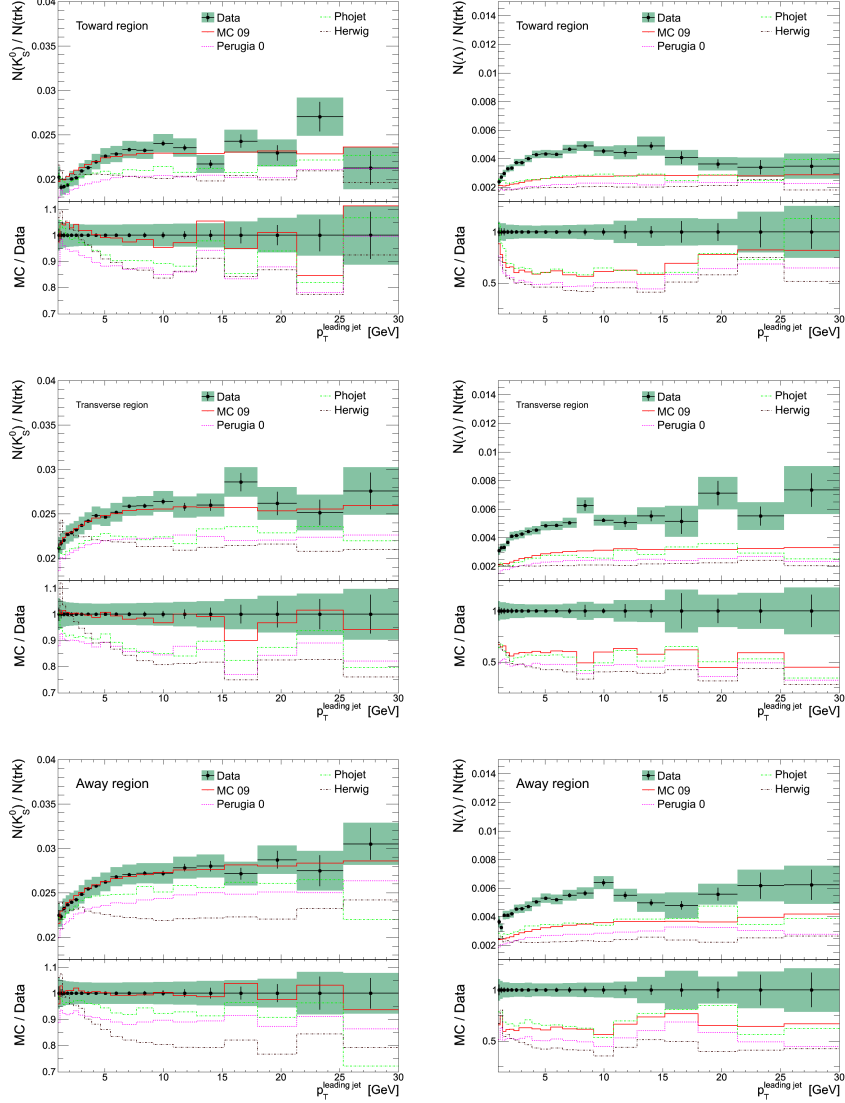


Figure 11.9: The ratio between $N_{K_S^0}$ and N_{trk} (left) and N_{Λ} and N_{trk} (right) vs. $p_T^{\text{leading jet}}$ in the toward (top), transverse (middle) and away (bottom) region, respectively. The data are corrected back to particle level and are compared to several event generators. The vertical error bar indicates the statistical uncertainty and the shaded area shows the systematic and statistical uncertainty added in quadrature. The systematic uncertainty was calculated only for the $N_{K_S^0}$ (N_{Λ}), since the systematic uncertainty on the number of tracks was assumed to be smaller.

is most likely due to the requirement of six tracks with $p_T > 500$ MeV, thus for very low $p_T^{\text{leading jet}}$ almost only the six tracks are present. The decline is explained by the tracks forming the jet also being used to calculate the average p_T . The event generators also reproduce the same behavior, even though they quantitative are about 10 % below.

In the transverse and away region, the ratios for Λ particles are almost flat and the event generators describe the observed ratios within 5 %. For K_S^0 the ratios are larger for small $p_T^{\text{leading jet}}$ in the measured distributions in both the transverse and away regions. This effect is not reproduced in the event generators and so far no explanation has been found.

The ratios between the scalar sum of the transverse momentum for K_S^0 (Λ) and tracks as a function of the leading jet p_T are shown in figure 11.11. The form of the ratios can be understood by comparing to the previous shown ratios: The decrease for low $p_T^{\text{leading jet}}$ is also observed in the multiplicity density ratios and the decline seen in the toward is from the average p_T ratios. In general, the MC09 tune predicts about 10 % below the measured value and Perugia 0 and PHOJET predict about 20 % for K_S^0 . The predicted Λ ratio is about 60 % of the measured ratio for MC09 and PHOJET and 50 % for Perugia 0. This is in agreement with the higher number of Λ particles measured in the data.

11.5 Comparison to track based results

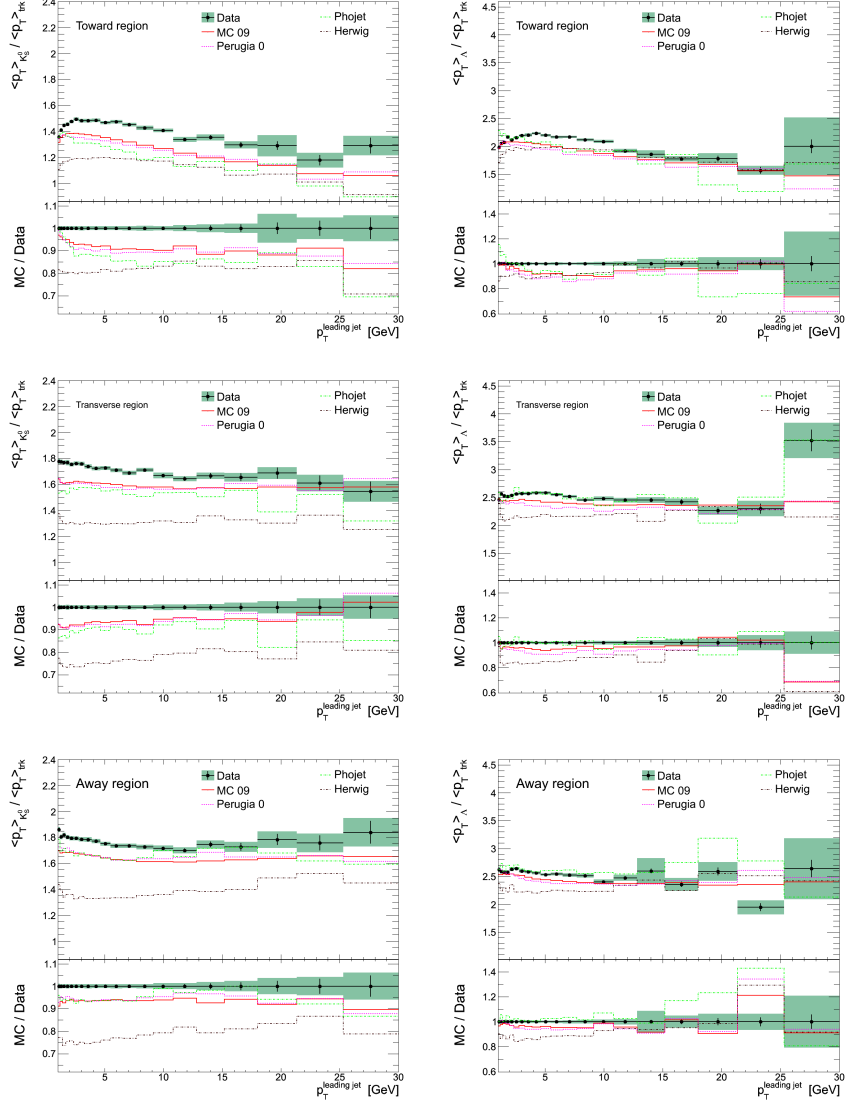


Figure 11.10: The ratio between the average momentum of, respectively, K_S^0 (left) and Λ (right), and the average momentum of primary tracks in the toward (top), transverse (middle) and away (bottom) region. The data are corrected back to particle level and are compared to several event generators. The vertical error bar indicates the statistical uncertainty and the shaded area shows the systematic and statistical uncertainty added in quadrature. The systematic uncertainty was calculated only for the $N_{K_S^0}$ (N_Λ), since the systematic uncertainty on the number of tracks was assumed to be smaller.

11.5 Comparison to track based results

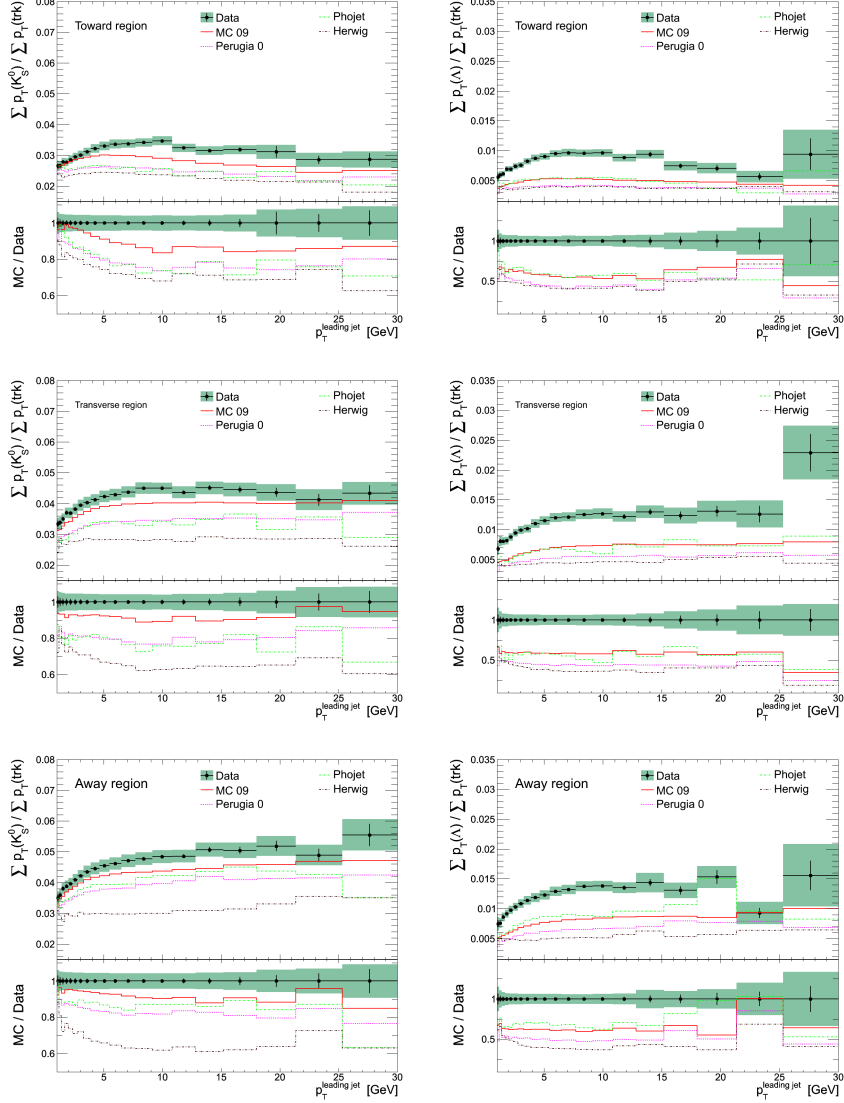


Figure 11.11: The ratio between sum p_T of, respectively, K_S^0 (left) and Λ (right), and the sum p_T of primary tracks in the toward (top), transverse (middle) and away (bottom) region, respectively. The data is corrected back to particle level and is compared to several event generators. The vertical error bar indicates the statistical uncertainty and the shaded area shows the systematic and statistical uncertainty added in quadrature. The systematic uncertainty was calculated only for the $N_{K_S^0}$ (N_Λ), since the systematic uncertainty on the number of tracks was assumed to be smaller.

12 Conclusion

In this study I have presented measurements of the underlying event using K_S^0 and Λ particles. The data was delivered by the LHC in 2010 with a center of mass energy of 7 TeV and was recorded with the ATLAS detector. The data was corrected for detector effects with the model-dependency kept at a minimum. The data was compared to several event generators and discrepancies were observed.

The event generators predict about 20 – 30 % too few K_S^0 mesons and 50 % too few Λ baryons in the transverse region, where the discrepancies were found to be largest. The difference was smallest in the toward region for soft events (i.e. low leading jet p_T), where the predictions become almost equal to the measured values. This is probably due to two effects canceling each other: Too many particles predicted in the jet production and too few in the underlying event. This was illustrated by imposing an additional cut on $\Delta\eta$ to enhance the jet effect, which made prediction from the event generators become above the measured values in the toward region for K_S^0 . The event generators do a better job at describing the average momentum distributions, where they almost stay within a 10 % difference for both K_S^0 and Λ .

To test whether the observed discrepancies were specific for K_S^0 and Λ or a more generic feature, the distributions were compared to similar distributions with tracks. The ratio between K_S^0 and tracks were found to be in good agreement with the prediction from the event generators. This indicates that if a new tune is produced describing the track production, it will probably also do a good job at describing the production of K_S^0 mesons. For Λ particles, the ratio was found to be significantly below the expected. This indicates that the ratio between baryon and meson production probably needs to be tuned to produce more baryons.

The next step would be to use the measured distributions to produce a new tune, which would provide a better description of the observed physics. Especially the huge difference between K_S^0 and Λ would provide a challenge, since a new tune also has to reproduce the results from previous collider experiments (e.g. LEP and Tevatron).

13 Appendix A - Summary of cuts

	Data	MC
	Event	
Trigger	MBTS fired	no cuts
Vertex	2 vertex tracks Veto against pile-up: If $N_{\text{vtx}} \geq 2$ with $N_{\text{trk}} \geq 4 \rightarrow$ reject event	2 vertex tracks
ND selection	$N_{\text{primary tracks}}(p_T > 500 \text{ MeV}) \geq 6$	$N_{\text{primary tracks}}(p_T > 500 \text{ MeV}) \geq 6$
	Single primary track with $p_T \geq 1 \text{ GeV}$	Single primary track with $p_T \geq 1 \text{ GeV}$
	Tracks	
Primary tracks	$p_T > 100 \text{ MeV}$, $ \eta < 2.5$ $ d_0 < 1.5 \text{ mm}$, $ z_0 \sin(\theta) < 1.5 \text{ mm}$ $N_{\text{b-layer}} = 1$, $N_{\text{pix}} \geq 1$, $N_{\text{SCT}} \geq 2, 4, 6(**)$ χ^2 probability < 0.01 if $p_T > 10 \text{ GeV}$ Veto if used in V_0	$p_T > 100 \text{ MeV}$, $ \eta < 2.5$, $\text{charge} \neq 0$, $\text{barcode} \neq 0$ $\text{barcode} < 100000$ (*).
BS track	$p_T > 100 \text{ MeV}$, $ \eta < 2.5$ $ d_0 < 1.8 \text{ mm}$, $N_{\text{b-layer}} = 1$, $N_{\text{pix}} \geq 1$, $N_{\text{SCT}} \geq 2, 4, 6(**)$ χ^2 probability < 0.01 if $p_T > 10 \text{ GeV}$	(same as for primary track)
Vertex track	$p_T > 100 \text{ MeV}$, $ \eta < 2.5$, $N_{\text{pix}} \geq 1$, $N_{\text{SCT}} \geq 4$, $N_{\text{silicon}} \geq 6$, $ d_0^{BS} < 4 \text{ mm}$, $\delta(d_0^{BS}) < 5 \text{ mm}$ and $\delta(z_0^{BS}) < 10 \text{ mm}$	(same as for primary track)
Decay track	$p_T > 100 \text{ MeV}$, $ \eta < 2.5$, $N_{\text{SCT}} \geq 2$,	$p_T > 100 \text{ MeV}$, $ \eta < 2.5$, $\text{charge} \neq 0$
	Secondary vertices	
K^0	2 decay tracks $p_T > 100 \text{ MeV}$, $d_{xy} > 4 \text{ mm}$, $\text{CosThetaPointing} < 0.999$, $\chi^2 < 15$, $ M_{p^+\pi^-} - M_\Lambda > 5.8 \text{ MeV}$, $ M_{p^-\pi^+} - M_{\bar{\Lambda}} > 5.8 \text{ MeV}$	2 decay tracks $p_T > 100 \text{ MeV}$, $ \eta < 2.5$ $d_{xy} > 4 \text{ mm}$, $\text{barcode} \neq 0$ $\text{barcode} < 100000$ (*)
Λ	2 decay tracks $p_T > 500 \text{ MeV}$, $d_{xy} > 17 \text{ mm}$, $\text{CosThetaPointing} < 0.9998$, $\chi^2 < 15$, $ M_{\pi^+\pi^-} - M_{K^0} > 14.4 \text{ MeV}$	2 decay tracks $p_T > 500 \text{ MeV}$, $ \eta < 2.5$ $d_{xy} > 17 \text{ mm}$, $\text{barcode} \neq 0$ $\text{barcode} < 100000$ (*)

Table 13.1: The different cuts imposed in the selection of event, track and secondary vertices. The left column shows the selection criteria on the data samples and the right column shows the selection for the MC truth level (event generators). (*) The barcode cut is used to select primary particles. (**) 2, 4 or 6 for respectively $p_T < 200 \text{ MeV}$, $200 \text{ MeV} < p_T < 300 \text{ MeV}$ and $300 \text{ MeV} < p_T$.

14 Appendix B - Glossary

ALFA ALFA (Absolute Luminosity For ATLAS) is a forward detector in the ATLAS experiment designed to measure the total luminosity by studying elastic scattering.

ALICE ALICE (A Large Ion Collider Experiment) is one of the four major detectors at the LHC. It is designed to study the heavy ion collisions in details.

ATLAS ATLAS (A Toroidal LHC ApparatuS) is one of the four major detectors at the LHC. It is a general purpose detector, designed to look for any new indications of physics beyond the standard model.

Azimuthal angle The azimuthal angle, ϕ , is the angle perpendicular to the beam axis.

BS Beamspot is the area within the detector where the collisions take place.

BPTX BPTX (Beam Pick-up Timing device) is two detectors placed ± 175 m away from the ATLAS detector. These are used to check for coincidence between the two beams such that it is known that the beams collide within the ATLAS detector

Calorimeter Is the part of a detector, where the energy of the particles is measured.

CD CD (Central Diffractive) is the type diffractive collisions, where both protons stay intact but create an excited system that can decay.

CDF CDF is one of the two detectors at Tevatron studying $p\bar{p}$ collisions.

CERN CERN (Conseil Européen pour la Recherche Nucléaire) is the European center for nuclear research; where the LHC is located.

CMS CMS (Compact Muon Solenoid) is one of the four major experiments at LHC. It is a general purpose detector, designed to look for a huge variety of physics beyond the standard model.

CP CP is the combination of the charge and parity operators. And the cp number tells how a state will change under both a charge and parity inversion.

CT10 CT10 is one of the groups producing a global fit for the PDFs.

-
- Diffractive events** Diffractive events are a classification of soft QCD collisions. If the collision do only result in two protons in excited states and they afterwards decay, the collision is called diffractive. In the detector, they are characterized by jets in the forward direction.
- DD** DD (Double Diffractive) is a type of diffractive events where both protons are excited and afterwards decay.
- DESY** DESY is a german research center for particle physics. It has housed the HERA accelerator.
- D0** D0 is one of the two detectors at Tevatron studying $p\bar{p}$ collisions.
- Elastic event** Elastic events are collisions where only a momentum transfer takes place between the two protons ($pp \rightarrow pp$).
- η** See Pseudorapidity
- Fermilab** Fermilab is an american research center. It houses the Tevatron accelerator.
- FSR** FSR (Final State Radiation) is the radiation of gluons or quarks after the collision took place.
- GEANT** GEANT is a detector simulation program, used to provide a simulation of the expected detector response when particles are travelling through it.
- Hadronization** Hadronization is the process of going from colored partons to colorless hadrons.
- Hard Interaction** The hard interaction is the interaction with the highest momentum transfer in a pp-collision.
- HERA** HERA (Hadron-Elektron-Ring-Anlage) was an electron-proton collider located at DESY. It was especially useful in determining the PDFs.
- HERWIG** HERWIG (Hadron Emission Reactions With Interfering Gluons) is a general event generator, which can simulate full events from hard interaction to hadronization.
- Inelastic events** The opposite of elastic events, thus at least one of the two protons has to break apart.

-
- ISR** ISR (Initial State Radiation) is the radiation of gluons or quarks before the actual collision take place.
- Jet** A jet is a combination of particles moving in almost the same direction in the detector.
- K^0 meson** K^0 is a meson consisting of a d-quark and an anti s-quark. In the detector, the observed particle is not the K^0 itself, but a linear combination of K^0 and \bar{K}^0 called K_S^0 .
- Kalman filter** The Kalman filter is an estimator used to do the full track reconstruction.
- Λ baryon** The Λ particle is a baryon consisting of a u-,d- and s-quark (uds).
- LEP** LEP (Large Electron-Positron collider) was an e^+e^- particle accelerator located at CERN.
- LHC** LHC (Large Hadron Collider) is an accelerator ring used to accelerate two protons to almost the speed of light, before colliding them in the experiments. LHC is located at CERN.
- LHC-b** LHC-b is one of the four major experiments at the LHC. It is focused on studying b-physics.
- LO** LO (Leading Order) refers to the perturbation calculation in calculating the hard processes within the standard model.
- MC** MC (Monte Carlo) is a simulation technique used to generate events from theory.
- MB** Minimum bias is the selection of all events where two protons collide, selected with as little bias as possible.
- MBTS** MBTS (Minimum Bias Trigger Scintillators) are two forward detectors in the ATLAS experiment, used to determine whether a collision took place or not.
- MPI** MPI (Multiple Parton Interactions) is the phenomenon of several parton interactions within the same proton-proton collision.
- MSTW** MSTW (Martin-Stirling-Thorne-Watt) is one of the groups producing a global fit for the PDFs.
- ND events** The opposite of diffractive events, requiring a collision between the partons of the two protons.

NLO NLO (Next-to-Leading-Order) refers to the perturbation calculation in calculating the hard processes within the standard model.

NSD All types of inelastic scattering except for single diffractive.

PDG PDG (Particle Data Group) provides a summary of particle physics every second year.

PHOJET PHOJET is a minimum bias event generator.

Pixel Pixel detector is a detector, where the sensitive area is split into small pixels. It also refers to the inner most section of the ATLAS inner detector, which is a pixel detector.

Pseudorapidity Pseudorapidity is defined as $\eta = -\ln \tan\left(\frac{\theta}{2}\right)$, thus it is just another measure of the angle between the particle and the beam. In the limit of massless particles, the rapidity and pseudorapidity becomes equal, which is the reason for its use in particle physics. It is very often used in experiments, due to it being impossible to calculate the rapidity without particle identification.

p_T See transverse momentum

Primary vertex The primary vertex is the collision point between the two protons.

PYTHIA PYTHIA is a general event generator, which can simulate full events from hard interaction to hadronization.

PS The PS (Proton Synchrotron) was the first major particle accelerator at CERN.

QCD QCD (Quantum Chromo Dynamics) is the theory describing the strong force.

QED QED (Quantum ElectroDynamics) is the theory describing the electromagnetic force.

QFT QFT (Quantum Field Theory) is the mathematical foundation for the standard model.

ΔR -matching ΔR -matching is a method to match the generated particles with reconstructed particle in the simulation. The two particles are required to have $\Delta R = \sqrt{\Delta\phi^2 + \Delta\eta^2} < 0.15$ to be matched.

Rapidity Rapidity is defined as $y = \frac{1}{2} \ln \frac{E+p_z}{E-p_z}$, where z is the beam direction. This is a theoretical convenient quantity, due to its additive behavior under Lorentz boost along the beam axis, resulting in Δy being a conserved quantity.

Renormalization Renormalization is a technique used in QFT to make otherwise infinity integrals finite.

SCT SCT is a silicon strip detector located in the ATLAS inner detector.

SD Single diffractive events are subclass of diffractive events, where only one of the two protons breaks up.

Secondary vertex Secondary vertices are vertices, which do not come from the primary proton-proton collision.

SHERPA SHERPA is a general event generator, which can simulate full events from hard interaction to hadronization.

SLAC SLAC (Stanford Linear Accelerator Complex) is a linear accelerator located in the United States of America.

SM The SM (Standard Model) is the theory used within particle physics and has had a great success describing all collider experiments.

SPS SPS (Super Proton Synchrotron) was a $p\bar{p}$ collider located at CERN, it is now used as injection to the LHC.

Tevatron A $p\bar{p}$ collider located at Fermilab in the United States.

θ θ is the angle between a particle and the beam. θ is equal to zero along the beam axis.

Track A track is a combinations of hits in the detector, which describe the path of a particle traversing the detector.

Transverse momentum p_T - The momentum of a particle perpendicular to the beam axis.

TRT Transition Radiation Tracker is the outer most part of the inner detector of the ATLAS experiment.

UE The underlying event refers to the particle coming from the beam remnants and MPI in a pp-collision.

Vertex If several tracks points towards a common point in the detector, it is plausible that they all origin from this point. Such a point is known as a vertex.

χ^2 χ^2 is quantity describing how well a fit matches the data.

y See rapidity

References

- [1] V. Khachatryan et al. Strange particle production in pp collisions at $\sqrt{s} = 0.9$ and 7 TeV. *Journal of High Energy Physics*, 2011:1–40, 2011. 10.1007/JHEP05(2011)064.
- [2] Search for the Higgs boson in the diphoton final state with 38 pb⁻¹ of data recorded by the ATLAS detector in proton-proton collisions at $\sqrt{s} = 7$ TeV. Technical Report ATLAS-CONF-2011-025, CERN, Geneva, Mar 2011.
- [3] K. Aamodt et al. Midrapidity Antiproton-to-Proton Ratio in pp Collisions at $\sqrt{s} = 0.9$ and 7 TeV Measured by the ALICE Experiment. *Phys. Rev. Lett.*, 105(7):072002, Aug 2010.
- [4] K. Kodama et al. Observation of tau neutrino interactions. *Physics Letters B*, 504(3):218 – 224, 2001.
- [5] Tony Rothman and Stephen Boughn. Can gravitons be detected? *Found. Phys.*, 36:1801–1825, 2006.
- [6] Michael E. Peskin and Daniel V. Schroeder. *An Introduction to Quantum Field Theory*. Westview Press, 1995.
- [7] B.J. Björken and S.L. Glashow. Elementary particles and SU(4). *Physics Letters*, 11(3):255 – 257, 1964.
- [8] J. Augustin et al. Discovery of a Narrow Resonance in e^+e^- Annihilation. *Phys. Rev. Lett.*, 33(23):1406–1408, Dec 1974.
- [9] J. J. Aubert et al. Experimental Observation of a Heavy Particle j . *Phys. Rev. Lett.*, 33(23):1404–1406, Dec 1974.
- [10] K Nakamura and Particle Data Group. Review of Particle Physics. *Journal of Physics G: Nuclear and Particle Physics*, 37(7A):075021, 2010.
- [11] B.R. Martin and G. Shaw. *Particle Physics*. Wiley, second edition, 1997.
- [12] A. D. Martin, W. J. Stirling, R. S. Thorne, and G. Watt. Parton distributions for the LHC. *Eur. Phys. J.*, C63:189–285, 2009.
- [13] Hung-Liang Lai et al. New parton distributions for collider physics. *Phys. Rev.*, D82:074024, 2010.

-
- [14] Andy Buckley et al. General-purpose event generators for LHC physics. 2011.
- [15] G. Corcella et al. HERWIG 6.5 release note. 2002.
- [16] G. Gustafson B. Andersson and B. Söderberg. A general model for jet fragmentation. *Zeitschrift für physic C Particles and Fields*, 20(4):317–329, 1983.
- [17] Torbjörn Sjöstrand, Stephen Mrenna, and Peter Skands. PYTHIA 6.4 physics and manual. *Journal of High Energy Physics*, 2006(05):026, 2006.
- [18] R. Engel. Photoproduction within the two-component Dual Parton Model: Amplitudes and cross sections. *Zeitschrift für Physik C Particles and Fields*, 66:203–214, 1995. 10.1007/BF01496594.
- [19] T. Gleisberg et al. Event generation with SHERPA 1.1. *JHEP*, 02:007, 2009.
- [20] ATLAS Monte Carlo tunes for MC09. Technical Report ATL-PHYS-PUB-2010-002, CERN, Geneva, Mar 2010.
- [21] Peter Zeiler Skands. Tuning Monte Carlo Generators: The Perugia Tunes. *Phys. Rev.*, D82:074018, 2010.
- [22] A. Capella, U. Sukhatme, C. I. Tan, and J. Tran Thanh Van. Dual parton model. *Physics Reports*, 236(4-5):225 – 329, 1994.
- [23] Stefan Gieseke, Philip Stephens, and Bryan Webber. New formalism for QCD parton showers. *Journal of High Energy Physics*, 2003(12):045, 2003.
- [24] ATLAS tunes of PYTHIA 6 and Pythia 8 for MC11. Technical Report ATL-PHYS-PUB-2011-009, CERN, Geneva, Jul 2011.
- [25] G. Aad et al. Measurement of underlying event characteristics using charged particles in pp collisions at $\sqrt{s} = 900$ GeV and 7 TeV with the ATLAS detector. *Phys. Rev. D*, 83(11):112001, May 2011.
- [26] CMS Collaboration. First measurement of the underlying event activity at the LHC with $\sqrt{s} = 0.9$ TeV. *The European Physical Journal C - Particles and Fields*, 70:555–572, 2010. 10.1140/epjc/s10052-010-1453-9.

-
- [27] CMS Collaboration. Measurement of the Underlying Event Activity at the LHC with $\sqrt{s} = 7$ TeV and Comparison with $\sqrt{s} = 0.9$ TeV. 2011.
- [28] G. Aad et al. Measurements of underlying-event properties using neutral and charged particles in pp collisions at $\sqrt{s} = 900$ GeV and $\sqrt{s} = 7$ TeV with the ATLAS detector at the LHC. *The European Physical Journal C - Particles and Fields*, 71:1–24, 2011. 10.1140/epjc/s10052-011-1636-z.
- [29] New ATLAS event generator tunes to 2010 data. Technical Report ATL-PHYS-PUB-2011-008, CERN, Geneva, Apr 2011.
- [30] Joao Pequeno. Computer generated image of the whole ATLAS detector. Mar 2008.
- [31] G. Aad et al. The ATLAS Experiment at the CERN Large Hadron Collider. *J. Instrum.*, 3:S08003. 437 p, 2008. Also published by CERN Geneva in 2010.
- [32] H. Bethe. Zur Theorie des Durchgangs schneller Korpuskularstrahlen durch Materie. *Annalen der Physik*, 397(3):325–400, 1930.
- [33] K. Kleinknecht. *detectors for particle radiation*. Cambridge University Press, 2nd edition, 1998.
- [34] R. Frühwirth. Application of Kalman filtering to track and vertex fitting. *Nuclear Instruments and Methods in Physics Research Section A: Accelerators, Spectrometers, Detectors and Associated Equipment*, 262(2-3):444 – 450, 1987.
- [35] T Cornelissen, M Elsing, I Gavrilenko, W Liebig, E Moyses, and A Salzburger. The new ATLAS track reconstruction (NEWT). *Journal of Physics: Conference Series*, 119(3):032014, 2008.
- [36] E Bouhova-Thacker, P Lichard, V Kostyukhin, W Liebig, M Limper, G Piacquadio, P Lichard, C Weiser, and A Wildauer. Vertex Reconstruction in the ATLAS Experiment at the LHC. Technical Report ATL-INDET-PUB-2009-001. ATL-COM-INDET-2009-011, CERN, Geneva, May 2009. Note was a proceeding for IEEE/NSS Dresden 2008 and is now intended for possible publication in TNS.
- [37] P. Billoir and S. Qian. Fast vertex fitting with a local parametrization of tracks. *Nuclear Instruments and Methods in Physics Research Section A: Accelerators, Spectrometers, Detectors and Associated Equipment*, 311(1-2):139 – 150, 1992.

-
- [38] S. Agostinelli et al. G4—a simulation toolkit. *Nuclear Instruments and Methods in Physics Research Section A: Accelerators, Spectrometers, Detectors and Associated Equipment*, 506(3):250 – 303, 2003.
- [39] J. Allison et al. Geant4 developments and applications. *Nuclear Science, IEEE Transactions on*, 53:270 – 278, 2006.
- [40] G. Aad et al. The ATLAS Simulation Infrastructure. *The European Physical Journal C - Particles and Fields*, 70:823–874, 2010. 10.1140/epjc/s10052-010-1429-9.
- [41] Mapping the material in the ATLAS Inner Detector using secondary hadronic interactions in 7 TeV collisions. Technical Report ATLAS-CONF-2010-058, CERN, Geneva, Jul 2010.
- [42] Alignment of the ATLAS Inner Detector Tracking System with 2010 LHC proton-proton collisions at $\sqrt{s} = 7$ TeV. Technical Report ATLAS-CONF-2011-012, CERN, Geneva, Mar 2011.
- [43] Georges Aad et al. Charged-particle multiplicities in pp interactions measured with the ATLAS detector at the LHC. *New J.Phys.*, 13:053033, 2011. Long author list - awaiting processing.
- [44] Matteo Cacciari, Gavin P. Salam, and Gregory Soyez. The anti- k_t jet clustering algorithm. *Journal of High Energy Physics*, 2008(04):063, 2008.
- [45] G. Aad et al. Charged-particle multiplicities in pp interactions at $\sqrt{s} = 900$ GeV measured with the ATLAS detector at the LHC. *Phys.Lett.*, B688:21–42, 2010.
- [46] Georges Aad et al. Properties of jets measured from tracks in proton-proton collisions at center-of-mass energy $\sqrt{s} = 7$ TeV with the ATLAS detector. 2011.

15 Resume - English

The aim with this thesis was to study the production of strange particles (as K_S^0 and Λ) in the underlying event in pp collisions in the LHC accelerator at CERN. The underlying event is present in all the collisions, and as such it is important to understand when looking for new physics beyond the standard model.

The data used was measured with the ATLAS detector at LHC at a center-of-mass energy of $\sqrt{s} = 7$ TeV. From the huge amount of data, primarily events from non-diffractive collisions were selected, which was achieved by imposing different cuts on the data.

The K_S^0 mesons and Λ baryons were identified by their decays into, respectively, $\pi^+\pi^-$ and $p\pi^-$. However, it is not possible to tell whether a specific particle comes from the underlying event or another part of the pp collision. Instead one has to look at the average distributions and try to find regions, which are more sensitive to the underlying event. This can be obtained by looking in the so-called region transverse to the leading jet ($\frac{\pi}{3} < |\Delta\phi| < \frac{2\pi}{3}$), since the number of particles from other parts of the pp collision is less in this region. Furthermore, a simulation of the detector was used to correct for the efficiencies, such that it was possible to compare the results with the expected results from theory.

Due to the complexity of the theory, one has to rely on simulation to estimate the expected results from the theory, these simulations are known as event generators. Several different event generators exist and also different tunes within each event generator (a tune refers to a different set of parameters).

Comparing the results from the observed K_S^0 and Λ particles with the results from running different event generators based on the theory, discrepancies were observed. The event generators predicted about 20 – 30% too few K_S^0 mesons and 50% too few Λ baryons in the transverse region, where the discrepancies were found to be largest. The event generators did a better job at describing the average momentum distributions, where they almost stayed within a 10% difference for both K_S^0 and Λ .

To test whether the observed discrepancies were specific for K_S^0 and Λ or a more generic feature, the distributions were compared to similar distributions with the primary charged particles (observed as tracks in the

detector). The ratio between K_S^0 and tracks were found to be in good agreement with the prediction from the event generators. This indicated that if a new tune is produced describing the track production, it will probably also do a good job at describing the production of K_S^0 mesons. For Λ particles, the ratio was found to be significantly below the expected. This indicated that the ratio between baryon and meson production probably needs to be tuned to produce more baryons.

16 Resume - dansk

Formålet med dette speciale var at studere produktionen af sære partikler (som K_S^0 og Λ) i den underliggende begivenhed i pp kollisioner ved LHC acceleratoren på CERN. Den underliggende begivenhed er tilstede i alle kollisioner og derfor er forståelsen af den vigtig for at kunne opdage noget nyt udenfor standardmodellen.

Dataene brugt i dette speciale blev optaget med ATLAS detektoren ved LHC ved en kollisionsenergi på $\sqrt{s} = 7$ TeV. Ved at indføre et sæt begrænsende kriterier (cuts), udvalgte de begivenheder som ikke stammede fra ikke-diffraktive kollisioner.

K_S^0 og Λ partiklerne blev identificeret ved deres henfald til henholdsvis $\pi^+\pi^-$ og $p\pi^-$. Det er dog ikke muligt umiddelbart at kunne fortælle om en partikel kommer fra den underliggende begivenhed eller en anden del af pp kollisionen. Så for bedre at kunne studere den underliggende begivenhed, blev observationen af hadronerne splittet op i tre områder: imod området, det tværgående område og væk området. Det mest sensitive område, for at studere den underliggende begivenhed, er det tværgående område, da der er mindre baggrund i dette område. Endvidere blev de målte resultater korrigeret for detektor effekter, for at kunne sammenligne dem med teorien.

På grund af kompleksiteten af standardmodellen, bliver man nødt til at simulere de forventede måleresultater. Der findes forskellige simuleringer, som alle prøver at simulere kollisioner mellem protoner. I dette speciale blev de målte data sammenlignet med fire forskellige simuleringer.

Der blev observeret afvigelser mellem den forventede teori og de målte fordelinger. Teorien forudsagde omkring 20 – 30 % for få K_S^0 mesoner og 50 % Λ baryoner i det tværgående område, hvor afvigelsen var størst. Forudsigelserne fra teorien var bedre til at beskrive den gennemsnitlige bevægelsesmængde fordeling, hvor afvigelsen var i størrelsesordenen 10 % for både K_S^0 og Λ partikler.

For at teste om afvigelsen kun var for K_S^0 og Λ partikler eller det skyldtes en mere generel tendens, blev resultaterne sammenlignet med lignende resultater fundet med brug af spor fra ladede partikler. Forholdet med antallet af K_S^0 mesoner og spor stemte godt overens med det forventede fra teorien. Dette indikerede, at hvis man kan beskrive fordelingen af ladede

spor, så følger fordelinger af K_S^0 mesoner automatisk med. For Λ baryoner blev forholdet derimod fundet til at være betydeligt under det forventede. Dette tydede på at teorien ikke er særlig god til at beskrive forholdet mellem produktionen af baryoner og mesoner.